Dissertation

Investigation of the interaction between gravity waves and the tropopause

Christopher Pütz

Berlin 2018

Fachbereich Mathematik und Informatik
Institut für Mathematik
Freie Universität Berlin

zur Erlangung des Grades eines
Doktors der Naturwissenschaften

Erstgutachter und Betreuer der Promotion:
Prof. Dr.-Ing. Rupert Klein

Zweitgutachter:
Prof. Dr. Peter Spichtinger

Tag der Disputation:
29. Juni 2018

Contents

1 Introduction

The atmosphere of the earth can be seen as a stratified fluid with height-dependent variation in density, pressure and temperature. Oftentimes, this stratification is stable, meaning that denser air masses lie below lighter ones. Such an environment permits internal gravity waves. The atmosphere is structured in several principal layers. The lower part consists of the troposphere ranging from the earth's surface up to around 12 km and the stratosphere on top of it to approximately 50 km. In the troposphere, the absolute temperature decreases with height. The stratosphere, in contrast, has a constant temperature in the lower part and even an increase in temperature in the upper part. The location where the temperature gradient switches its sign from negative to non-negative is defined as the tropopause. It is a rather shallow area of 1-2 km depth where tropospheric and stratospheric air masses mix.

The tropopause plays a key role in the propagation of gravity waves from the troposphere to the stratosphere. Birner et al. (2002) and Birner (2006) used observational and reanalysis data to describe the temperature inversion layer in extratropical regions. Gettelman et al. (2011) conducted an extensive study the extratropical tropopause region, finding that it constitutes a transport barrier for many trace gases. A recent study of Gisinger et al. (2017) includes the observation of the propagation of gravity waves through the tropopause during the DEEPWAVE-campaign in New Zealand. Once in the stratosphere, gravity waves can have a major impact on the circulation in the lower and middle atmosphere by depositing their momentum to the background flow due to wave-mean flow interaction and wave breaking (Fritts and Alexander, 2003).

An important characteristic of gravity waves is the ability to transport energy not only horizontally but vertically. Eliassen and Palm (1961) analysed waves carrying energy upward and downward in the context of orographically excited gravity waves that reflect from vertically varying stratification and wind. They used a piecewise-constant approximation for both stratification and wind and found local solutions which were matched at the discontinuities of the approximation. This approximation will found the basis for a large part of the work presented in this thesis.

A similar approach was taken by Danielsen and Bleck (1970) who examined mountain waves and approximated key atmospheric parameters by piecewise exponential functions. This method allowed them to solve the governing equations by combinations of Bessel functions. Sutherland and Yewchuck (2004) attended to the topic again and scrutinised the phenomenon of wave tunnelling, which describes the energy transport over a finite layer of decreased, or even vanishing, stratification. They undertook a mathematical analysis as well as laboratory experiments to support their findings. Brown and Sutherland (2007) expanded the theory by allowing for shear flow over an unstratified layer. Both scenarios were later examined numerically by Nault and Sutherland (2007) who provided numerical solutions for plane wave transmission in arbitrary stratification and wind. As a specific example, they performed simulations for an atmospheric stratification and wind profile that was observed over Jan Mayen island.

When speaking of atmospheric gravity waves, one has to keep in mind that they are usually spatially and temporally confined. One of the first investigations of such wave packets goes back to Benney and Newell (1967), who described wave packets as superposition of finitely many plane waves. Grimshaw (1977) discussed the modulation of a wave packet when moving through non-homogeneous media. He derived evolution equations for the wave packet envelope and found it to be moving with the group velocity in leading order. A very common approximation that is made for gravity wave packets is the WKB assumption, meaning that the envelope as well as the background is slowly varying compared to a wavelength. Achatz et al. (2010) carried out a scale analysis for the Euler equations and derived leading and first order equations describing the evolution of WKB gravity wave packets on long time scales that allows the packet to travel large vertical distances. The derivations were made for small- and large-amplitude waves. Their findings match very well with the pseudo-incompressible theory developed by Durran (1989) while they go beyound the regime of validity of other soundproof models (Boussinesq and anelastic). A complete discussion on the regime of validity for those atmospheric models can be found in Klein et al. (2010) and Klein (2011). The theory was numerically validated by Rieper et al. (2013a) and is one of the most general descriptions of atmospheric internal gravity wave packets. Very recently, Schlutow et al. (2017) were able to close the modulation equations found in Achatz et al. (2010) and derive analytic solutions describing travelling waves in the atmosphere. They are the first and to the best of the authors' knowledge only ones to ever find analytical descriptions of atmospheric gravity waves beyond plane wave solutions.

A difficulty with the handling of gravity waves in numerical weather models is their large wavelength spectrum. It ranges from a few hundred metres up to several thousands of kilometres in the horizontal direction. The Integrated Forecast System (IFS) of the European Centre for Medium-range Weather Forecast (ECMWF) uses a triangular mesh with 9 km grid size, the ICON model of the German weather service (DWD) is currently operational with a grid size of 13 km, with an extension down to 6.5 km soon to go live. Even high resolution regional models, such as COSMO-DE, which runs with a resolution of 2.8 km are not able to capture the whole gravity wave spectrum. Non-resolved waves therefore have to be parametrised.

Parametrisations are build on a basic understanding of gravity waves being excited somewhere in the troposphere, travelling upward, growing in amplitude due to the lower density and eventually break, dissipating their momentum and energy irreversibly to the mean flow. One of the tasks of gravity wave parametrisations is to predict when and where the breaking process happens, but also to predict wave reflection from phenomena such as a jet stream or a temperature inversion layer.

The aim of this work is to provide a description of gravity waves interacting with the tropopause. In chapter 2, we will derive the linearised Boussinesq equations from the Euler equations and give justification for the assumptions we make over the course of the simplification. After reducing the system down to a single equation, we will develop a method to solve this equation approximately in chapter 3 in case of a steady atmosphere. This so-called multi-layer method builds the foundation for the upcoming chapters. It has the advantage of separating upward and downward propagating waves in the solution, such that we can compute transmission coefficients, that describe the ratio of transmitted and incident wave energy, from it. Chapter 4 is concerned with the inclusion of a non-steady background wind into the multi-layer method. It also includes an extensive discussion on a term containing the curvature of the background wind, as this is often neglected in the common literature. We will switch the focus to the investigation of wave packets in chapter 5. With the help of Fourier transform and a coordinate transformation using the gravity wave dispersion relation, it is possible to reformulate the governing equation in a way that a modified multi-layer method can be applied. We use an inverse Fourier transform on the solution to obtain the full spatial and temporal evolution of a gravity wave packet without any restrictions regarding scaling or time steps. A numerical validation of the multi-layer method can be found in chapter 6. There, we compare solutions given by the multi-layer method with solutions found from simulations of the full Boussinesq equations. In chapter 7, we will investigate the wave-tropopause interaction from a different angle, using the tools of multiple-scale analysis. By dividing the waves in three regimes, dependent on the aspect ratio of vertical wavelength and tropopause depth, we derive dimensionless equations describing the gravity wave propagation through the tropopause for the respective aspect ratios. For two of the three regimes, it is possible to derive a leading order solution, while the remaining regime is hard to analyse from the perspective of multiple-scale analysis. The thesis will be concluded in chapter 8 with a summary of the results as well as discussion of open challenges.

2 The Boussinesq equations

This chapter will give a framework for the upcoming investigations. We start with the dimensional Euler equations, which describe various types of inviscid atmospheric flows. Since our interest lies in the interaction of gravity waves with the tropopause, we may use some assumptions to find a set of equations which are easier to handle than the full Euler equations.

2.1 Euler equations

We consider gravity waves in a two-dimensional reference frame, with one horizontal (alongside the earth's surface) and one vertical (perpendicular to the earth's surface) axis. The horizontal coordinate will be named x, but in contrast to the usual convention in three-dimensional atmospheric investigations, it does not need to point in zonal direction. The two-dimensional setup allows us to neglect the Coriolis force, making the equations more manageable while still giving a fundamental understanding of gravity wave dynamics. Moreover, we do not consider external heat sources or viscous effects. The Euler equations can then be written as (see Achatz et al. (2010))

$$\frac{\mathrm{D}u}{\mathrm{D}t} + c_p\theta\frac{\partial \mathit{\Pi}}{\partial x} = 0, \tag{2.1a}$$

$$\frac{\mathrm{D}w}{\mathrm{D}t} + c_p\theta\frac{\partial \mathit{\Pi}}{\partial z} = -g, \tag{2.1b}$$

$$\frac{\mathrm{D}\theta}{\mathrm{D}t} = 0, \tag{2.1c}$$

$$\frac{\mathrm{D}\mathit{\Pi}}{\mathrm{D}t} + \frac{\kappa}{1-\kappa}\mathit{\Pi}\left(\frac{\partial u}{\partial x} + \frac{\partial w}{\partial z}\right) = 0. \tag{2.1d}$$

Here, u denotes the horizontal wind component, w denotes the vertical wind component, g is the gravitational acceleration and

$$\frac{\mathrm{D}}{\mathrm{D}t} = \frac{\partial}{\partial t} + u\frac{\partial}{\partial x} + w\frac{\partial}{\partial z} \tag{2.2}$$

is the material derivative. Further, c_p is the specific heat capacity of dry air at constant pressure, R denotes the specific gas constant of dry air and their ratio is denoted as $\kappa = R/c_p$. $\Pi = (p/p_0)^\kappa$ indicates the Exner pressure function, which is a non-dimensional form of the pressure p normalised with a reference value p_0. The potential temperature $\theta = T/\Pi$ can be seen a rescaling of the absolute temperature T via the Exner pressure. Both are linked via the equation of state for an ideal gas

$$\Pi^{\frac{1-\kappa}{\kappa}} = \frac{R\rho\theta}{p_0}, \tag{2.3}$$

where ρ denotes the density. Equations (2.1a) and (2.1b) describe the momentum transport. Equation (2.1c) is the first law of thermodynamics for adiabatic processes, sometimes called conservation of internal energy or entropy equation. Equation (2.1d) reflects the conservation of mass, also referred to as continuity equation.

2.2 Simplifying the Euler equations

The purpose of this work is to investigate the interaction of gravity waves and the tropopause. In order to accomplish this, we make several physically meaningful assumptions that will allow us to simplify the Euler equations.

1. Since the vertical extent of the tropopause is small compared to atmospheric reference heights such as density or potential temperature scale height, we use the Boussinesq approximation. This means we assume that the total density only varies by a small fraction compared to a constant reference value.

2. We assume a hydrostatic atmosphere, which results in the vertical change in Exner pressure being inversely proportional to the potential temperature.

3. We are not interested in wave breaking in the first place, but assume that the wave amplitudes are small. This allows a linearisation of the governing equations.

The first assumption leads to the elimination of the material derivative of the pressure in the continuity equation (2.1d). To see this, we have a look at the equation of state under the Boussinesq approximation:

$$\Pi^{\frac{1-\kappa}{\kappa}} = \frac{R\rho_0\theta}{p_0}. \tag{2.4}$$

So basically, the variable density ρ was replaced by a constant reference value ρ_0. By rewriting equation (2.1d), we obtain

$$\frac{\mathrm{D}}{\mathrm{D}t}\left(\ln(\Pi^{\frac{1-\kappa}{\kappa}})\right) + \left(\frac{\partial u}{\partial x} + \frac{\partial w}{\partial z}\right) = 0. \tag{2.5}$$

Replacing the pressure according to equation (2.4), using the fact that all variables but θ are constant and reversing the logarithmic derivative, we find

$$\frac{R\rho_0}{p_0}\frac{1}{\theta}\frac{\mathrm{D}\theta}{\mathrm{D}t}+\left(\frac{\partial u}{\partial x}+\frac{\partial w}{\partial z}\right)=0. \tag{2.6}$$

But as we know from the entropy equation (2.1c), the material derivative of the potential temperature vanishes. As we additionally assume that the potential temperature is not zero (which is actually not an assumption but a fact for the atmosphere, see International Standard Atmosphere ISO 2533:1975), we see that the first term in the equation above vanishes, leaving us with the incompressible continuity equation

$$\frac{\partial u}{\partial x}+\frac{\partial w}{\partial z}=0. \tag{2.7}$$

For the linearisation, we make the following ansatz for the dynamic variables:

$$u(x,z,t)=\overline{u}(z)+u'(x,z,t), \tag{2.8a}$$
$$w(x,z,t)=w'(x,z,t), \tag{2.8b}$$
$$\Pi(x,z,t)=\Pi_0+\overline{\Pi}(z)+\Pi'(x,z,t). \tag{2.8c}$$

Here, Π_0 is a constant reference state, over-lined variables correspond to background values, which are only height-dependent and the primed variables are small perturbations that describe the wave movement. From the equation of state (2.3), we obtain a relation between density, potential temperature and Exner pressure. The Boussinesq approximation suggests that

$$\theta(x,z,t)=\theta_0+\overline{\theta}(z)+\theta'(x,z,t), \tag{2.9}$$

where the deviation $\overline{\theta}$ is small compared to the reference value θ_0. The assumption of a hydrostatic background is then reflected in the equation

$$c_p\theta_0\frac{\mathrm{d}\overline{\Pi}}{\mathrm{d}z}=-g. \tag{2.10}$$

We insert the ansatz (2.8) into the Euler equations (2.1). Using the incompressible mass conservation (2.7) and neglecting products that include at least two of the primed variables as they are considered too small to influence the dynamic, we obtain

$$\frac{\partial u'}{\partial t}+\overline{u}\frac{\partial u'}{\partial x}+w'\frac{\mathrm{d}\overline{u}}{\mathrm{d}z}+c_p\theta_0\left(1+\frac{\overline{\theta}}{\theta_0}\right)\frac{\partial \Pi'}{\partial x}=0, \tag{2.11a}$$

$$\frac{\partial w'}{\partial t} + \overline{u}\frac{\partial w'}{\partial x} + c_p\theta_0\left(1+\frac{\overline{\theta}}{\theta_0}\right)\frac{\mathrm{d}\overline{\Pi}}{\mathrm{d}z} + c_p\theta_0\left(1+\frac{\overline{\theta}}{\theta_0}\right)\frac{\partial \Pi'}{\partial z} + c_p\theta'\frac{\mathrm{d}\overline{\Pi}}{\mathrm{d}z} = -g, \tag{2.11b}$$

$$\frac{\partial \theta'}{\partial t} + \overline{u}\frac{\partial \theta}{\partial x} + w'\frac{\mathrm{d}\overline{\theta}}{\mathrm{d}z} = 0 \tag{2.11c}$$

$$\frac{\partial u'}{\partial x} + \frac{\partial w'}{\partial z} = 0. \tag{2.11d}$$

By what we said earlier, the deviations of potential temperature are small, hence we approximate

$$\left(1+\frac{\overline{\theta}}{\theta_0}\right) \approx 1. \tag{2.12}$$

Using additionally the hydrostatic balance (2.10), we obtain the system

$$\frac{\partial u'}{\partial t} + \overline{u}\frac{\partial u'}{\partial x} + w'\frac{\mathrm{d}\overline{u}}{\mathrm{d}z} + c_p\theta_0\frac{\partial \Pi'}{\partial x} = 0, \tag{2.13a}$$

$$\frac{\partial w'}{\partial t} + \overline{u}\frac{\partial w'}{\partial x} + c_p\theta_0\frac{\partial \Pi'}{\partial z} - \frac{g\theta'}{\theta_0} = 0, \tag{2.13b}$$

$$\frac{\partial \theta'}{\partial t} + \overline{u}\frac{\partial \theta}{\partial x} + w'\frac{\mathrm{d}\overline{\theta}}{\mathrm{d}z} = 0 \tag{2.13c}$$

$$\frac{\partial u'}{\partial x} + \frac{\partial w'}{\partial z} = 0. \tag{2.13d}$$

We refer to system (2.13) as the linearised Boussinesq equations and they will be the starting point for further investigations.

3 Transmission and reflection of plane waves in an atmosphere at rest

In this chapter, we derive a one-step method to find an approximate solution for equation system (2.13) in case of non-uniform stratification and steady background wind. From this solution, we are able to compute a transmission coefficient for plane waves propagating through a region of non-uniform stratification. The foundation for the transmission coefficient is the conservation of energy, which will be derived directly from equation system (3.1).

Except for sections 3.1 and 3.4, the work presented in this chapter is based on a manuscript (Pütz et al., 2018), which has been submitted to a peer-reviewed journal and we closely follow the structure therein.

3.1 The Taylor-Goldstein equation

We consider an hydrostatic atmosphere at rest, i.e. $\overline{u} \equiv 0$. Using this in equation system (2.13) and omitting the primes for the sake of clarity, we obtain the following equations:

$$\frac{\partial u}{\partial t} + c_p\theta_0\frac{\partial \Pi}{\partial x} = 0, \tag{3.1a}$$

$$\frac{\partial w}{\partial t} + c_p\theta_0\frac{\partial \Pi}{\partial z} - \frac{g\theta}{\theta_0} = 0, \tag{3.1b}$$

$$\frac{\partial \theta}{\partial t} + w\frac{\mathrm{d}\overline{\theta}}{\mathrm{d}z} = 0, \tag{3.1c}$$

$$\frac{\partial u}{\partial x} + \frac{\partial w}{\partial z} = 0. \tag{3.1d}$$

These equations can be combined to a single equation for one of the variables u, w, θ or Π. We choose the vertical wind w as our variable of interest and will stick with this for the remainder of the thesis. Taking the curl of the momentum equations (3.1a) and (3.1b), we obtain

$$\frac{\partial^2 u}{\partial z \partial t} - \frac{\partial^2 w}{\partial x \partial t} + \frac{g}{\theta_0}\frac{\partial \theta}{\partial x} = 0. \tag{3.2}$$

Taking the x-derivative of this equation and using the divergence constraint (3.1d) yields

$$-\frac{\partial^3 w}{\partial z^2 \partial t} - \frac{\partial^3 w}{\partial x^2 \partial t} + \frac{g}{\theta_0}\frac{\partial^2 \theta}{\partial x^2} = 0. \tag{3.3}$$

For the final step, we take the t-derivative of this equation and plug in the entropy equation (3.1c). Together with the definition

$$N^2 = \frac{g}{\theta_0}\frac{\mathrm{d}\overline{\theta}}{\mathrm{d}z} \tag{3.4}$$

for the Brunt-Väisälä frequency in the Boussinesq framework, we obtain the following equation:

$$\left(\frac{\partial^2}{\partial x^2} + \frac{\partial^2}{\partial z^2}\right)\frac{\partial^2 w}{\partial t^2} + N^2 \frac{\partial^2 w}{\partial x^2} = 0. \tag{3.5}$$

The Brunt-Väisälä frequency N is sometimes also called buoyancy frequency. This is the frequency an air parcel would oscillate with when displaced adiabatically in vertical direction. In atmospheric science, it is used as a measure for strength of the stratification. Higher values, i.e. higher frequencies, lead to faster oscillations, resulting from a stronger restoring force. Therefore, N is often referred to as *stratification*, where stronger stratification is equivalent to higher values of N.

As we assume a horizontally homogeneous background as well as a time independence, the equation admits solutions of the form

$$w(x,z,t) = \hat{w}(z)\exp(i(kx - \omega t)), \tag{3.6}$$

where k is the horizontal wavenumber and ω is the frequency. By convention, we only consider $\omega > 0$ and discuss the case $k > 0$, as the case for $k < 0$ is completely symmetric. With these assumptions, the horizontal phase velocity ω/k points in positive x-direction. Equation (3.5) then reduces to an ordinary differential equation (ODE), also known as the Taylor-Goldstein equation:

$$\frac{\mathrm{d}^2\hat{w}}{\mathrm{d}z^2} + k^2\left(\frac{N^2}{\omega^2} - 1\right)\hat{w} = 0. \tag{3.7}$$

If N depends on z, this equation has no general solution, except for maybe some special cases. But if $N \equiv N_0$ is constant, a plane wave solution

$$\hat{w}(z) = A\exp(-imz) + B\exp(imz) \tag{3.8}$$

exists, where A and B are constants and

$$m = -k\sqrt{\frac{N_0^2}{\omega^2} - 1} \tag{3.9}$$

is the vertical wavenumber. We choose the complex representation of the solution over, e.g., a cosine representation, because we can distinguish between upward- and downward propagating wave components. It basically is a Fourier transform, followed up by a bandpass filtering so that the real solution corresponds to the real part of the complex representation. We will see shortly that this representation is very useful.

We can use the fact that plane wave solutions exist in the case of a uniform background to derive polarization relations for the wave fields u, θ and Π subject to w. The divergence equation (3.1d) yields

$$u = -\frac{m}{k}w, \tag{3.10}$$

which means that the wind amplitudes scale with the wavenumbers and that both are out of phase by 180 degree (u is maximal where w is minimal and vice versa).

The entropy equation (3.1c), divided by $\theta_0 g^-1$, gives

$$\frac{g\theta}{\theta_0} = -i\frac{N^2}{\omega}w. \tag{3.11}$$

The term $\frac{g\theta}{\theta_0}$ is commonly named as wave or perturbation buoyancy (Achatz et al., 2010). It is out of phase with the vertical wind by 270 degree, meaning that one of the fields attains the extremal values while the other is 0.

Finally, the horizontal momentum equation (3.1a) equation, together with the polarisation for u yields

$$\Pi = -\frac{m}{k^2}\frac{\omega}{c_p\theta_0}w. \tag{3.12}$$

Like the horizontal wind, the pressure is out of phase by 180 degree with the vertical wind. This in turn means also that pressure and horizontal wind are in phase, obtaining their maxima and minima at the same locations.

3.2 The multi-layer method

The main focus of this work is the interaction of gravity waves with the tropopause. The latter is characterised by strong variations in stratification and wind, but also by a short vertical extent. Moreover, the stratification in the troposphere and stratosphere can safely assumed to be uniform (although not equal in terms of strength, see for example Birner et al. (2002), Gettelman et al. (2011)). This means that in the troposphere and stratosphere, equation (3.7) can be solved explicitly with solutions of the form (3.8). To be precise, we are given a function

$$N(z) = \begin{cases} N_b, & z < z_b \\ N_c(z), & z_b \leq z \leq z_t \\ N_t, & z > z_t, \end{cases} \tag{3.13}$$

where z_b, z_t are the bottom and top of the tropopause, respectively (or any region of interest in general), N_b, N_t are constant values of N in the bottom and top layer, respectively, and N_c is a continuous[1] function of z with $N_c(z_b) = N_b$ and $N_c(z_t) = N_t$. The tropospheric solution is

$$\hat{w}(z) = A_b \exp(i m_b z) + B_b \exp(-i m_b z), \tag{3.14}$$

with $m_b = -k\sqrt{N_b^2/\omega^2 - 1}$. For the stratospheric solution, we replace the subscript b by t. The solution in the tropopause region remains still unknown.

We are going to make use of the fact that solutions to equation (3.7) exist for constant stratification and approximate N_c by a piecewise-constant function. For each constant section, we can find an explicit solution and each local solution needs to be matched to its neighbours. This will yield an approximate solution of equation (3.7), where we can distinguish upward and downward propagating waves. The ansatz itself goes back to Eliassen and Palm (1961), but we are the first one to carry out extensive computations as well as convergence studies. Moreover, we use the fact that we can distinguish the wave propagation directions to compute a transmission coefficient, which relates the upward vertical wave energy flux below and above the tropopause region. Although the ansatz might seem simple, it will turn out that it will deliver accurate solutions that can be computed very fast.

We start with a technical introduction of the setup. Let J be a positive integer that, for now, remains fixed. This corresponds to the number of jumps we have in the piecewise-constant approximation. We define an equidistant grid of J points from z_b to z_t, including both end points:

$$z_j = z_b + \frac{j-1}{J-1}(z_t - z_b) \text{ for } j = 1, \ldots, J. \tag{3.15}$$

This gives rise to a partition into $J+1$ layers I_j with $I_j = [z_{j-1}, z_j)$ for $j = 2, \ldots, J$, I_1 the troposphere region $z < z_b$ and I_{J+1} the stratosphere region $z \geq z_t$. We set

---

[1] Continuity is not necessary, as the multi-layer method would also work with discontinuous functions, but we will assume the continuity of N throughout this work.

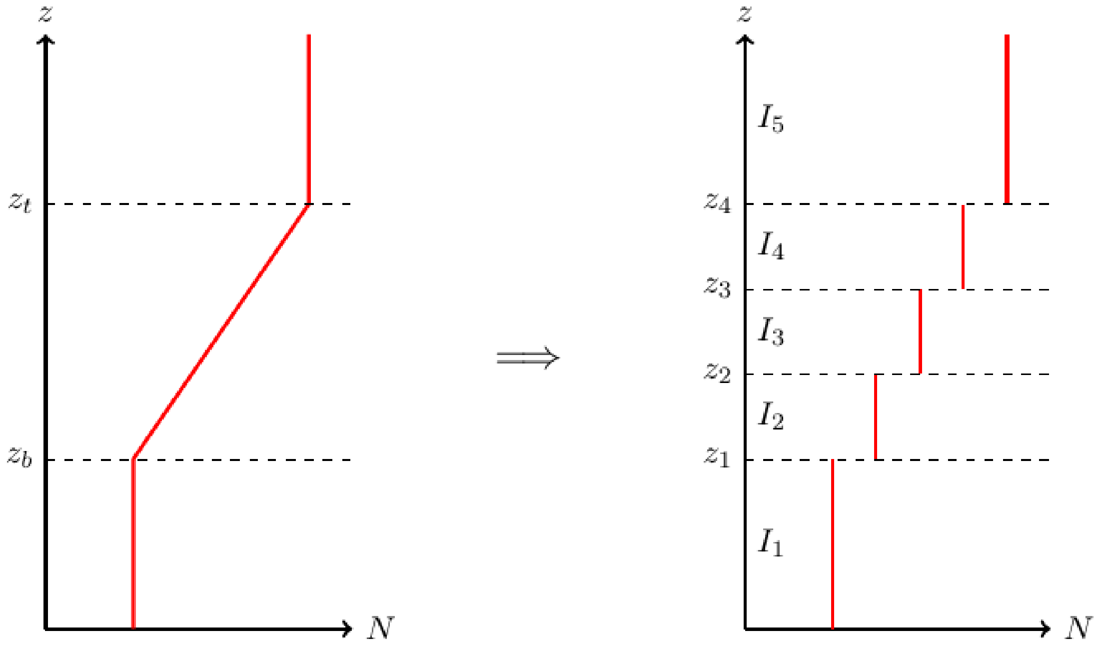

Figure 3.1: Schematic discretisation of a linearly increasing function for N

$N_1 = fN(z_1) = N_b, N_{J+1} = N(z_J) = N_t$ and

$$N_j := N\left(\frac{z_j + z_{j-1}}{2}\right) \quad \text{for } j = 2, ..., J. \tag{3.16}$$

This can be understood as a piecewise function

$$\tilde{N}(z) = N_j, z \in I_j, \tag{3.17}$$

In each single layer, we are able to state the Taylor-Goldstein equation, but with a constant value for N. In particular, for the layer I_j, the equation writes down as

$$\frac{\mathrm{d}^2 w_j}{\mathrm{d}z^2} + k^2 \left(\frac{N_j^2}{\omega^2} - 1\right) w_j = 0. \tag{3.18}$$

Each layer admits explicit plane wave solutions of the form

$$w_j(z) = A_j \exp(im_j z) + B_j \exp(-im_j z), \tag{3.19}$$

where

$$m_j = -k\sqrt{\frac{N_j^2}{\omega^2} - 1} \tag{3.20}$$

is the vertical wavenumber and A_j and B_j are the amplitudes of the upward and downward propagating wave, respectively.

All variables indexed by $j \in \{1, \ldots, J+1\}$ defined above depend implicitly on the (fixed) number J, i.e. for $J_1 \neq J_2$, we have $N_j^{(J_1)} \neq N_j^{(J_2)}$ in general, where the superscript here should reflect the dependence on the number of levels. To be precise and keep the variables comparable, one could index them by j/J or add the number of jumps as a superscript. But apart from being harder tor read, it does not provide further benefit, since most of the time, we are interested in the variables indexed with 1 and $J+1$. Therefore, stick with the notation above, but keep this dependence in mind.

The solution with indices 1 and $J+1$ correspond to the tropospheric and stratospheric solution respectively. We want to investigate waves that are incident on the tropopause from below with amplitude A_1. Since the stratosphere is uniformly stratified, we assume a radiation condition, i.e. that waves, once reached the stratosphere, do not reflect any longer but propagate upwards[2]. Hence, $B_{J+1} = 0$. Then, A_{J+1} corresponds to the transmitted amplitude and B_1 to the reflected amplitude.

To obtain a global solution, we have to match the local solutions at the interfaces in a proper way. Physically meaningful conditions require that the vertical wind speed and the pressure are continuous across the interface (see also Drazin and Reid (1981)). By using the horizontal momentum equation (3.1a), the divergence constraint (3.1d) and the plane wave ansatz (3.6), second condition is equivalent to the requirement that $w_j' = \mathrm{d}w_j/\,\mathrm{d}z$ is continuous across the interfaces. This can also be derived directly from the polarisation relation (3.12), when the factor im is replaced by the vertical derivative. Together, we can write the matching conditions as

$$\mathit{\Delta}\left[w\right](z_j) = 0, \tag{3.21a}$$

$$\mathit{\Delta}\left[w'\right](z_j) = 0. \tag{3.21b}$$

at each layer interface, where

$$\mathit{\Delta}[f](z_0) = \lim_{\delta\to 0^-} f(z_0+\delta) - \lim_{\delta\to 0^+} f(z_0+\delta) \tag{3.22}$$

is called the jump of f at z_0. In our setup, this writes as

$$w_j(z_j) = w_{j+1}(z_j), \tag{3.23a}$$

---

[2] This is of course only partially true. There could be stratospheric jets or the stratopause which could cause partial reflection of the upward propagating waves. But since our interest is on the wave-tropopause interaction, the assumption is justified.

$$w_j'(z_j) = w_{j+1}'(z_j). \tag{3.23b}$$

This turns out to be also mathematically meaningful. Since we construct an approximate solution for a second order ordinary differential equation, the solution should be at least continuously differentiable once.

For fixed $j \in \{1, \dots, J\}$, a pair of the form (3.23) gives us two equations for the four unknowns $A_j, B_j, A_{j+1}, B_{j+1}$. Hence, we are able to derive a recurrence relation

$$\begin{pmatrix} A_{j+1} \\ B_{j+1} \end{pmatrix} = \boldsymbol{M}_j \begin{pmatrix} A_j \\ B_j \end{pmatrix}, \tag{3.24}$$

where $\boldsymbol{M}_j$ is a 2-by-2 matrix. Its entries can be found by plugging in the local solutions (3.19) at z_j and solving the system for A_{j+1} and B_{j+1}:

$$\begin{aligned} &A_j \exp(im_j z_j) + B_j \exp(-im_j z_j) \\ &\qquad = A_{j+1} \exp(im_{j+1} z_j) + B_{j+1} \exp(-im_{j+1} z_j), \end{aligned} \tag{3.25a}$$

$$\begin{aligned} &im_j A_j \exp(im_j z_j) - im_j B_j \exp(-im_j z_j) \\ &\qquad = im_{j+1} A_{j+1} \exp(im_{j+1} z_j) - im_{j+1} B_{j+1} \exp(-im_{j+1} z_j), \end{aligned} \tag{3.25b}$$

which simplifies to

$$A_{j+1} = \frac{m_j + m_{j+1}}{2m_{j+1}} \exp(i(m_j - m_{j+1})z_j) A_j - \frac{m_j - m_{j+1}}{2m_{j+1}} \exp(-i(m_j + m_{j+1})z_j) B_j, \tag{3.26a}$$

$$B_{j+1} = -\frac{m_j - m_{j+1}}{2m_{j+1}} \exp(i(m_j + m_{j+1})z_j) A_j + \frac{m_j + m_{j+1}}{2m_{j+1}} \exp(-i(m_j - m_{j+1})z_j) B_j. \tag{3.26b}$$

The coefficients of A_j and B_j are the matrix entries of $\boldsymbol{M}_j$. We can see similarities in the coefficients. In fact, the matrix has the shape

$$\boldsymbol{M}_j = \begin{pmatrix} c_j & d_j \\ d_j^* & c_j^* \end{pmatrix}. \tag{3.27}$$

where the matrix entries are given by

$$c_j = \frac{m_j + m_{j+1}}{2m_{j+1}} \exp(i(m_j - m_{j+1})z_j) \tag{3.28a}$$

$$d_j = -\frac{m_j - m_{j+1}}{2m_{j+1}} \exp(-i(m_j + m_{j+1})z_j). \tag{3.28b}$$

The entries superscripted with a star only differ from their non-superscripted counterparts by the sign in the exponential term. In order to be able to refer to this later, we define the *-operation which changes the sign of the argument of the exp-function, i.e.,

$$c_j^* = \frac{m_j + m_{j+1}}{2m_{j+1}} \exp(-i(m_j - m_{j+1})z_j) \tag{3.29a}$$

$$d_j^* = -\frac{m_j - m_{j+1}}{2m_{j+1}} \exp(i(m_j + m_{j+1})z_j). \tag{3.29b}$$

As long as m_j and m_{j+1} are real-valued, this corresponds to the usual complex conjugation. Imaginary values for m occur only when the waves are encountering a region of decreased stratification, where $N < \omega$. We will see later that these cases are harder to deal with analytically, hence they have to be treated very carefully. A necessary and sufficient condition for $\boldsymbol{M}_j$ to be the zero matrix is that $m_j + m_{j+1} = 0$ and $m_j - m_{j+1} = 0$ hold at the same time. We will discuss this possibility towards the end of this section.

The determinant of $\boldsymbol{M}_j$ is given by

$$\begin{aligned} \det(\boldsymbol{M}_j) &= c_j c_j^* - d_j d_j^* \\ &= \frac{(m_j + m_{j+1})^2}{4m_{j+1}^2} - \frac{(m_j - m_{j+1})^2}{4m_{j+1}^2} \\ &= \frac{4m_j m_{j+1}}{4m_{j+1}^2} \\ &= \frac{m_j}{m_{j+1}} \end{aligned} \tag{3.30}$$

Unless either of the values m_j or m_{j+1} equals 0, the matrices are well-defined and of full rank. By definition of m_j (3.20), it can only be zero if $N_j = \omega$. If this happens, the matching between those two layers fail. Mathematically, the reason for this is that in the case of $m_j = 0$, the solutions of equation (3.18) differ qualitatively from the case $m_j \neq 0$, be it real or imaginary. In the former case, the corresponding first-order system has no longer two different eigenvalues m_j and $-m_j$, but only one. Therefore the solution is of the form

$$w = A + Bz, \tag{3.31}$$

i.e. a linear function (the exp-expressions reduce to 1, as the corresponding eigenvalue is 0).

If $N = \omega$ only holds at isolated points for the stratification profile, we can mitigate the problem. If the multi-layer method should hit that point such that for some layer j, we have $N_j = \omega$, a simple workaround is to split the layer j into two new layers $j + \frac{1}{2}$ and $j + \frac{3}{2}$ with $N_{j+\frac{1}{2}} > \omega$ and $N_{j+\frac{3}{2}} < \omega$ and match those two layers. We will see later, that this does not affect the convergence of the method.

If $N = \omega$ holds over an interval $[z_r, z_s]$ with $z_r \neq z_s$, the workaround is as follows: We split the domain in multiple parts, distinguishing between parts with $N \neq \omega$ and $N = \omega$. We use the multi-layer method in the parts with $N \neq \omega$. For the parts with $N = \omega$, equation (3.18) has an explicit solution with boundary conditions given by their adjacent domains. This will, at least, be an approximate solution to equation (3.7) in the sense of section 3.4, but we lose the possibility to keep track of upward and downward propagating wave components.

So for now, we assume that $N = \omega$ only holds at isolated points. This also guarantees that none of the matrices is the zero matrix.

3.3 Transmission coefficient

In order to compute a meaningful transmission coefficient, we need to find a quantity that is conserved over the whole domain. Since we did not allow for dissipation or background horizontal wind in the equations, wave energy (sometimes called perturbation energy) is conserved. The conservation equations can be derived directly from the Boussinesq equations (3.1). Multiplying $u, w, g\theta/(\overline{\theta}N^2)$ with the first, second and third equation respectively, adding them and using the divergence constraint (3.1d), we derive

$$\frac{\partial E}{\partial t} + c_p\overline{\theta}\rho_b\left(\frac{\partial u\Pi}{\partial x} + \frac{\partial w\Pi}{\partial z}\right) = 0, \tag{3.32}$$

where

$$E = \frac{\rho_b}{2}\left(u^2 + w^2 + \left(\frac{g\theta}{\theta_0 N}\right)^2\right) \tag{3.33}$$

and ρ_b is the background density. The first two terms in the large parenthesis reflect the kinetic energy while the last term is the potential energy. The physical dimension of E is J/m^3, i.e. energy per unit volume. Therefore, the term energy density is often used synonymously for E. Energy can be derived from this expression by integrating over a fixed control volume, but for our purposes, it is sufficient to take the energy density. Since there is no danger of confusion, we stick with the terminology “(wave) energy” for E. It is also important to note that when using the complex representations for the wave fields, we have to be careful, since the real solution consists only of the real part of the full complex representation, so for any of the fields $f \in \{u, w, \theta\}$, f^2 has to be understood as $\Re(f)^2$.

Using the polarisation relations (3.10), (3.11) and (3.12), equation (3.32) can be rewritten as

$$\frac{\partial E}{\partial t} + \nabla \cdot (\vec{c}_g E) = 0, \tag{3.34}$$

with the group velocity vector

$$\vec{c}_g = \left(\frac{\partial \omega}{\partial k}, \frac{\partial \omega}{\partial m}\right) = \left(\frac{Nm^2}{\sqrt{k^2+m^2}^3}, \frac{-Nkm}{\sqrt{k^2+m^2}^3}\right). \tag{3.35}$$

In our setup, it is convenient to a look at the horizontally averaged energy, since we have a horizontally periodic domain. The formula for wave energy averaged over a horizontal wavelength is given by

$$\langle E \rangle = \frac{k}{2\pi}\int_0^{\frac{2\pi}{k}} E \, \mathrm{d}x = \frac{k}{2\pi}\frac{\rho_b}{2}\int_0^{\frac{2\pi}{k}} \left(|u|^2 + |w|^2 + \left|\frac{g\theta}{\theta_0 N}\right|^2\right) \mathrm{d}x. \tag{3.36}$$

Assuming constant stratification, we can represent each field $f \in \{u, w, \theta\}$ as a plane wave $f = A_f \exp(i(kx + mz - \omega t))$. Hence, we find that

$$\begin{aligned}\int_0^{\frac{2\pi}{k}} \Re(f)^2 \, \mathrm{d}x &= \int_0^{\frac{2\pi}{k}} \left(\Re(A_f)\cos(kx) + \Im(A_f)\sin(kx)\right)^2 \mathrm{d}x \\ &= \Re(A_f)^2 \int_0^{\frac{2\pi}{k}} \cos^2(kx)\, \mathrm{d}x + \Im(A_f)^2 \int_0^{\frac{2\pi}{k}} \sin^2(kx)\, \mathrm{d}x \\ &\quad + \Re(A_f)\Im(A_f)\int_0^{\frac{2\pi}{k}} \cos(kx)\sin(kx)\, \mathrm{d}x\end{aligned} \tag{3.37}$$

The antiderivatives of $\cos^2(kx)$, $\sin^2(kx)$ and $\sin(kx)\cos(kx)$ are

$$\int \cos^2(kx) = \frac{\cos(kx)\sin(kx) + kx}{2k} + c, \tag{3.38}$$

$$\int \sin^2(kx) = \frac{-\cos(kx)\sin(kx) + kx}{2k} + c, \tag{3.39}$$

$$\int \sin(kx)\cos(kx) = \frac{\sin^2(kx)}{2k} + c, \tag{3.40}$$

where c is an arbitrary real constant. Hence, the integral 3.37 solves to

$$\int_0^{\frac{2\pi}{k}} \Re(f)^2 \, \mathrm{d}x = \Re(A_f)^2 \frac{\pi}{k} + \Im(A_f)^2 \frac{\pi}{k} + 0 = |A_f|^2 \frac{\pi}{k}. \tag{3.41}$$

Hence, the horizontally averaged energy can be written as

$$\langle E \rangle = \frac{\rho_b}{4}\left(|A_u|^2 + |A_w|^2 + \frac{g^2}{\theta_0^2 N^2}|A_\theta|^2\right). \tag{3.42}$$

The amplitudes of u and θ can be related to w via the polarisation relations (3.10) and (3.11):

$$|A_u|^2 + |A_w|^2 + \frac{g^2}{\theta_0^2 N^2} |A_\theta|^2 = \left(\frac{m^2}{k^2} + 1 + \frac{N^2}{\omega^2} \right) |A_w|^2 . \tag{3.43}$$

Using the dispersion relation (3.9), we find that

$$\frac{m^2 + k^2}{k^2} = \frac{N^2}{\omega^2}. \tag{3.44}$$

So we can finally write the horizontally averaged wave energy as

$$\langle E \rangle = \frac{1}{2} \rho_b \frac{N^2}{\omega^2} |A_w|^2 . \tag{3.45}$$

Horizontal averaging of equation (3.34) removes the x-derivative and yields

$$\frac{\partial \langle E \rangle}{\partial t} + \frac{\partial c_{g_z} \langle E \rangle}{\partial z} = 0, \tag{3.46}$$

where c_{g_z} denotes the second component of the group velocity (3.35), also called vertical group velocity. The term $c_{g_z} \langle E \rangle$ is often named vertical wave energy flux, written as $\langle \mathcal{F}_z \rangle$. Moreover, the average energy at a fixed location does not change in time, since we assumed the solution to be periodic in time. The remaining term, namely

$$\frac{\partial \langle \mathcal{F}_z \rangle}{\partial z} = 0 \tag{3.47}$$

basically says that the vertical mean wave energy flux is constant. When now comparing the tropospheric and stratospheric vertical wave energy flux, they have to be the same:

$$\langle \mathcal{F}_z \rangle_T = \langle \mathcal{F}_z \rangle_S \tag{3.48}$$

In the last subsection, we assumed no wave travelling downward in the stratosphere, but the troposphere can have downward travelling waves, namely waves that are (partially) reflected at the non-uniform stratification. So we have two wave fluxes in the troposphere with different directions:

$$\langle \mathcal{F}_z \rangle_{T,\text{up}} - \langle \mathcal{F}_z \rangle_{T,\text{down}} = \langle \mathcal{F}_z \rangle_{S,\text{up}} \tag{3.49}$$

Rewriting the equation yields

$$\frac{\langle \mathcal{F}_z \rangle_{S,\text{up}}}{\langle \mathcal{F}_z \rangle_{T,\text{up}}} + \frac{\langle \mathcal{F}_z \rangle_{T,\text{down}}}{\langle \mathcal{F}_z \rangle_{T,\text{up}}} = 1. \tag{3.50}$$

Assuming that $\langle \mathcal{F}_z \rangle_{T,\mathrm{up}}$ is the energy flux caused by the incident wave, the first term on the left hand side is the ratio of transmitted upward wave energy flux and incident upward wave energy flux. This is what we will use as *transmission coefficient*. Likewise, the second term can be seen as a reflection coefficient. As we can see from the equation, transmission and reflection coefficient add up to 1, as it should be, since we started the derivation with a conservation law.

Using the formula for vertical group velocity (3.35) and horizontally averaged wave energy (3.45), we can write the vertical wave energy flux as

$$\langle \mathcal{F}_z \rangle = \frac{-N^3 k m \rho_b}{2\omega^2 \sqrt{k^2+m^2}^3} \left| A_w \right|^2 . \tag{3.51}$$

By using the dispersion relation (3.9), solved for ω, we obtain that

$$\langle \mathcal{F}_z \rangle = \frac{-\rho_b m \omega}{2k^2} \left| A_w \right|^2 . \tag{3.52}$$

We made the assumption that the density does not vary too much over the tropopause, so that we stick with the reference value ρ_b for both troposphere and stratosphere. Then, everything except for m and A_w is constant. Therefore, we can compute the transmission coefficient as

$$TC = \frac{\langle \mathcal{F}_z \rangle_{S,\mathrm{up}}}{\langle \mathcal{F}_z \rangle_{T,\mathrm{up}}} = \frac{m_{J+1} \left| A_{J+1} \right|^2}{m_1 \left| A_1 \right|^2} . \tag{3.53}$$

In a similar fashion we can define a reflection coefficient, which compares the upward flux with the downward flux below the tropopause:

$$RC = \frac{\left| B_1 \right|^2}{\left| A_1 \right|^2} \tag{3.54}$$

An interesting observation that we obtain from equation (3.53) is that for a perfect transmission, i.e. $TC = 1$, the transmitted amplitude scales with the square root of the wavenumber ratio. In particular, we have

$$\left| A_{J+1} \right| = \sqrt{\frac{m_1}{m_{J+1}}} \left| A_1 \right| . \tag{3.55}$$

So a stronger stratification in the stratosphere results in a larger vertical wavenumber and therefore in a smaller wave amplitude. This observation will arise again in chapter 7, where we investigate the governing equations for different scaling regimes.

The next task is to relate A_1 and A_{J+1}. We can state a relation like equation (3.24) for all $j = 1, \dots, J$ and combine them to obtain a chain of equations:

$$\begin{pmatrix} A_{J+1} \\ B_{J+1} \end{pmatrix} = \boldsymbol{M}_J \begin{pmatrix} A_J \\ B_J \end{pmatrix} = \boldsymbol{M}_J \boldsymbol{M}_{J-1} \begin{pmatrix} A_{J-1} \\ B_{J-1} \end{pmatrix} = \ldots = \underbrace{\prod_{j=J}^{1} \boldsymbol{M}_j}_{=:\boldsymbol{M}} \begin{pmatrix} A_1 \\ B_1 \end{pmatrix} \tag{3.56}$$

We have to be careful about the order of the matrix multiplication, since it is in general not commutative. By assumption, $B_{J+1} = 0$. So we have

$$A_{J+1} = M_{1,1} A_1 + M_{1,2} B_1 \tag{3.57}$$

$$0 = M_{2,1} A_1 + M_{2,2} B_1, \tag{3.58}$$

where $M_{k,l}$ are the entries of $\boldsymbol{M}$. This gives two equations for three unknowns. Hence we can relate any two of the unknowns. Solving the equation system for A_1 and A_{J+1} shows that

$$\frac{A_{J+1}}{A_1} = \left(M_{1,1} - \frac{M_{1,2} M_{2,1}}{M_{2,2}} \right) = \frac{\det(\boldsymbol{M})}{M_{2,2}}. \tag{3.59}$$

We can compute $\det(\boldsymbol{M})$ with the help of equations (3.56), (3.30) and the fact that the determinant is multiplicative:

$$\det(\boldsymbol{M}) = \det(\prod_{j=J}^{1} \boldsymbol{M}_j) = \prod_{j=J}^{1} \det(\boldsymbol{M}_j) = \prod_{j=J}^{1} \frac{m_j}{m_{j+1}} = \frac{m_1}{m_{J+1}}. \tag{3.60}$$

The final formula for the transmission coefficient then reads

$$TC = \frac{m_{J+1}}{m_1} \left| \frac{\det(M)}{M_{2,2}} \right|^2 = \frac{m_1}{m_{J+1} \left| M_{2,2} \right|^2}. \tag{3.61}$$

Mathematically, we can see the transmission coefficient as a real-valued function of ω and k, for a fixed profile N. It is composed of multiple functions that depend on ω and k, namely the wavenumbers m_j in the respective layers. They are clearly continuous in k, but the continuity in ω is not clear at first sight, since we have a square root involved. As it is well known, the complex square root function is not unconditionally continuous, as we have two branches that overlap at one half-axis in the complex plane. We have, however, only real radicands, restricting the function from $\mathbb{R}$ to $\mathbb{C}$. Seeing this as a function between metric spaces, where $\mathbb{R}$ and $\mathbb{C}$ are equipped with the usual metrics, it is possible to show that m_j is continuous as a function of ω.

Claim 3.3.1. *Let $k, N_j \in \mathbb{R}$ be constant. Then, the function*

$$m_j \colon (0,\infty) \to \mathbb{C},\ \omega \mapsto k\sqrt{\frac{N_j^2}{\omega^2} - 1} \tag{3.62}$$

is continuous in ω for any choice $k, N_j \in \mathbb{R}$.

Proof. m_j is the composition of two functions f and g with

$$f \colon \mathbb{R} \to \mathbb{C},\, x \mapsto f(x) = \begin{cases} \sqrt{x}, & x \geq 0 \\ i\sqrt{|x|}, & x < 0 \end{cases} \tag{3.63}$$

$$g \colon (0,\infty) \to \mathbb{C},\, \omega \mapsto \frac{N_j^2}{\omega^2} - 1, \tag{3.64}$$

such that $m_j(\omega) = k \cdot f(g(\omega))$. So if f and g are continuous, so would be m_j as a composition of continuous functions. g is clearly continuous, as $h(x) = \frac{1}{x^2}$ is continuous for the positive real numbers and multiplication and addition of constants do not affect continuity. For the continuity of f, we use the $\epsilon - \delta$ definition, i.e. we show that

$$\forall x_0 \in \mathbb{R} : \forall \epsilon > 0 \exists \delta > 0 : \forall x \in \mathbb{R} \text{ with } |x_0 - x| < \delta \Rightarrow \|f(x_0) - f(x)\| < \epsilon \tag{3.65}$$

Here, $\|z\| = \|x + iy\| = \sqrt{x^2 + y^2}$ is the usual norm for complex numbers. Note that $\|x\| = |x|$ for $x \in \mathbb{R}$. We have to distinguish four cases, since both x_0 and x can be positive or negative.

1. $x_0 \geq 0, x \geq 0$
   Then $f(x_0), f(x) \in \mathbb{R}$

   $$\|f(x_0) - f(x)\| = \|\sqrt{x_0} - \sqrt{x}\| = \sqrt{(\sqrt{x_0} - \sqrt{x})^2} = \left|\sqrt{x_0} - \sqrt{x}\right| \tag{3.66}$$

   Using that $|x - y| \leq |x + y|$ for $x, y \geq 0$, we obtain

   $$\|f(x_0) - f(x)\|^2 = \left|\sqrt{x_0} - \sqrt{x}\right|^2 \leq \left|\sqrt{x_0} - \sqrt{x}\right| \left|\sqrt{x_0} + \sqrt{x}\right| \leq |x_0 - x| < \delta. \tag{3.67}$$

   So we choose $\delta = \epsilon^2$.

2. $x_0 < 0, x < 0$
   Then $f(x_0), f(x) \in i\mathbb{R}$

   $$\|f(x_0) - f(x)\| = \|i\sqrt{|x_0|} - i\sqrt{|x|}\| = \sqrt{(\sqrt{|x_0|} - \sqrt{|x|})^2} = \left|\sqrt{|x_0|} - \sqrt{|x|}\right| \tag{3.68}$$

Using the same inequality as in the first case, we obtain

$$\begin{aligned}\|f(x_0)-f(x)\|^2 &= \left|\sqrt{|x_0|}-\sqrt{|x|}\right|^2 \leq \left|\sqrt{|x_0|}-\sqrt{|x|}\right|\left|\sqrt{|x_0|}+\sqrt{|x|}\right| \\ &\leq \left||x_0|-|x|\right| = |x_0-x| < \delta.\end{aligned} \tag{3.69}$$

The last equality follows from the fact that both x_0 and x are negative. Again, we can choose $\delta = \epsilon^2$.

3. $x_0 \geq 0, x < 0$
   Then

   $$\begin{aligned}\|f(x_0)-f(x)\| &= \|\sqrt{x_0}-i\sqrt{|x|}\| = \sqrt{\sqrt{x_0}^2+\sqrt{|x|}^2} = \sqrt{x_0+|x|} \\ &= \sqrt{x_0-x} = \sqrt{|x_0-x|} < \sqrt{\delta}.\end{aligned} \tag{3.70}$$

   The last second-to last equality follows from the definition of the absolute value, the last equality from the fact that the radicand is positive and the last inequality holds since the square root is strictly monotonically increasing on $\mathbb{R}_{\geq 0}$. So we can choose $\delta = \epsilon^2$.

4. $x_0 < 0, x \geq 0$
   Then

   $$\begin{aligned}\|f(x_0)-f(x)\| &= \|i\sqrt{|x_0|}-\sqrt{x}\| = \sqrt{\sqrt{|x_0|}^2+\sqrt{x}^2} = \sqrt{|x_0|+x} \\ &= \sqrt{x-x_0} = \sqrt{|x-x_0|} = \sqrt{|x_0-x|} < \sqrt{\delta}.\end{aligned} \tag{3.71}$$

   The same reasoning as in the third case hold at the respective positions. The last equality comes from the fact that $|a-b| = |b-a|$. Again, we choose $\delta = \epsilon^2$. This concludes the proof.

□

Now that we know that all functions m_j are continuous in k and ω, also arithmetic operations involving them will yield in continuous functions (as long as we do not divide by 0). Finally, we take the absolute value, but that does not affect the continuity[3]. Therefore, if $m_j \neq 0$ for all j, the transmission coefficient is a continuous function. As we said at the end of section 3.2, $m_j = 0$ occurs, when $N_j = \omega$. If this happens at an isolated point (which would be $(z_{j+1}+z_j)/2$ in this case), we can bypass the problem without affecting the solution. We will discuss the case $N = \omega$ closer in subsection 3.6.2.

---

[3] If anything, it would have even better continuity properties than the complex square root function, as the absolute value of the square root is continuous in $\mathbb{C}$.

3.4 Proof of convergence and construction of a finite element solution

The proof of convergence for the multi-layer scheme is based on the theory developed in Lara (2004). It is about the convergence of a one-step method for autonomous systems of ordinary differential equations. By rewriting equation (3.7) as a first-order system

$$\begin{pmatrix} w \\ q \end{pmatrix}' = \begin{pmatrix} 0 & 1 \\ -m^2(z) & 0 \end{pmatrix} \begin{pmatrix} w \\ q \end{pmatrix}, \tag{3.72}$$

the multi-layer method can be written down as a one-step method that fulfils the requirements in Lara (2004). In particular, given a point z_0, initial conditions w_0, q_0 and a step size h, we solve the constant-coefficient system

$$\begin{pmatrix} w^{(1)} \\ q^{(1)} \end{pmatrix}' = \begin{pmatrix} 0 & 1 \\ -m^2(z_0 + \frac{h}{2}) & 0 \end{pmatrix} \begin{pmatrix} w^{(1)} \\ q^{(1)} \end{pmatrix}, \tag{3.73}$$

due to the initial conditions $w^{(1)}(z_0) = w_0, q^{(1)}(z_0) = q_0$) and set $w_1 = w^{(1)}(z_0 + h)$, $q_1 = q^{(1)}(z_0 + h)$, which are the initial conditions for the next step. Since $q = w'$ (can be seen from the first row of the equation system (3.72)), the global solution as well as its derivative are continuous. This corresponds to the matching conditions (3.23). Due to Lara (2004), such one-step methods for first-order systems converge to the solution of the corresponding system. But the one-step method from equation (3.73) is equivalent to the multi-layer method, as the eigenvalues of the matrix are $\pm im(z_0 + \frac{h}{2})$ and the solution is a linear combination of the exponentials of the eigenvalues, which is exactly the same as for the multi-layer method.

To see how a solution to equation (3.7) is actually constructed from this method, we will have a look at the following case study. We show the results for equation (3.7), where N was taken to be a linearly increasing profile

$$N(z) = \begin{cases} N_b, & z < z_b \\ N_b + \frac{z - z_b}{z_t - z_b}(N_t - N_b), & z_b \leq z \leq z_t \\ N_t, & z_t < z. \end{cases} \tag{3.74}$$

The horizontal wavelength is $\lambda_x = 0.5\mathit{\Delta}_z$ with $\mathit{\Delta}_z = z_t - z_b$ and the frequency is $\omega = 0.6N_b$, which results in a vertical wavelength in the bottom layer of $\lambda_{z,b} = 0.375\mathit{\Delta}_z$. We obtain a reference solution by direct numerical integration of equation (3.7) with the data we just mentioned. The numerical scheme we use is the MATLAB built-in integrator ode45, which is based on a fourth-order explicit Runge-Kutta scheme.

To construct the solution with the multi-layer approach, we take the same steps as with computing the transmission coefficient. Let J be the number of jumps, i.e., we

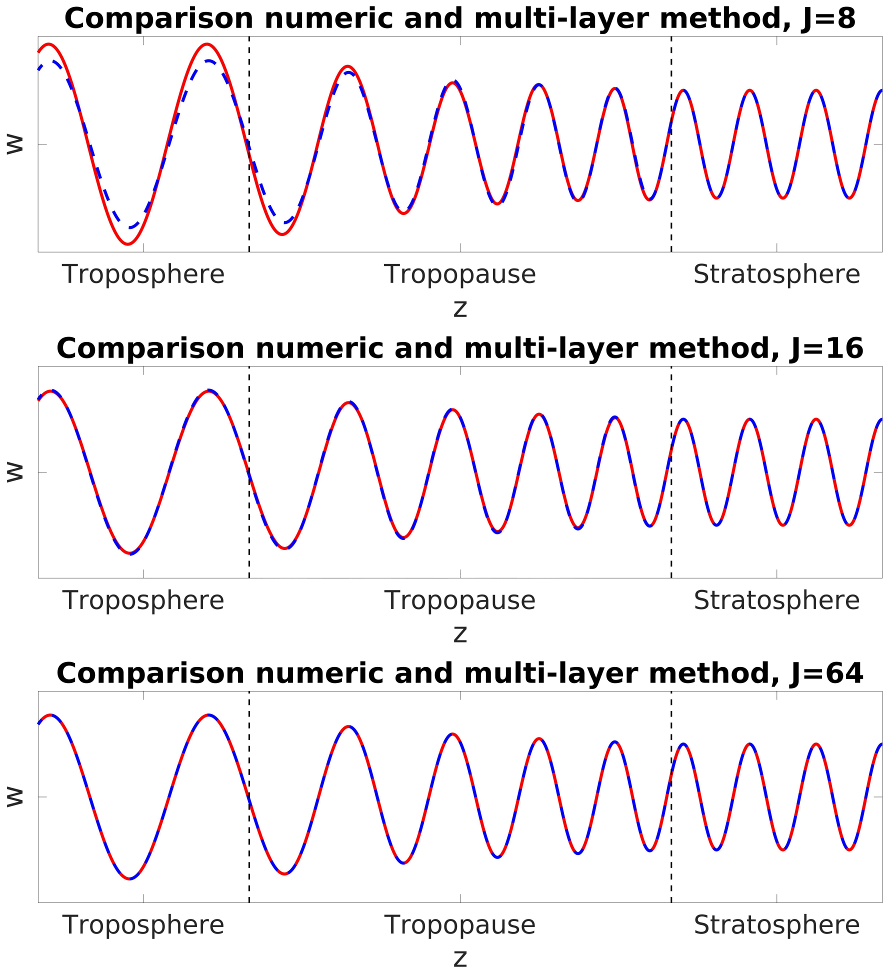

Figure 3.2: Comparison between the numerical solution of equation (3.7) and the solution obtained by using the multi-layer method for the linearly increasing stratification profile (3.97). The solid red curve corresponds to the multi-layer solution, the dashed blue curve to the numeric solution. The vertical dashed black lines indicate the beginning and the end of the tropopause. The boundary conditions for the different methods were chosen in a way that the solutions match across the uppermost (here: rightmost) layer.

have $J+1$ layers of constant stratification. For each layer, the equation to solve is (3.18). We already know that we have plane wave solutions, given by equation (3.19). The amplitudes A_j and B_j can then be computed via the matching conditions (3.24) and given boundary data for A_{J+1} and B_{J+1}. We test the setup again for boundary data with a wave incident from below, represented by A_1 and no downward travelling wave in the uppermost layer, that means $B_{J+1}=0$. Instead of assuming the amplitude of the incident wave, we can as well assume the amplitude of the transmitted wave, which is A_{J+1}. Since the transmission coefficient does not depend on the amplitude, we can choose any non-zero value for A_{J+1}. In order to obtain comparable results, we must translate the boundary conditions we put into the numerical solver into an expression for the multi-layer method. Since the Taylor-Goldstein equation is a second-order equation, it takes boundary conditions of the form $w(z_0)$ and $w'(z_0)$, where z_0 is either the top or the bottom of the integration domain. Here we chose the domain top since we already know that there is only an upward travelling wave. Without loss of generality, we set

$$w(z_0) = 1, \tag{3.75a}$$

$$w'(z_0) = 0. \tag{3.75b}$$

Since the stratification in the uppermost layer is constant, we know that an analytical solution exists and that it is a plane wave. Hence the wave amplitude of the numerical solution equals 1 in this layer, since the point z_0 is a maximum point.

With the use of Euler's formula, we can rewrite the multi-layer solution in the uppermost layer (which coincides with the exact solution):

$$w_{J+1}(z) = \Re(A_{J+1}\exp(im_{J+1}z)) = \Re(A_{J+1})\cos(m_{J+1}z) - \Im(A_{J+1})\sin(m_{J+1}z). \tag{3.76}$$

By using the initial conditions (3.75), we obtain a linear equation system with two equations for the real and imaginary part of A_{J+1}:

$$1 = \Re(A_{J+1})\cos(m_{J+1}z_0) - \Im(A_{J+1})\sin(m_{J+1}z_0), \tag{3.77a}$$

$$0 = -m_{J+1}\Re(A_{J+1})\sin(m_{J+1}z_0) - m_{J+1}\Im(A_{J+1})\cos(m_{J+1}z_0). \tag{3.77b}$$

Solving this system gives us

$$\Re(A_{J+1}) = \cos(m_{J+1}z_0), \tag{3.78a}$$

$$\Im(A_{J+1}) = -\sin(m_{J+1}z_0). \tag{3.78b}$$

These are the boundary conditions for the multi-layer method. It is easy to check that

$$|A_{J+1}| = \sqrt{\Re(A_{J+1})^2 + \Im(A_{J+1})^2} = \sqrt{\cos(m_{J+1}z_0)^2 + \sin(m_{J+1}z_0)^2} = 1, \tag{3.79}$$

which matches the wave amplitude of the numerical solution.

The number of jumps were chosen to be $J = 8, 16$ and 64 for the multi-layer solution. The results can be seen in figure 3.2. Qualitatively, we can say that the multi-layer solution converges to the one obtained by direct numerical integration. By looking at the maximum absolute error

$$\max_z |w_{\mathrm{num}}(z) - w_{ml}(z)| \,, \tag{3.80}$$

we find values $3.29 \cdot 10^{-1}, 2.89 \cdot 10^{-2}$ and $5.81 \cdot 10^{-4}$ for $J = 8, 16, 64$, respectively. A more detailed analysis for different wavelength, frequencies and number of layers yield quadratic decrease of the error, at least for an appropriately large number of layers. This is one order better than what the proof of convergence order in Lara (2004) gives, but as the author there uses the approximate values at a grid point and we use the value in the middle between two points. It is suggested there that this should yield a convergence order of 2.

It is important to note that there are no further restrictions on $m^2(z)$. It can very well be negative, corresponding to real eigenvalues and hence, to exponential growth or decay of the solution. This phenomenon can occur in the atmosphere, when the wave frequency is higher than the background stratification, which leads to wave damping. Such levels are called reflection levels, since waves tend to reflect from them. In fact, ray theory predicts a total reflection of waves from such layers. This is, however, not the total truth due to the restrictions on ray theory. A closer examination of reflection levels follows over the course of this work.

3.5 Limit approach

As we now know that the multi-layer method converges to the real solution, the question arises if it is actually possible to compute the limit for the number of layers tending to infinity. If so, we would have solved equation (3.7), which was not possible with classical methods. Unfortunately, the direct answer to that question is no. Nevertheless, we are able to find an ODE system that develops from the limit procedure and sheds light on the solution structure from a different angle. Moreover, with the multi-layer method converging, there must also be a limit for the transmission coefficient. The ODE we are going to derive can be solved numerically and allows us to compute a transmission coefficient which we can compare to the one we obtain from the multi-layer method to see how accurate it is and what would be a good number of layers to work with in order to guarantee fairly accurate results and low computational cost.

First, we observe that the matrix M_j in equation (3.27) tends to the identity matrix, as $m_j + 1$ tends to m_j for all $j = 1, \ldots, J$, i.e.

$$\lim_{J\to\infty} c_j = 1 = \lim_{J\to\infty} c_j^*, \tag{3.81a}$$

$$\lim_{J\to\infty} d_j = 0 = \lim_{J\to\infty} d_j^*. \tag{3.81b}$$

But similar to the formula $e = \lim_{n\to\infty}(1+1/n)^n$ for the Euler constant, the number of near-identity matrices we multiply tends to infinity, hence the product does not converge to the identity matrix. Moreover, the entries are complex, which poses an additional challenge. Hence, there seems to be no closed formula for

$$\lim_{J\to\infty} \prod_{j=J}^{1} \boldsymbol{M}_j^{(J)}. \tag{3.82}$$

Most methods known for real matrices blow up because of the non-vanishing imaginary part. This would have given at least a solution to the transmission coefficient problem.

The idea is to reformulate the limit process as a differential equation for a vector consisting of the amplitudes for the upward and downward propagating wave. We know that the depth of each layer is $h = \Delta_z/J$, so the limit process $J \to \infty$ can also be seen as $\Delta_z/J \to 0$ or $h \to 0$. Moreover, the j-indexed variables A_j, B_j, m_j are approximations of their continuous counterparts at $z_j + h/2$. By using the recurrence relation (3.24) we can write

$$\begin{pmatrix} A_{j+1} \\ B_{j+1} \end{pmatrix} - \begin{pmatrix} A_j \\ B_j \end{pmatrix} = \left(\boldsymbol{M}_j^{(J)} - I\right) \begin{pmatrix} A_j \\ B_j \end{pmatrix}, \tag{3.83}$$

where I is the 2-by-2-identity matrix. Dividing now by h and taking the limit $h \to 0$, the left-hand side converges to the z-derivative of the amplitudes. Using the short-hand notation $\underline{\boldsymbol{A}}= \underline{\boldsymbol{A}}(z) = (A(z), B(z))^T$ for the vector of amplitudes[4], we have

$$\frac{\mathrm{d}\underline{\boldsymbol{A}}}{\mathrm{d}z} = \lim_{h\to 0} \frac{\left(\boldsymbol{M}_j^{(J)} - I\right)}{h} \underline{\boldsymbol{A}}. \tag{3.84}$$

This is now a differential equation for the amplitudes in $\underline{\boldsymbol{A}}$. If we want to have any chance of solving it (either analytically or numerically), we have to execute the limit process

$$\lim_{h\to 0} \frac{\left(\boldsymbol{M}_j^{(J)} - I\right)}{h}. \tag{3.85}$$

This is done component-wise. The upper-left entry of the matrix inside the limit in

---

[4] Here, the superscript T denotes the transpose.

(3.85) is $(c_j - 1)/h$. We can rewrite $c_j - 1$ as

$$\begin{aligned}
&c_j - 1 \\
&= \left(\frac{m(z_j) + m(z_j + h)}{2m(z_j + h)}\right) \exp\left(i(m(z_j) - m(z_j + h))z_j\right) - 1 \\
&= \left(\frac{m(z_j) + m(z_j) + hm'(z_j) + o(h)}{2(m(z_j) + hm'(z_j) + o(h))}\right) \exp(i(m(z_j) - m(z_j) - hm'(z_j) + o(h))z_j) - 1 \\
&= \left(\frac{2m(z_j) + hm'(z_j) + o(h)}{2(m(z_j) + hm'(z_j) + o(h))}\right) \exp(-i(hm'(z_j) + o(h))z_j) - 1 \\
&= \left(\frac{2m(z_j) + hm'(z_j) + o(h)}{2(m(z_j) + hm'(z_j) + o(h))}\right) \big(1 - ihm'(z_j)z_j + o(h)\big) - 1 \\
&= \frac{2m(z_j) + h(m'(z_j) - 2im(z_j)m'(z_j)z_j) + o(h)}{2(m(z_j) + hm'(z_j) + o(h))} - 1 \\
&= \frac{h(-m'(z_j) - 2im(z_j)m'(z_j)z_j) + o(h)}{2(m(z_j) + hm'(z_j) + o(h))}
\end{aligned} \tag{3.86}$$

Dividing equation (3.86) by h and letting $h \to 0$, we obtain

$$f(z) := \lim_{h \to 0} \frac{c_j - 1}{h} = -\frac{m'(z)}{2m(z)} - im'(z)z. \tag{3.87}$$

With a similar computation, we rewrite d_j as

$$\begin{aligned}
&d_j \\
&= -\left(\frac{m(z_j) - m(z_j + h)}{2m(z_j + h)}\right) \exp\left(-i(m(z_j) + m(z_j + h))z_j\right) \\
&= -\left(\frac{m(z_j) - m(z_j) - hm'(z_j) + o(h)}{2(m(z_j) + hm'(z_j) + o(h))}\right) \exp(-i(2m(z_j) + h(m'(z_j) + o(h))z_j) \\
&= -\left(\frac{-hm'(z_j) + o(h)}{2(m(z_j) + hm'(z_j) + o(h))}\right) \exp(-i(2m(z_j) + h(m'(z_j) + o(h))z_j)
\end{aligned} \tag{3.88}$$

Hence, we obtain

$$g(z) := \lim_{h \to 0} \frac{d_j}{h} = \frac{m'(z)}{2m(z)} \exp(-2im(z)z). \tag{3.89}$$

The respective limits for the starred entries yield the same except for a replacement of

i by $-i$ or vice versa. Hence the differential equation for the amplitudes is

$$\frac{\mathrm{d}\underline{\boldsymbol{A}}}{\mathrm{d}z} = \underbrace{\begin{pmatrix} f(z) & g(z) \\ g^*(z) & f^*(z) \end{pmatrix}}_{=:\mathcal{M}(z)} \underline{\boldsymbol{A}}. \tag{3.90}$$

One has to be careful about the use of m'. Since we only requested a continuous function for N, it is not guaranteed that it is also differentiable, especially at the interfaces to the troposphere and stratosphere (see for example the linearly increasing profile (3.74) form th previous section). This should, however, not be a problem, if we additionally assume piecewise differentiability, i.e. the set of values where N is not differentiable should be finite. Then, we can solve equation (3.90) piecewise, using the solutions from one patch as boundary conditions for the next one.

Equation (3.90) can only be solved analytically if $\mathcal{M}(z_1)\mathcal{M}(z_2) = \mathcal{M}(z_2)\mathcal{M}(z_1)$ holds for all z_1, z_2 in the integration domain. Unfortunately, this is in general not true for arbitrary stratification profiles. Consider for example the upper left entry of $\mathcal{M}(z_2)\mathcal{M}(z_1)$ and $\mathcal{M}(z_2)\mathcal{M}(z_1)$:

$$(\mathcal{M}(z_1)\mathcal{M}(z_2))_{1,1} = f(z_1)f(z_2) + g(z_1)g^*(z_2), \tag{3.91}$$

$$(\mathcal{M}(z_2)\mathcal{M}(z_1))_{1,1} = f(z_2)f(z_1) + g(z_2)g^*(z_1). \tag{3.92}$$

We can clearly assume commutativity for the separate products. In order for the matrix entries to coincide, the equation $g(z_1)g^*(z_2) = g(z_2)g^*(z_1)$ needs to hold. Inserting the definition of g from equation (3.89), this reduces to the statement that either the exponents of the exp-function need to be the same or $m' = 0$. If $m' = 0$, then, every entry of $\mathcal{M}$ is zero and hence the amplitudes do not change with height. This happens if and only if N is constant, in which case we don't expect any change in the wave amplitudes. If $m' \neq 0$, basic algebra reveals that the following equation needs to hold for any z_1, z_2 in the integration domain:

$$m(z_1)z_1 = m(z_2)z_2. \tag{3.93}$$

In particular, the vertical wavenumber is inversely proportional to the height. It is easy to see that this is in general not true.

What we can deduce, however, is that if the functions f and g are analytic over the interval $[z_b, z_t]$, equation (3.90) has a unique analytic solution for arbitrary initial data $\underline{\boldsymbol{A}}(z_0) = \underline{\boldsymbol{A}}_0$, $z_0 \in [z_b, z_t]$ (see, for example, Teschl (2012) for the theory on complex ODEs). It is easy to check that this is the case for stratification profiles and wave parameters such that there is no reflection layer, i.e. a point z_r where $N(z_r) = \omega$. Although securing the existence of solutions, finding analytic or even explicit expressions for them will be a nearly hopeless undertaking. Another approach to find at least approximate solutions are power series methods. Since analytic functions on an open subset coincide locally with a convergent power series (see , e.g., Stalker (1998) for details), we can make a power series ansatz for the solution of equation (3.90). In order to do so, we extend $[z_b, z_t]$ to an open subset of the complex numbers, in which $\mathcal{M}$ is still analytic. But although the matrix has no singularities for real values, it has some for certain complex numbers, which drastically restricts the radius of convergence of the power series solution to a value that is not guaranteed to be large enough to cover the whole region of interest. However, it would be possible to partition the interval into smaller segments and finding the power series solution in each segment, but this procedure is very tedious and still only yields a solution up to a certain precision. We will see in the upcoming error analyses that the multi-layer method yields very accurate results notwithstanding that it is a much easier-to-apply technique. Hence, the evaluation of equation (3.90) will be done numerically.

The question may arise which benefit integrating equation (3.90) has over integrating (3.7), since both equations are equivalent, using appropriate boundary conditions. The advantage is that equation (3.90) separates between upward and downward propagating waves, knowing at any point which part of the waves belong to either of those two parts, while by straight up integrating the Taylor-Goldstein equation, we can not tell this by just looking at the solution[5].

Another challenge are reflection levels, i.e. a point z_r such that $N(z_r) = \omega$. Then, the entries of the coefficient matrix $\mathcal{M}$ tend to infinity, because $m(z_r) = 0$. By regarding equation (3.90) as a system of complex differential equations, the point z_r is an isolated singularity. At first sight, it might seem that the singularity is a first order pole, since functions of the form a'/a, where a has a zero of any order at some point z_0 do have a first order pole at z_0. Assuming a is continuous, we can find an open set around z_0 in which a does not contain any poles or other zeroes. In this open set, we can write a as

$$a(z) = (z - z_0)^\alpha b(z), g(z_0) \neq 0. \tag{3.94}$$

Here, α denotes the order of the zero. Then, we have for the derivative of a:

$$a'(z) = \alpha(z - z_0)^{\alpha-1} b(z) + (z - z_0)^\alpha b'(z), \tag{3.95}$$

and hence

$$\frac{a'}{a} = \alpha(z - z_0)^{-1} + \frac{b'(z)}{b(z)} \tag{3.96}$$

As $b(z_0) \neq 0$ and b does not contain any poles, a/a' has a first order pole at z_0.

Unfortunately, the extra terms that are prevalent in the coefficients, i.e. $im'(z)z$ and

---

[5] Both solutions we obtain from a direct numerical simulation are steady-state solutions, i.e. the solution does not change in time, hence we cannot see movement of the wave, but that does not mean that it is not there

$\exp(-2im(z)z)$ involve square roots of z, which results in f and g not being holomorphic in a punctured disk around z_r. The reason for this is that the complex square root has two branches, similar to real numbers where each positive real number x has two possibilities for its root: $\sqrt{x}$ and $-\sqrt{x}$, with 0 having only one root. Extended to the complex numbers, every complex number unequal to 0 has 2 possibilities for its square root. Similar to the real square root function, a principal square root is defined. This definition then results in a function that assigns each complex number exactly one of its square roots. It is holomorphic everywhere except for the non-negative real numbers, on the negative real numbers, it is even discontinuous. Via coordinate transformation, this discontinuity can occur across any ray in the complex plane, but the square root will always be only holomorphic in a disk with this particular ray removed. Therefore, known theorems about existence and structure of solutions, which apply only for functions holomorphic on a punctured disc, can not be used here. Nonetheless, the structure of the functions in equation (3.90) are very interesting and could serve as a topic for future research.

Existing research in this case, such as Sutherland and Yewchuck (2004), who investigate propagation of gravity waves through a layer of sudden reduced or vanishing stratification, suggest some sort of "wave tunnelling" (a term coined by the comparison to quantum tunnelling of electrons in quantum physics) through this region, dependent on the wavelength of the incident wave. As we will see later, the findings from our multi-layer method confirm those results also for continuous transitions to a lower value of the Brunt-Väisälä frequency. Apart from that, an intensive investigation of the behaviour of gravity waves near reflection layers requires a scale analysis for different regimes of vertical wavelengths. This will be discussed briefly in subsection 3.6.2 and again in chapter 7.

3.6 Results for various stratification profiles

This subsection is meant to show some exemplary results for plane wave transmission we computed with the multi-layer method. We chose four different stratification profiles to show here. The first one is a linear increase between two different values. This serves as an introductory example to show how the multi-layer method is used to compute transmission coefficients. The second profile we are going to show contains a region of weak stratification, which in turn leads to wave tunnelling or reflection. A basic variant of this phenomenon was also studied by Sutherland and Yewchuck (2004). With this example, we want to show that the multi-layer method is able to support wave tunnelling. For the third example, we construct a profile that is leaned on the findings of Birner (2006) and should represent the stratification a realistic tropopause with a strong temperature inversion layer. The last profile consists of two stratification peaks, separated by a region of uniform stratification. With this, we investigate the influence of the separation distance d between the two peaks. All profiles share a common structure, namely that we have a region of non-constant stratification of depth Δ_z that has a region of constant stratification with value N_b below and with value N_t above it. This is about what we can observe in the atmosphere: The stratification changes rapidly in the tropopause and is nearly constant in the free troposphere and the stratosphere.

We will focus on a frequency range from 0 to N_b, since waves with frequencies larger than N_b are evanescent. We opted to use a grid size of 300 horizontal wavelengths, logarithmically spaced between 1000 m and 100000 m, which corresponds to values from Δ_z to $100\Delta_z$, and 300 frequencies, equally spaced between $0.001N_0$ and $0.999N_0$. This results in a total of 90000 grid points. The number of layers equals 128. The computations are performed on the author's office computer with a standard Intel® Core™ i7-3770 CPU and 8 GB RAM. The software we use is MATLAB. The computation times lie within a range of 70 to 80 seconds when computed on a single core. Compared to the numerical method of Nault and Sutherland (2007), who need about 1 day to simulate 300 × 300 parameters on a "typical desktop computer" at that time, this is a decrease in computation time by a factor of about 1000. Even when considering the slightly higher clock rate and RAM, the multi-layer method is much more efficient in computing Transmission coefficients for large data sets.

3.6.1 Linear increase

The first case for which we will present results is the case of the linearly increasing stratification, defined as

$$N(z) = \begin{cases} N_b, & z < z_b \\ N_b + \frac{z-z_b}{z_t-z_b}(N_t - N_b), & z_b \leq z \leq z_t \\ N_t, & z_t < z. \end{cases} \tag{3.97}$$

The results are presented in a dimensionless way in order to be as general as possible. For reference, the computations were done with realistic atmospheric values: $\Delta_z = 1000\,\mathrm{m}$ and $N_b = 0.01\,\mathrm{s}^{-1}$.

Figure 3.3 gives overview over the transmission coefficients for the linear increasing profile (3.97). We want to point out three regimes of vertical wavelengths: shorter than Δ_z, comparable to Δ_z and longer than Δ_z, represented by the three curves in figure 3.3. Δ_z in turn represents the scale of variation of N. So wavelength that are much shorter than Δ_z are also small compared to the scale of variation of N. This is the regime where the classical WKB theory is applicable. Ray theory, that is based on WKB assumptions, predicts perfect transmission for those waves in a linearly increasing profile and this is exactly what we are able to find. Even for moderately large horizontal and vertical wavelengths, the transmission is high, at least up to a certain point. As we can see, there is stronger reflection when we are moving to the right and to the bottom

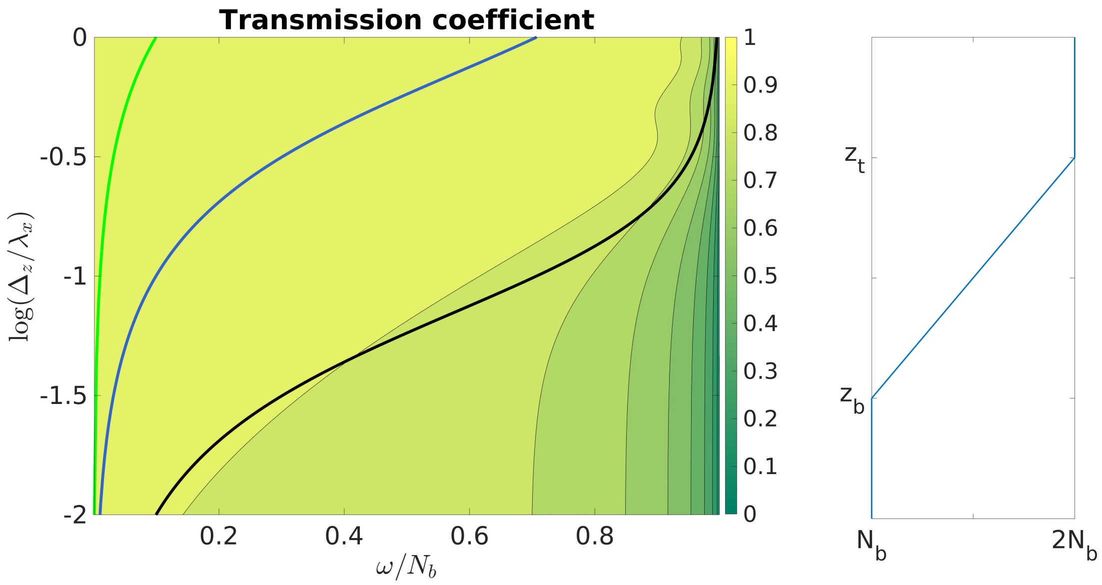

Figure 3.3: Transmission coefficients for a stratification profile that increases linearly over a finite region of depth $\mathit{\Delta}_z$. The three curves represent constant vertical wavelength in the bottom layer: green for $\lambda_z = 0.1\mathit{\Delta}_z$, blue for $\lambda_z = \mathit{\Delta}_z$ and black for $\lambda_z = 10\mathit{\Delta}_z$.

in the panel, that means that the wave frequency gets closer to the lower value N_b and the horizontal wavelength (and eventually the vertical wavelength) is growing. If the vertical wavelength exceeds $\mathit{\Delta}_z$ by about an order of magnitude (black curve), waves start to transmit worse.

Waves that have frequencies close to the Brunt-Väisälä frequency are almost purely horizontal and in the limit of $\omega \to N_b$ for fixed λ_x, it seems from figure 3.3 that the transmission eventually gets zero. This seems reasonable, since there is no vertical wave structure and hence no vertical energy transport. The upcoming computation gives a proof for this claim. Let us have a look at

$$\lim_{\omega \to N_b} m_j = \lim_{\omega \to N_b} -k\sqrt{\frac{N_j^2}{\omega^2} - 1} = -k\sqrt{\frac{N_j^2}{N_b^2} - 1} =: \tilde{m}_j, \tag{3.98}$$

If $j \neq 1$, then $N_j \neq N_b$ (remember: linear increasing profile). Hence, $\tilde{m}_j \neq 0$. Since $\det \boldsymbol{M}_j = m_j/m_{j+1}$, $\boldsymbol{M}_j$ is regular for $J \neq 1$. For $j = 1$, $N_1 = N_b$, hence $\tilde{m}_1 = 0$ and therefore, by the definition of the transmission coefficient (3.61), the transmission is also 0, as $M_{2,2} \neq 0$. In the limit $\lambda_x \to \infty$ (or equivalently $k \to 0$) for fixed $\omega < N_b$, it is possible to find a closed formula for the matrix product in (3.56) and hence a formula for the amplitude ratio, which coincides with the classical result for a two-layer model

(Eliassen and Palm, 1961). We write

$$m_j = k\sqrt{\frac{N_j^2}{\omega^2} - 1} = k\hat{m}_j \tag{3.99}$$

and consider the matrix entries (3.28) in the limit $k \to 0$:

$$\begin{aligned}\tilde{c}_j := \lim_{k\to 0} c_j &= \lim_{k\to 0} \frac{1}{2}\left(\frac{m_j}{m_{j+1}} + 1\right) \exp\left(i\left(m_j - m_{j+1} z_j\right)\right) \\ &= \lim_{k\to 0} \frac{1}{2}\left(\frac{k\hat{m}_j}{k\hat{m}_{j+1}} + 1\right) \exp\left(ik\left(\hat{m}_j - \hat{m}_{j+1} z_j\right)\right) \\ &= \frac{1}{2}\left(\frac{\hat{m}_j}{\hat{m}_{j+1}} + 1\right)\end{aligned} \tag{3.100}$$

In a similar fashion, we follow that

$$\tilde{d}_j := \lim_{k\to 0} d_j = \frac{1}{2}\left(\frac{\hat{m}_j}{\hat{m}_{j+1}} - 1\right). \tag{3.101}$$

Moreover, $\tilde{c}_j^* = \tilde{c}_j$ and $\tilde{d}_j^* = \tilde{d}_j$, as the exponential terms vanish in the limit process. The matrices

$$\widetilde{\boldsymbol{M}}_j := \lim_{k\to 0} \boldsymbol{M}_j = \begin{pmatrix} \tilde{c}_j & \tilde{d}_j \\ \tilde{d}_j & \tilde{c}_j \end{pmatrix} \tag{3.102}$$

are bisymmetric (symmetric to both main diagonals).

Claim 3.6.1. *The set* $\left\{\begin{pmatrix} a & b \\ b & a \end{pmatrix} \mid a, b \in \mathbb{C}\right\}$ *is closed under the usual matrix multiplication*[6].

Proof. Let $M_1 = \begin{pmatrix} a & b \\ b & a \end{pmatrix}, M_2 \begin{pmatrix} c & d \\ d & c \end{pmatrix}$ be two bisymmetric matrices with entries in $\mathbb{C}$. Then

$$M_1 M_2 = \begin{pmatrix} ac + bd & ad + bc \\ bc + ad & bd + ac \end{pmatrix}. \tag{3.103}$$

As addition in $\mathbb{C}$ is commutative, $M_1 M_2$ is again bisymmetric. $\square$

---

[6] In fact, this even forms an abelian, but we only need the closedness for our purposes.

Let us have a closer look at $\widetilde{\boldsymbol{M}}_j\widetilde{\boldsymbol{M}}_{j-1}$. The diagonal entries are

$$\begin{aligned}\tilde{c}_j\tilde{c}_{j-1}+\tilde{d}_j\tilde{d}_{j-1} &= \frac{1}{4}\left(\frac{\hat{m}_j}{\hat{m}_{j+1}}+1\right)\left(\frac{\hat{m}_{j-1}}{\hat{m}_j}+1\right)+\frac{1}{4}\left(\frac{\hat{m}_j}{\hat{m}_{j+1}}-1\right)\left(\frac{\hat{m}_{j-1}}{\hat{m}_j}-1\right)\\ &= \frac{1}{4}\left(\frac{\hat{m}_{j-1}}{\hat{m}_{j+1}}+\frac{\hat{m}_j}{\hat{m}_{j+1}}+\frac{\hat{m}_{j-1}}{\hat{m}_j}+1+\frac{\hat{m}_{j-1}}{\hat{m}_{j+1}}-\frac{\hat{m}_j}{\hat{m}_{j+1}}-\frac{\hat{m}_{j-1}}{\hat{m}_j}+1\right)\\ &= \frac{1}{2}\left(\frac{\hat{m}_{j-1}}{\hat{m}_{j+1}}+1\right).\end{aligned} \tag{3.104}$$

These are very similar to the entries of $\widetilde{\boldsymbol{M}}_j$, but with $\hat{m}_j$ replaced by $\hat{m}_{j-1}$. For the off-diagonal entries, we have

$$\begin{aligned}\tilde{c}_j\tilde{d}_{j-1}+\tilde{d}_j\tilde{c}_{j-1} &= \frac{1}{4}\left(\frac{\hat{m}_j}{\hat{m}_{j+1}}+1\right)\left(\frac{\hat{m}_{j-1}}{\hat{m}_j}-1\right)+\frac{1}{4}\left(\frac{\hat{m}_j}{\hat{m}_{j+1}}-1\right)\left(\frac{\hat{m}_{j-1}}{\hat{m}_j}+1\right)\\ &= \frac{1}{4}\left(\frac{\hat{m}_{j-1}}{\hat{m}_{j+1}}-\frac{\hat{m}_j}{\hat{m}_{j+1}}+\frac{\hat{m}_{j-1}}{\hat{m}_j}-1+\frac{\hat{m}_{j-1}}{\hat{m}_{j+1}}+\frac{\hat{m}_j}{\hat{m}_{j+1}}-\frac{\hat{m}_{j-1}}{\hat{m}_j}-1\right)\\ &= \frac{1}{2}\left(\frac{\hat{m}_{j-1}}{\hat{m}_{j+1}}-1\right).\end{aligned} \tag{3.105}$$

A simple induction argument shows that the entries of

$$\widetilde{\boldsymbol{M}}=\begin{pmatrix}\tilde{c} & \tilde{d}\\ \tilde{d} & \tilde{c}\end{pmatrix}:=\prod_{j=J}^{1}\widetilde{\boldsymbol{M}}_j \tag{3.106}$$

are

$$\tilde{c}=\frac{1}{2}\left(\frac{\hat{m}_1}{\hat{m}_{J+1}}+1\right), \tag{3.107}$$

$$\tilde{d}=\frac{1}{2}\left(\frac{\hat{m}_1}{\hat{m}_{J+1}}-1\right). \tag{3.108}$$

The relation between the amplitudes is the same as in (3.59), i.e.

$$\frac{A_{J+1}}{A_1}=\frac{\det(\widetilde{\boldsymbol{M}})}{\tilde{d}}=\frac{m_1}{m_{J+1}}\left(\frac{1}{2}\left(\frac{\hat{m}_1+\hat{m}_{J+1}}{\hat{m}_{J+1}}\right)\right)^{-1}=\frac{2\hat{m}_1}{\hat{m}_1+\hat{m}_{J+1}}. \tag{3.109}$$

This is the result for internal waves in a two-layer fluid (Eliassen and Palm, 1961). It is interesting to see that we made no assumptions on the structure of N, hence this limit holds for any stratification profile.

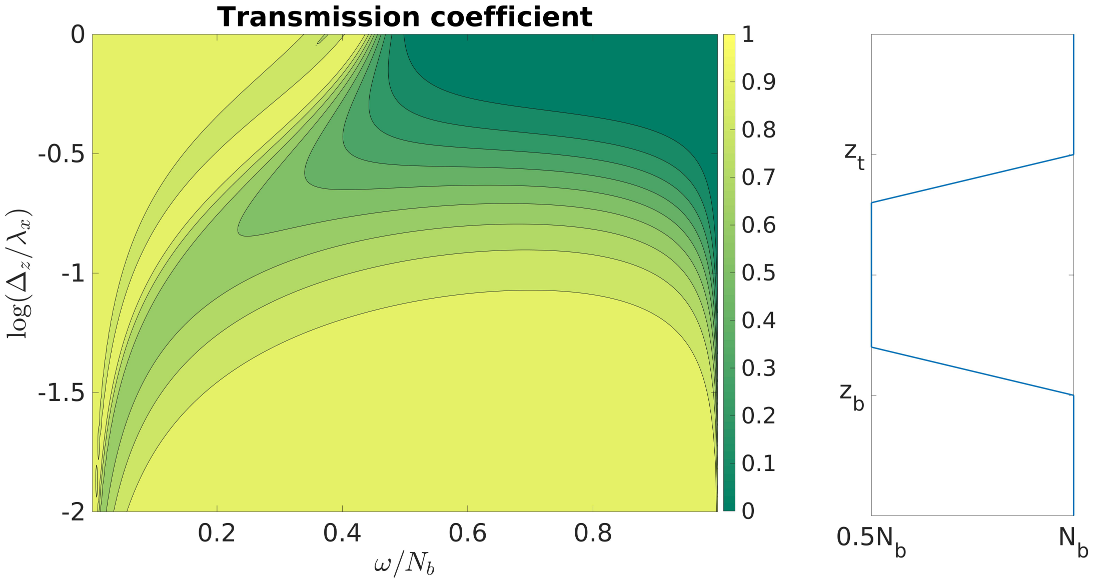

Figure 3.4: Transmission coefficients for a profile that has a region of decreased stratification. We see that waves, whose frequency is larger than $0.5N_b$ can transmit, if their wavelength is long compared to the region of decreased stratification.

3.6.2 Wave tunneling

We consider now a case where the stratification linearly drops from some N_b to a value $N_d < N_b$ over a finite region and eventually increases again back to N_b:

$$N(z) = \begin{cases} N_b, & z < z_b \\ N_b + \frac{z-z_b}{z_{d_1}-z_b}(N_d - N_b), & z_b < z \leq z_{d_1} \\ N_d, & z_{d_1} \leq z \leq z_{d_2} \\ N_d + \frac{z-z_{d_2}}{z_t-z_{d_2}}(N_b - N_d), & z_{d_2} < z \leq z_t \\ N_b, & z_t < z. \end{cases} \tag{3.110}$$

In the example we present, $z_{d_1} - z_b = 0.2\Delta_z = z_t - z_{d_2}$ and $N_d = 0.5N_b$. The results found for this case are very different from what ray theory tells us. There, it is predicted that waves totally reflect from a layer, where $\omega \geq N$. However, when there is only a small, finite region where $\omega \geq N$ holds, wave propagation through this region is possible under certain conditions. Sutherland and Yewchuck (2004) described this phenomenon for a sharp drop to a weak or even vanishing stratification, and our results show that tunnelling also exists in the case of a continuous transition. In figure 3.4, one can see

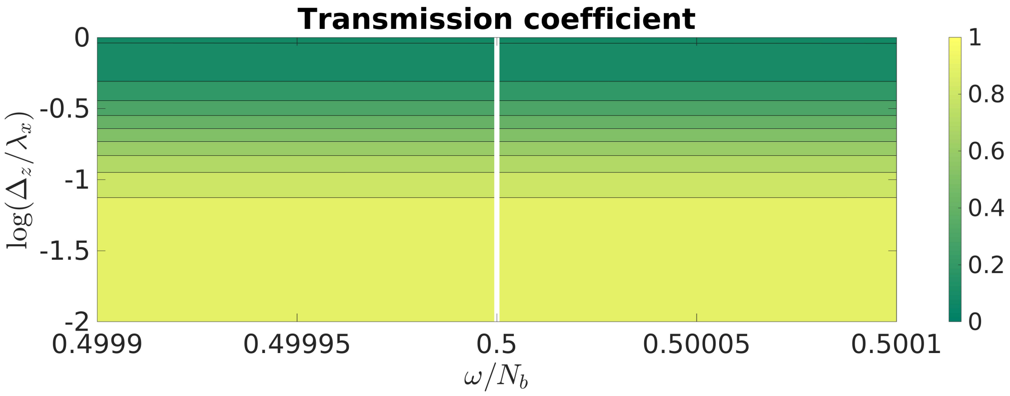

Figure 3.5: Zoom into the left panel of figure 3.4 centred around $\omega = 0.5N_b$.

the transmission coefficient for profile (3.110). In this particular example, ray theory predicts that every wave with frequency $\omega \geq 0.5N_b$ would fully reflect from this layer, but we can observe that if the wavelength is large compared to the extent of the region with weak stratification, it is possible to obtain high wave transmission. In fact, the longer the waves seem to be, the better they transmit. This can be easily derived from the two-layer limit (3.109). As $m_b = m_t$ in this example, the amplitude ratio in the limit of long waves is 1.

As we said earlier, the multi-layer method would fail for this profile if we would try to evaluate it for $\omega = 0.5N_b$, since there is an interval, in which this equation holds. But the panel in figure 3.4 suggests continuity in the transmission coefficient over the whole frequency range. Figure 3.5 shows a zoom into the area around $\omega = 0.5N_b$ and corroborates our suggestion. We see the domain from $0.4999N_b$ to $0.5001N_b$. The white strip at $0.5N_b$ occurs since the method does not find a value for the TC there, but nonetheless, the panel suggests that the transmission coefficient is continuously extendable over $\omega = 0.5N_b$. This is, however, challenging to prove as a closed formula for the transmission coefficient is hard to write down.

3.6.3 Realistic tropopause profile

Since we are ultimately interested in the behaviour of atmospheric gravity waves and their interaction with the tropopause, we now want to consider a realistic tropopause profile. The stratification is constant with a value N_b below the tropopause. At the temperature inversion layer, the Brunt-Väisälä frequency has a very sharp increase to a peak value N_p, almost like a jump, followed by a relaxation to a value N_t with $N_b < N_t < N_p$ that is the constant value of the stratification in the stratosphere (see Gisinger et al. (2017) for more details on mid-latitude tropopause shapes). We realise this by a piecewise-defined

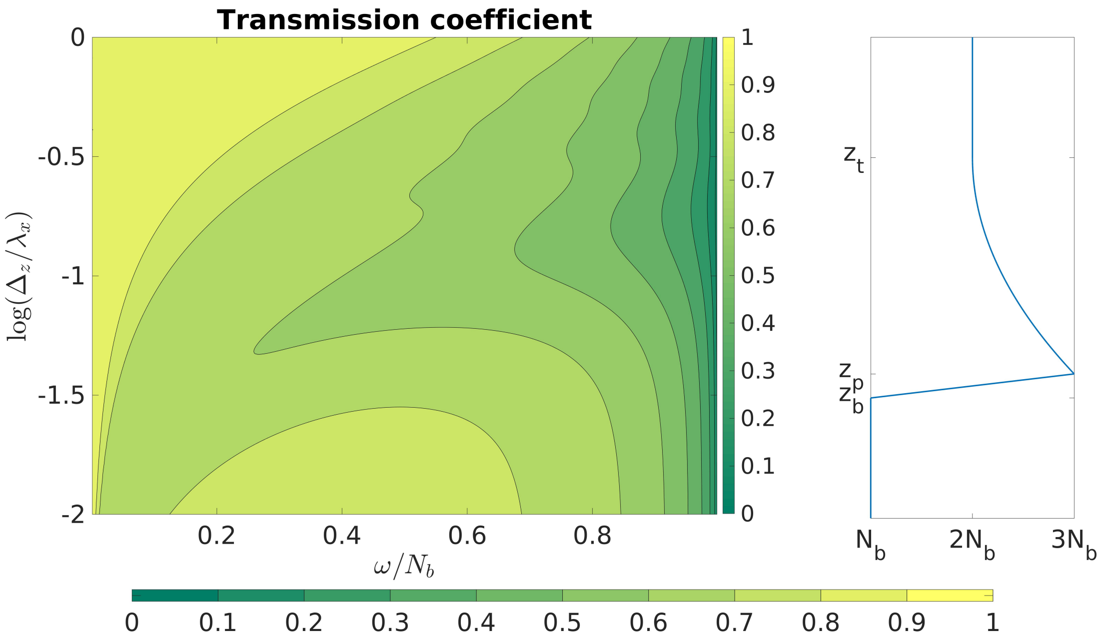

Figure 3.6: Transmission coefficients for a realistic tropopause profile that can be seen in the right panel. In the limit for long waves, the transmission coefficient approaches again the two-layer solution. For moderately long waves, we can see a combination of 2 effects: The sharp increase, which is almost like a jump and blocks a part of the waves and the smooth relaxation afterwards that has high transmission. We also observe that in the classical WKB regime, the transmission is still very high

continuous function:

$$N(z) = \begin{cases} N_b, & z < z_b \\ N_b + \frac{z-z_b}{z_p-z_b}(N_p - N_b), & z_b < z \leq z_p \\ az^2 + bz + c, & z_p < z \leq z_t \\ N_t, & z_t < z, \end{cases} \tag{3.111}$$

where we set $a = N_p - N_t/(z_p - z_t)^2, b = -2z_t(N_p - N_t)/(z_p - z_t)^2$ and $c = N_t + z_t^2(N_p - N_t)/(z_p - z_t)^2$. The values were chosen such that the profile is continuous at z_p and z_t and differentiable at z_t. In the example we show here, we chose $z_p - z_t = 0.1\Delta_z$, $N_p = 3N_b$ and $N_t = 2N_b$. The profile as well as results for the transmission coefficient can be seen in figure 3.6. It is no surprise to see overall lower values of the transmission coefficient. The linear increase now happens over a much smaller vertical extent than in subsection 3.6.1, so that waves with wavelength

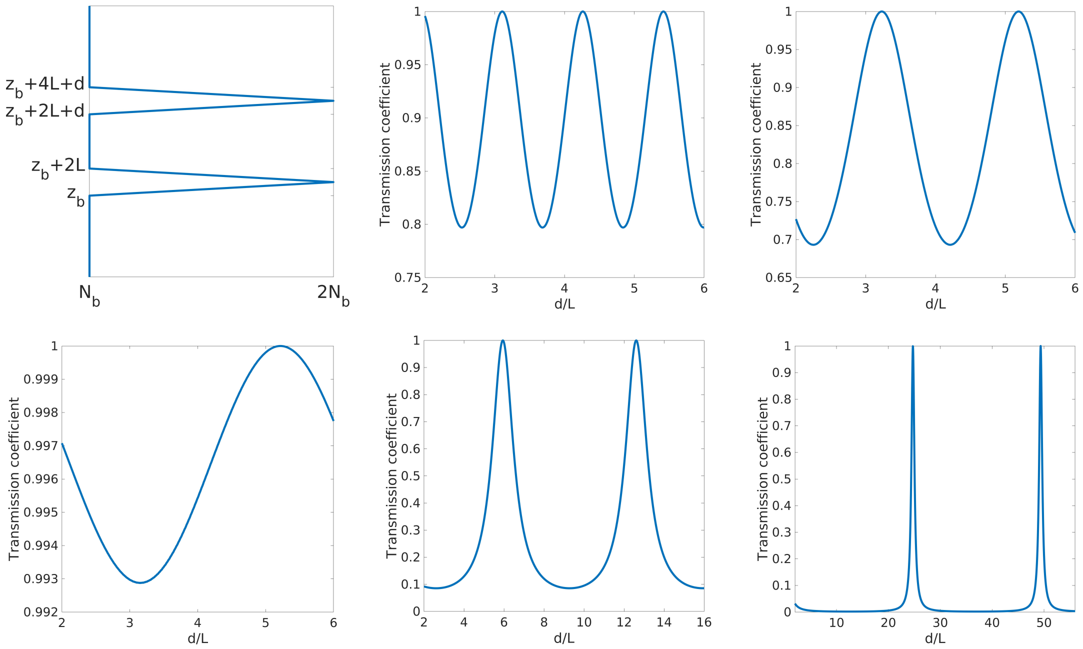

Figure 3.7: Transmission coefficients for the twin peaks profile (seen in the upper left panel) and several wavelength-frequency pairs.

comparable to $\varDelta_z$ are now long compared to $z_p - z_t$. They already partially reflect before reaching the second part of the profile where the stratification slowly weakens.

For the limits $\omega \to N_b$ for fixed λ_x and $\lambda_x \to \infty$ for fixed ω, we have the exact same behaviour as in the linearly increasing case, which is no surprise, since in the first limit, we still have no vertical energy flux and in the second limit we again approach the two-layer model. The rest of the picture however gives some interesting insights. By making the sharp increase asymptotically thin, i.e., making it a (discontinuous) jump, we obtain, for wavelengths comparable to $\varDelta_z$, a composition of the transmission coefficient for a two-layer model (that describes the jump) and the one for the smooth profile that follows after the jump.

3.6.4 Twin peaks

In this subsection, we describe the effect that two areas of non-uniform stratification, separated by an area of uniform stratification, have on plane wave propagation. To do this, we have a look at a stratification profile that has two separated peaks and is hence called twin peaks. One individual peak has a linear increase of the buoyancy frequency from a base value N_b to twice its base value over a finite vertical extent L followed by a linear decrease back to the base value over the same vertical range. Both peaks are separated by a vertical distance d. Mathematically, this is

$$N(z) = \begin{cases} N_b, & z < z_b \\ N_b + \frac{z-z_b}{L} N_b, & z_b \le z < z_b + L \\ 2N_b - \frac{z-z_b-L}{L} N_b, & z_b + L \le z < z_b + 2L \\ N_b, & z_b + 2L \le z < z_b + 2L + d \\ N_b + \frac{z-z_b-2L-d}{L} N_b, & z_b + 2L + d \le z < z_b + 3L + d \\ 2N_b - \frac{z-z_b-3L-d}{L} N_b, & z_b + 3L + d \le z < z_b + 4L + d \\ N_b, & z_b + 4L + d \le z \end{cases} \tag{3.112}$$

A plot of this profile can be seen in the upper left panel of figure 3.7. The other panels show the transmission coefficient for several wavelength-frequency pairs, plotted over d. In all presented cases, we set $L = 500\,\mathrm{m}$. In the upper middle and right panel, we have a horizontal wave length $\lambda_x = 2000\,\mathrm{m}$ and wave frequencies $\omega = 0.5N_b$ and $\omega = 0.7N_b$ respectively. The corresponding vertical wavelengths are $\lambda_z = 1155\,\mathrm{m}$ and $\lambda_z = 1960\,\mathrm{m}$. We observe are sinusodial dependence of the transmission coefficient on d and moderate variations in the values. Absolute difference between minimum and maximum transmission is 0.203 for $\omega = 0.5N_b$ and 0.307 for $\omega = 0.7N_b$. Moreover, the period increases from the upper middle to the upper right panel. In the lower right panel, we have the same horizontal wave length, but a frequency $\omega = 0.9N_b$, resulting in a vertical wavelength of $\lambda_z = 4130\,\mathrm{m}$. We observe that the fluctuations have an even larger period and a much smaller amplitude. We conclude that the period depends on the vertical wavelength. This seems meaningful. Waves that are (partially) reflected at the second peak travel downwards and are incident on the first peak from above, where again a part of the wave is reflected. If this reflected part is in phase with the wave that is transmitted through the first peak, the amplitude is amplified, which leads to the transmission peaks. On the other hand, when the reflected wave is out of phase by 180 degree, the wave amplitude is lowered and the total transmission is worse. This can be seen even more extremely in the lower middle and right panel. Here, the horizontal wavelength is $\lambda_x = 5000\,\mathrm{m}$ and we have wave frequencies $\omega = 0.8N_b$ and $\omega = 0.98N_b$ respectively. The amplitude of the transmission coefficient is very large, especially in the lower right panel, where it spans from almost no to almost total transmission. For this case, we have most of the time a total reflection except for some leaky modes, where the transmission can get almost perfect.

3.7 Convergence study

This subsection is dedicated to the numerical integration of equation (3.90) and the comparison of the transmission coefficients derived from it compared to the transmission coefficients derived from the multi-layer method. As we already know that the multi-layer method converges to the real solution and that equation (3.90) is a reformulation of equation (3.7), we expect a convergence of the values from the multi-layer method towards the limit solution.

In order to do integrate euqation (3.90), proper boundary conditions are needed. Since we are interested in waves that are initially travelling upwards and encountering a non-uniform stratification over a confined region and eventually reaching a region of uniform stratification again, we require that there is only a wave incident on the non-uniform region from below. Hence, above this region, there is no wave that is travelling downwards. Moreover, we are only interested in ratios between the incident and the transmitted wave. Therefore we are free to choose the value of the incident or the transmitted wave, since the equation is linear. To be more precise, if z_e is the upper boundary of the integration domain then we take the boundary conditions

$$\underline{\boldsymbol{A}}(z_e) = \begin{pmatrix} A(z_e) \\ B(z_e) \end{pmatrix} = \begin{pmatrix} 1 \\ 0 \end{pmatrix}. \tag{3.113}$$

We want to analyse the error between the limit solution and the multi-layer solution. As model setup, we again choose the linearly increasing profile (3.97). Our analysis consists of two parts. The first one is an error computation over a large domain of wavenumbers and frequencies while keeping the number of discretisation levels constant at $J = 512$ to show that the error is small over the whole wavenumber-frequency-domain. The second one chooses several specific points in this domain and tracks the error for an increasing number of levels J, up to $J = 10^5$.

The results of the first part can be seen in figure 3.8. For the left panel, we derived the transmission coefficient from the multi-layer method with $J = 512$ layers, the right panel shows the transmission coefficient computed from solving equation (3.90) numerically. It is impossible to spot any difference between the two frames. Computing the relative error yields the estimate

$$\max_{\omega,\lambda_x} \frac{|TC_d(\omega,\lambda_x) - TC_l(\omega,\lambda_x)|}{|TC_l(\omega,\lambda_x)|} < 7 \cdot 10^{-6} \tag{3.114}$$

For the second analysis, we fix specific wave parameters, i.e, a pair $(\lambda_{x,0}, \omega_0)$ of wavelength and frequency, and analyse how the relative error develops for increasing J. In particular, we perform the calculation for three different wavelength-frequency-pairs. We choose $\omega_0 = \frac{N_b}{\sqrt{2}}$ for all three cases and have a look at the wavelengths $\mathit{\Delta}_z, 2\mathit{\Delta}_z$ and $10\mathit{\Delta}_z$. The results can be seen in figure 3.9.

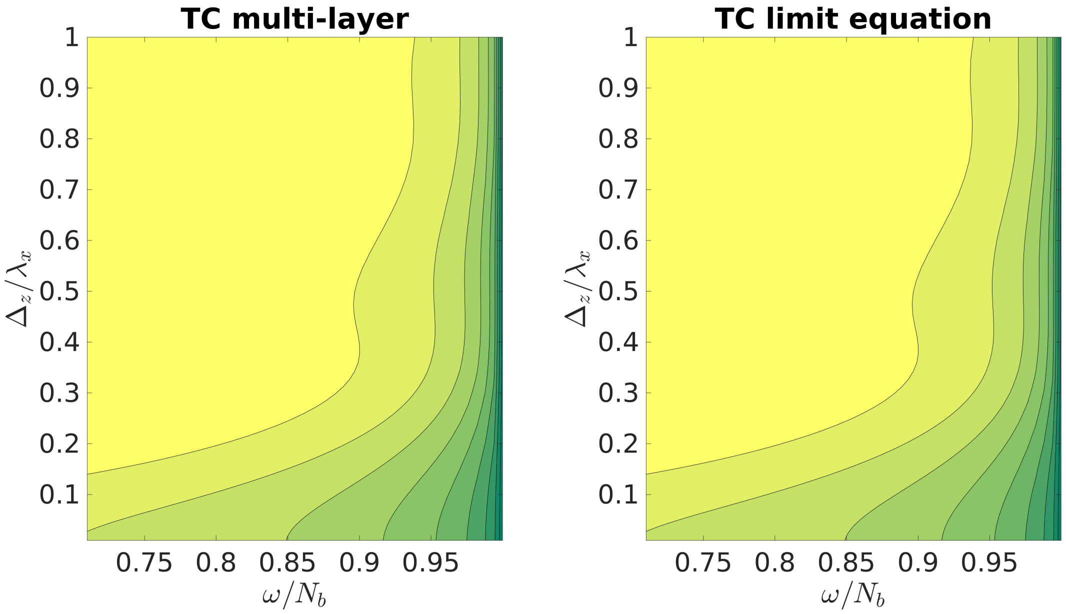

Figure 3.8: The left panel shows the multi-layer method with $J = 512$ steps and the right panel shows the values of the transmission coefficient computed from the numerical evaluation of the limit approach. At every single point in the domain, the error is smaller than 10^{-5}

We computed the relative error of the limit solution and the discrete solution for several numbers of layers J, that were logarithmically spaced between 10^1 and 10^5. For any two adjacent points, we computed the slope in the log-log diagram and for every wavelength, the mean and the standard deviation of all computed slopes. We found the mean slopes to be $\mu_l = -2.0050 \pm 0.0314$, $\mu_m = -2.0073 \pm 0.0533$ and $\mu_r = -2.0269 \pm 0.1184$, where the indices correspond to the left, middle and right panel of figure 3.9. In the the last few values are around the tolerance of the numerical scheme, hence there are somewhat larger fluctuations. But nonetheless, we observe that in all three test cases, the error decreases quadratically with the number of steps, until the error reaches the region where the tolerance of the scheme and the machine precision prevent a more precise computation. This is in line with the convergence order we found in subsection 3.4 for the solution itself. Even for a coarse discretisation with $J = 100$ layers, the relative error is about 10^{-5}. This justifies our choice of $J = 128$ layers in the previous sections.

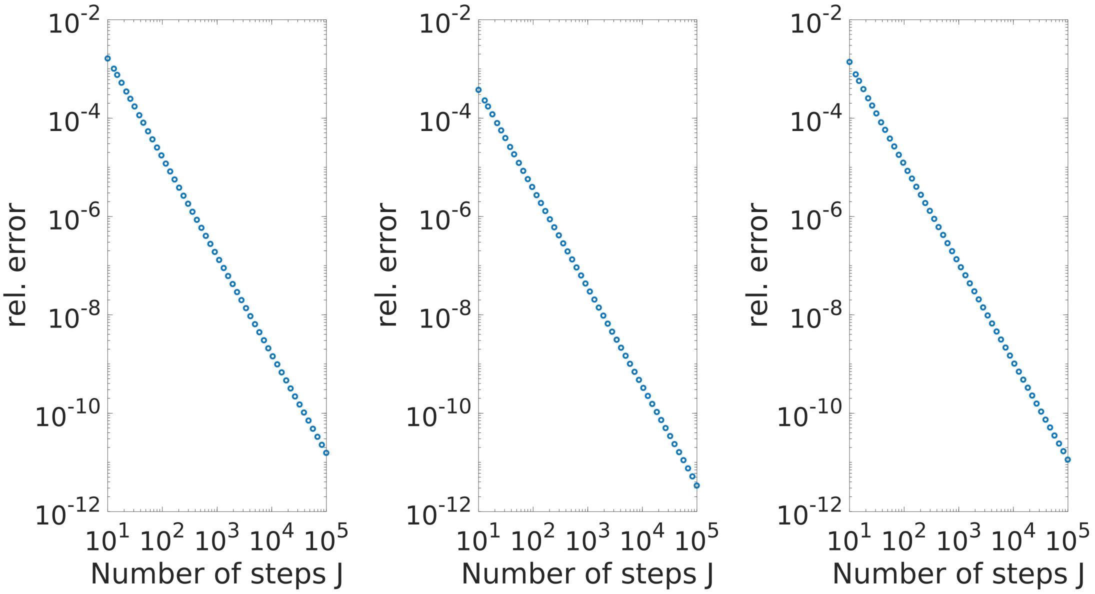

Figure 3.9: Relative error for profile (3.97) with $N_t = 2N_b$, $\omega_0 = \frac{N_b}{\sqrt{2}}$ and different horizontal wavelengths λ_x: $\lambda_x = \Delta_z$ in the left panel, $\lambda_x = 2\Delta_z$ in the middle panel and $\lambda_x = 10\Delta_z$ in the right panel. The mean slope of the different plots is nearly the same, namely $\mu \approx -2$. This means that the relative error decreases quadratically with the number of steps.

4 Wave transmission with background wind

Wind plays a major role in many atmospheric phenomenons. Gravity wave propagation is no exception to this. Although the wind generally changes over time, we are usually interested in short time scales only. Moreover, we focus on small amplitude waves, effectively neglecting wave-mean flow interactions. This leads to the assumption of a time-independent, but vertically varying background wind.

When including background wind to our method, there are two major cases: constant and non-constant wind. The first one is a straight-forward extension to the theory developed in last section, the second one requires more attention. Height-dependent wind is a crucial topic in atmospheric flows, especially around the tropopause, where strong winds can be present (Gisinger et al., 2017). A major part of the work presented in this chapter is discussed in Pütz and Klein (2018), which has been submitted to a peer-reviewed journal.

4.1 Constant wind

Let us assume that we have a constant background wind $\overline{u} \equiv u_0$. The linearised Boussinesq equations then take the form

$$\frac{\partial u}{\partial t} + u_0 \frac{\partial u}{\partial x} + c_p \theta_0 \frac{\partial \Pi}{\partial x} = 0 \tag{4.1a}$$

$$\frac{\partial w}{\partial t} + u_0 \frac{\partial w}{\partial x} + c_p \theta_0 \frac{\partial \Pi}{\partial z} + c_p \theta \frac{\partial \overline{\Pi}}{\partial z} = 0 \tag{4.1b}$$

$$\frac{\partial \theta}{\partial t} + u_0 \frac{\partial \theta}{\partial x} + w \frac{\mathrm{d}\overline{\theta}}{\mathrm{d}z} = 0 \tag{4.1c}$$

$$\frac{\partial u}{\partial x} + \frac{\partial w}{\partial z} = 0. \tag{4.1d}$$

Using a plane wave ansatz in x and t, i.e.

$$f(x, z, t) = \hat{f}(z) \exp(i(kx - \omega t)), \tag{4.2}$$

for the dynamic variables $f \in \{u, w, \theta, \Pi\}$, we can derive an ordinary differential equation in z for either of them, similar to the derivation of equation (3.7) in the previous chapter.

We stick to vertical wind as quantity of interest and obtain

$$\frac{\mathrm{d}^2\hat{w}}{\mathrm{d}z^2}(z) + k^2\left(\frac{N(z)^2}{(\omega - ku_0)^2} - 1\right)\hat{w}(z) = 0, \tag{4.3}$$

This is the Taylor-Goldstein equation for constant background wind. Note that it would have also been possible to obtain a partial differential equation for w from equation system (4.1), similar to equation (3.5), but since we are interested in plane wave transmission anyway, we opted to plug in the plane wave ansatz before reducing the equation system, which makes the calculation less cumbersome.

The term $\omega - ku_0$ is called relative frequency, here and in the majority of the literature denoted as $\hat{\omega}$. This is the frequency an observer moving with the constant velocity u_0 would see, in comparison to the absolute frequency ω that a fixed , usually ground-based, observer would see. We avoid using the terms “intrinsic” and “extrinsic” frequency, as they are not used uniformly by all researchers in the field. Additionally, the terms “absolute” and “relative” give a better intuition, as the observer either has an absolute, fixed position or is moving relatively to the ground with the mean flow. Along the lines of having no background wind, waves can propagate when their relative frequency is between zero and the ambient Brunt-Väisälä frequency. Apart from this change, the remainder of the theory is still valid and can be applied as derived in chapter 3.

4.2 Height dependent wind

Let us assume now a horizontal background wind that changes with height, i.e. $\overline{u}(z)$. The linearised Boussinesq equations now include also vertical derivatives of $\overline{u}$. They are written out as

$$\frac{\partial u}{\partial t} + \overline{u}\frac{\partial u}{\partial x} + w\frac{\mathrm{d}\overline{u}}{\mathrm{d}z} + c_p\theta_0\frac{\partial \Pi}{\partial x} = 0 \tag{4.4a}$$

$$\frac{\partial w}{\partial t} + \overline{u}\frac{\partial w}{\partial x} + c_p\theta_0\frac{\partial \Pi}{\partial z} - \frac{g\theta}{\theta_0} = 0 \tag{4.4b}$$

$$\frac{\partial \theta}{\partial t} + \overline{u}\frac{\partial \theta}{\partial x} + w\frac{\mathrm{d}\overline{\theta}}{\mathrm{d}z} = 0 \tag{4.4c}$$

$$\frac{\partial u}{\partial x} + \frac{\partial w}{\partial z} = 0 \tag{4.4d}$$

Using the plane wave ansatz (4.2), we obtain the following ODE for $\hat{w}$, explicitly stating the z-dependence:

$$\frac{\mathrm{d}^2\hat{w}}{\mathrm{d}z^2}(z) + k^2\left(\frac{N(z)^2}{(\omega - k\overline{u}(z))^2} + \frac{\overline{u}''(z)}{k(\omega - k\overline{u}(z))} - 1\right)\hat{w}(z) = 0, \tag{4.5}$$

If we want to apply the multi-layer method, we now not only need to approximate $N(z)$, but also $\overline{u}(z)$. Moreover, the second derivative of $\overline{u}$ appears in the equation and represents another challenge that needs to be taken on. One could make the argument that by approximating $\overline{u}$ piecewise constant, that there is no curvature in each individual layer, hence one could just neglect the term involving $\overline{u}''$. But then, in the limit for the number of layers going to infinity, this term will not reappear. Therefore, one also must include an approximation of the background wind curvature. This can either be done by two different approaches. The first one would be an approximation of the second derivative by a finite difference, for example second order central differences

$$\overline{u}''(z_0) \approx \frac{\overline{u}(z_0 - h) - 2\overline{u}(z_0) + \overline{u}(z_0 + h)}{h^2}, \tag{4.6}$$

where h denotes a small step size. It would be convenient to choose, sticking to the notation of the previous chapter, $h = \varDelta_z / J$ and z_0 to be the same points at which we approximate N. The other method involves computing the second derivative of $\overline{u}$ explicitly (if possible) and use the value of $\overline{u}''$ at the points where we approximate N. As it turns out, both methods yield basically the same results. The error between both approaches is negligibly small. We will give specific values when we present the results for selected wind profiles in section 4.2.2. For the remainder of this work, we use the explicit expression for the second derivative of $\overline{u}$ and evaluate it at the same point as we do with $\overline{u}$ and N, since we also need to compute $\overline{u}''$ for a direct numerical simulation of equation (4.5).

4.2.1 An analysis of the different matching conditions

When applying the multilayer method, we have to match the local solutions at the interfaces. The proof of convergence for the multi-layer method in an atmosphere at rest (see section 3.4) also applies in the case with background wind, as there where no further requirements on m, as long as we evaluate N, $\overline{u}$ and $\overline{u}''$ at the same point (which we do by construction of the method). This again transfers to matching conditions that require the solution and its derivative to be continuous at the interfaces. We will relate to them as the *mathematical* matching conditions. Despite already knowing how to match the solutions at the layer interfaces, there is a reason to spend a section on discussing this topic.

When browsing through the literature on the topic of layering the atmosphere in multiple layers, one finds that most of the research uses the classical matching ansatz derived by Drazin and Reid (1981). They analysed the stability of inviscid parallel shear flow of an unstratified fluid, hence the matching conditions are derived for Rayleigh's stability equation, which is just equation (4.5) with $N \equiv 0$, and also for piecewise linear background flow profiles. As this is certainly valid for their setup, the conditions themselves cannot be transferred one-to-one to our method, because we consider not only discontinuities in N, but also in $\overline{u}$. This in turn leads to discontinuities in the relative frequency which is a point that was not considered in the original derivation of Drazin and Reid (1981). Using the physical interpretation of those conditions, i.e. that vertical wind and pressure are continuous at the layer interfaces, we arrive at matching conditions that differ from both the classical conditions of (Drazin and Reid, 1981) and the mathematical conditions we derived earlier. And although the matching conditions converge towards each other in the limit of infinite layers, it is not clear that the solutions they produce will show the same behaviour. And since we know that the solution using the mathematical conditions converges to the real solution, the solution using the classical conditions would not, if it differs from the solution with the mathematical matching conditions. As we will see, this is going to be the case.

So let us derive mathematical expressions for the classical matching ansatz. The first one of the new matching conditions is acquired fairly easily, since equation (4.5) is stated for the vertical wind w. The second condition can be found when using the horizontal momentum equation (4.4a) and the divergence constraint (4.4d) to eliminate u from the former. Mathematically, this can be written as

$$\varDelta\left[w\right] = 0 \tag{4.7a}$$
$$\varDelta\left[\hat{\omega}w' - ik\overline{u}'w\right] = 0 \tag{4.7b}$$

at each layer interface, where again $\varDelta[f](z_0)$ is the jump operator defined in equation (3.22). It is interesting to note that this approach coincides with the mathematical conditions in the case of constant background wind since $\hat{\omega}$ is constant and $\overline{u}' = 0$.

As done in section 3.2, we derive a relation at each layer interface z_j:

$$w_j(z_j) = w_{j+1}(z_j{+}1), \tag{4.8a}$$
$$\hat{\omega}_j w_j(z_j) - ik\overline{u}_j' w_j(z_j) = \hat{\omega}_{j+1} w_{j+1}(z_j) - ik\overline{u}_{j+1}' w_{j+1}(z_j). \tag{4.8b}$$

Here, the subscripts j and $j{+}1$ for $\hat{\omega}$ and $\overline{u}$ indicate their approximations in the respective layers. Using the local solution (3.19) in each layer, together with the adapted vertical wavenumber

$$m_j = -k\sqrt{\frac{N_j^2}{(\omega - k\overline{u}_j)^2} + \frac{\overline{u}_j''}{k(\omega - k\overline{u}_j)} - 1}, \tag{4.9}$$

we find a relation

$$\begin{pmatrix} A_{j+1} \\ B_{j+1} \end{pmatrix} = \boldsymbol{M}_j^{(c)} \begin{pmatrix} A_j \\ B_j \end{pmatrix}. \tag{4.10}$$

Again, $\boldsymbol{M}_j^{(c)}$ is a 2-by-2 matrix with the superscript indicating that it corresponds to the classical conditions. The matrix entries can be derived in a similar way as displayed in section 3.2 for the mathematical conditions. We obtain

$$M_{1,1}^{(c)} = \frac{m_j\omega_j + m_{j+1}\omega_{j+1} - k(\overline{u}_j' - \overline{u}_{j+1}')}{2m_{j+1}\omega_{j+1}} \exp(i(m_j - m_{j+1})z_j), \tag{4.11a}$$

$$M_{1,2}^{(c)} = -\frac{m_j\omega_j - m_{j+1}\omega_{j+1} + k(\overline{u}_j' - \overline{u}_{j+1}')}{2m_{j+1}\omega_{j+1}} \exp(-i(m_j + m_{j+1})z_j), \tag{4.11b}$$

$$M_{2,1}^{(c)} = -\frac{m_j\omega_j - m_{j+1}\omega_{j+1} - k(\overline{u}_j' - \overline{u}_{j+1}')}{2m_{j+1}\omega_{j+1}} \exp(i(m_j + m_{j+1})z_j), \tag{4.11c}$$

$$M_{2,2}^{(c)} = \frac{m_j\omega_j + m_{j+1}\omega_{j+1} - k(\overline{u}_j' + \overline{u}_{j+1}')}{2m_{j+1}\omega_{j+1}} \exp(-i(m_j - m_{j+1})z_j). \tag{4.11d}$$

Constructing a solution from the mathematical conditions in the case of non-constant background wind leads to the same relations as in section 3.2, except for the difference in the computation of the vertical wavenumber, which is now given my equation (4.9).

We depict an example for chosen background and wave parameters. This should make the right choice of matching conditions clear at first sight. In the presented case, the stratification is uniform ($N \equiv N_0$) over the whole domain and the wind profile is bell-shaped, i.e.

$$U(z) = U_0 \exp\left(-\frac{(z-z_0)^2}{\sigma^2}\right). \tag{4.12}$$

Far away from z_0, the value for the background wind is very close to zero, so that we only need to consider a confined area around z_0 as region of non-uniform background and choose $U \equiv 0$ outside of it. The interval we choose for the computation is $I_c = [z_0 - 5\sigma, z_0 + 5\sigma]$. The value at the interval boundaries is $1.39 \cdot 10^{-11} U_0$, and because of the shape of the function, this is also the supreme value outside of I_c. Moreover, we chose $U_0 = 0.5\,\mathrm{ms}^{-1}$, $\sigma = 100\,\mathrm{m}$ and $\lambda_x = \lambda_z = 2000\,\mathrm{m}$.

Figure 4.1 shows plots of the maximal normalised error between the numerical and multilayer solution. Normalised error means that we are looking at the absolute error, but normalised by the maximal value of the numerical solution. We chose this error computation over a classical relative error computation because we have oscillating functions and as soon as the zeros of the functions do not match, the relative error gets large and does not give qualitative information about how well one method approximates the other. Mathematically, for a fixed number of layers J, we compute

$$e_J = \frac{\max_{z\in D} \left| w_{\mathrm{ml}}^{(J)}(z) - w_{\mathrm{num}}(z) \right|}{\max_{z\in D} \left| w_{\mathrm{num}}(z) \right|}, \tag{4.13}$$

where $w_{\mathrm{ml}}^{(J)}$ is the multi-layer solution for J layers, w_{num} is the solution obtained by direct numerical solution of equation (4.5) and D is the domain of interest, which should at

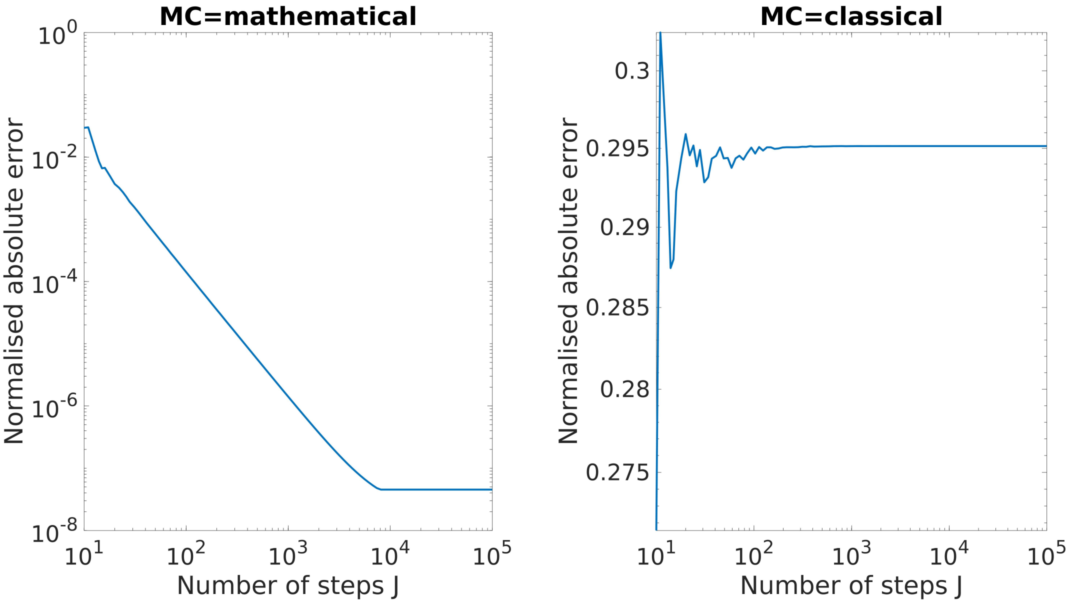

Figure 4.1: Here, we see the normalised absolute error of the multi-layer solution compared with a DNS of equation (4.5), plotted over the number of layers. The left panel uses the mathematical matching conditions, the right panel uses the classical ones.

least cover the region of non-uniform wind and stratification. In the left panel , we see the results for the mathematical matching conditions. There is a decrease of the error, up to a point where the error reaches the precision of the numerical scheme (which is the MATLAB built-in ode45 scheme). This happens at about 5000 layers. Between 100 and 4000 layers, the slope of the graph is $\mu = -1.9388 \pm 0.1105$. Since both axes are spaced logarithmically, this indicates a convergence of order 2. In the right panel, we show the result for the classical matching conditions. Although the method seems converge to a limit, this limit does not coincide with the numerical solution.

Figure 4.2 shows the numerical solutions and the multi-layer solutions with either matching conditions, created via the finite-element ansatz discussed in section 3.4. While the numerical solution and the one with the mathematical matching conditions are basically indistinguishable, we can clearly see that the solution with the classical matching conditions differs from both others. Note that the solutions were initialised so that they all agree right of the non-uniform layer, which is located between the two vertical lines.

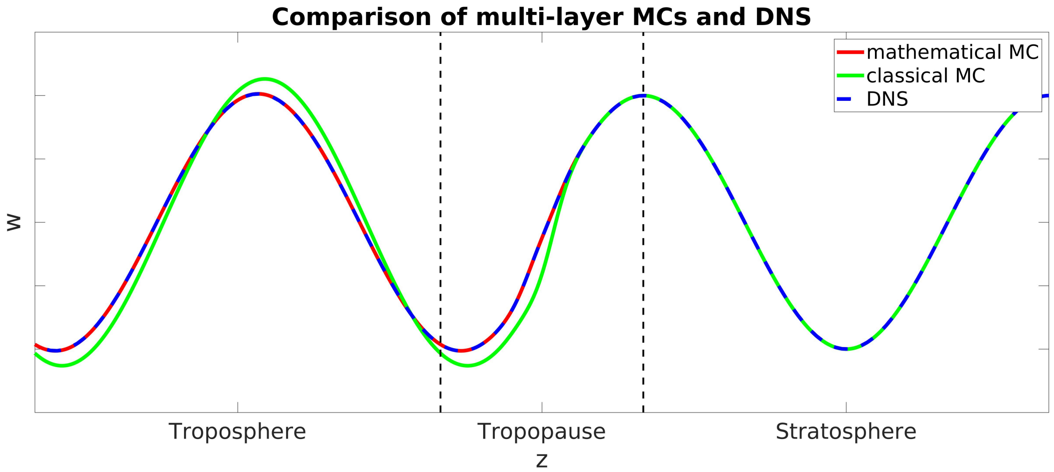

Figure 4.2: Comparison of different methods to solve equation (4.5). The dashed blue curve is a direct numerical simulation (DNS) of equation (4.5), the solid red curve is obtained with the multi-layer method and the mathematical matching conditions and the solid green curve uses the classical matching conditions.

4.2.2 Results for a cosine-shaped wind profile

This section is about the results for various background wind profiles. We start with some a priori thoughts. We recall the dispersion relation (4.9)

$$m = -k\sqrt{\frac{N^2}{(\omega - k\overline{u})^2} + \frac{\overline{u}''}{k(\omega - k\overline{u})} - 1}. \tag{4.14}$$

We see that there can be 2 crucial cases. First, the radiant can become zero, similar as in the reflection layer case we know from section 3, but with the possibility that it not only may occur via weakening stratification, but also via a change in the background wind. The difference between the case discussed here and the case without background wind is that the Doppler shift appears in the horizontal group velocity

$$\frac{\partial\omega}{\partial k} = \frac{Nm^2}{\sqrt{k^2 + m^2}^3} + U. \tag{4.15}$$

In terms of ray tracing, the ray path would be a loop at the reflection level which is tangential to the horizontal at the reflection level instead of approaching it with a cusp (see Sutherland (2010), Chapter 6.5.3, for a more detailed discussion). But since we are not solving the ray equations, it does not matter how the reflection level is generated. Therefore its treatment works in a similar way as without wind.

The other crucial case that could in fact not appear with constant background wind is that the denominator of the first (and hence also the second) term in the radiant goes to zero, causing the whole radiant to approach infinity. This is in the common literature denoted as critical level. At such a level, the vertical wavenumber theoretically is infinity. Ray theory predicts that waves approach this level asymptotically, but never reach it. However, ray theory is no longer valid around a critical layer. Most likely, due to the rapid oscillations, the wave becomes unstable and breaks, dissipating its energy during that process. Since this is a very non-linear behaviour and our theory is built on linear approximations, the multi-layer method does not provide any further insights to the evolution of waves around critical levels. But since this critical level occurs usually at a certain altitude, the multi-layer method is suitable to describe the wave amplitude evolution up to a certain point below and above the critical level and one could try to find an approximate solution of the describing equation around the critical level, for example via rescaling and using a perturbation ansatz or a Frobenius method approach, similar to what was done in Nault and Sutherland (2007). Then, matching this to the multi-layer solution could yield a solution, but this is not part of the research presented here.

Next, we want to define a meaningful transmission coefficient for the case of non-constant background wind, because wave energy is not conserved when the wind changes with height. To see this, we go the same way as we did with deriving the energy conservation law (3.34) for a steady atmosphere. The equation that results from this procedure is

$$\frac{\partial E}{\partial t} + \nabla \cdot (\vec{c}_g E) = -uw\frac{\mathrm{d}\overline{u}}{\mathrm{d}z}, \tag{4.16}$$

so the time-dependent change of wave energy is not only due to the energy flux divergence, but is also influenced by the vertical shear. It is however possible to find a conserved quantity, namely the ratio of wave energy and relative frequency. This is called wave action in the common literature and denoted via

$$\mathcal{A} = \frac{E}{\hat{\omega}} \tag{4.17}$$

To see that this is conserved, we have a look at

$$\frac{\partial \mathcal{A}}{\partial t} + \nabla \cdot (\vec{c}_g \mathcal{A}), \tag{4.18}$$

which can be rewritten as

$$\frac{1}{\hat{\omega}}\left(\frac{\partial E}{\partial t} + \nabla \cdot (\vec{c}_g E)\right) + c_{g_z} E \frac{\mathrm{d}\hat{\omega}^{-1}}{\mathrm{d}z}. \tag{4.19}$$

The x- and t-derviatives of $\hat{\omega}$ have vanished as it depends only on z. Executing the last derivative yields the equation

$$\frac{1}{\hat{\omega}}\left(\frac{\partial E}{\partial t}+\nabla\cdot(\vec{c}_g E)\right)+\frac{c_{g_z}Ek}{\hat{\omega}}\frac{\mathrm{d}\overline{u}}{\mathrm{d}z}. \tag{4.20}$$

Using the polarization relations (3.10), (3.11) and (3.12) (note that absolute frequency must be replaced by relative frequency here), the previous expression can be transformed into

$$\frac{1}{\hat{\omega}}\left(\frac{\partial E}{\partial t}+\nabla\cdot(\vec{c}_g E)+uw\frac{\mathrm{d}\overline{u}}{\mathrm{d}z}\right). \tag{4.21}$$

Togehter with equation (4.16), we deduce that expression (4.21) equates to 0. This gives the wave action conservation law

$$\frac{\partial \mathcal{A}}{\partial t}+\nabla\cdot(\vec{c}_g \mathcal{A})=0 \tag{4.22}$$

In a similar fashion to section 3.3, we take the horizontal average, find temporal independence of the wave action and find that the vertical flux of horizontally averaged wave action $c_{g_z}\langle\mathcal{A}\rangle$ is conserved. In terms of vertical velocity wave amplitude, this is

$$c_{g_z}\langle\mathcal{A}\rangle=\frac{\rho_b m}{2k^2}\left|A_w\right|^2. \tag{4.23}$$

Defining the transmission coefficient again as the ratio of incident and transmitted upward wave action fluxes, we find the very same formula as we have for the case of a steady atmosphere:

$$TC=\frac{m_{J+1}}{m_1}\left|\frac{A_{J+1}}{A_1}\right|^2 \tag{4.24}$$

Figure 4.3 shows the transmission coefficients for a uniformly stratified atmosphere and a cosine-shaped wind profile. The left panel shows a negative jet, i.e. the wind and the relative horizontal phase speed point in different directions. In this case, the jet can form a reflection layer, as we can see in the upper right part of the panel, where the transmission is very low. Note that without the background wind, the transmission coefficient would be equal to 1 everywhere.

The middle panel shows the results for a positive jet. In this case, we can have critical levels, as we can see in the upper left part of the panel. In this case, the multi-layer method does not converge, because the vertical wavenumber goes to infinity. The values we get in this area are useless, since no matter how large the number of layers is, the resolution at some point will still not be fine enough. Nonetheless, we get a good glimpse which choice of wave parameters leads to the wave encountering a critical layer.

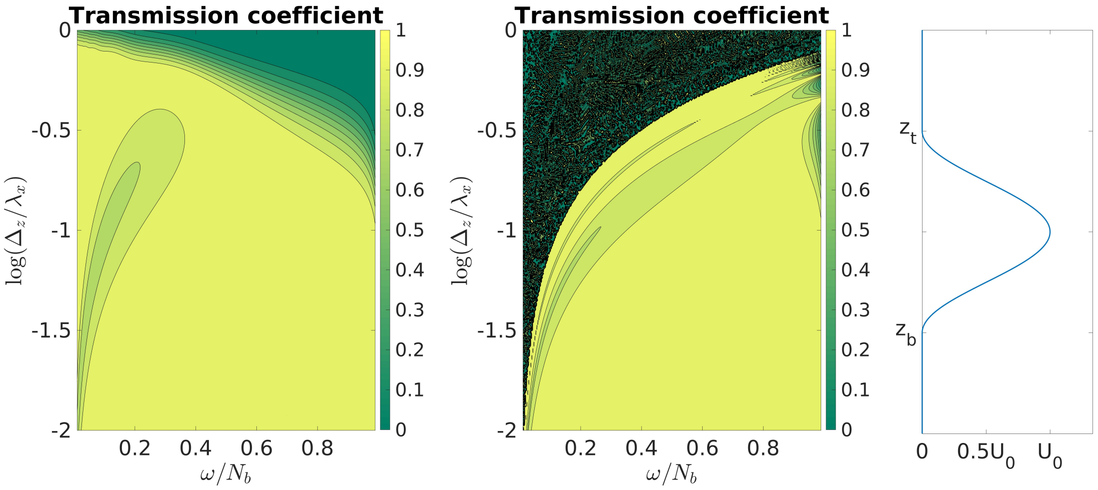

Figure 4.3: Transmission coefficient for a cosine-shaped wind profile as displayed in the right panel. In the left panel, $U_0 = -2\,\mathrm{ms}^{-1}$, in the middle panel, $U_0 = 2\,\mathrm{ms}^{-1}$.

4.3 Limit solution in the case of non-zero background wind

Since we know from the last section that we have the same matching conditions as in the case without background wind, the limit of the number of layers tending to infinity will yield the same equation that was derived in section 3.5, i.e. equation (3.90). The major difference is that the vertical wavenumber is now given by

$$m(z) = -k\sqrt{\frac{N(z)^2}{(\omega - k\overline{u}(z))^2} + \frac{\overline{u}''(z)}{k(\omega - k\overline{u}(z))} - 1}. \tag{4.25}$$

Hence, the derivative of m, which appears in the matrix entries of equation (3.90), now not only involves the derivative of N, but also the first three derivatives of $\overline{u}$. The exact equation is

$$m'(z) = \frac{-k\left(\frac{2N(z)N'(z)}{(\omega-k\overline{u}(z))^2} + \frac{2kN(z)\overline{u}'(z)}{(\omega-k\overline{u}(z))^3} + \frac{\overline{u}'''}{k(\omega-k\overline{u}(z))} + \frac{\overline{u}''\overline{u}'}{(\omega-k\overline{u}(z))^2}\right)}{2\sqrt{\frac{N(z)^2}{(\omega-k\overline{u}(z))^2} + \frac{\overline{u}''(z)}{k(\omega-k\overline{u}(z))} - 1}}. \tag{4.26}$$

Fortunately, the numerical evaluation for this is still manageable as long as there are no reflection or critical levels and we obtain convergence of the multi-layer method towards the solution of equation (3.90). One more thing to note is that in the case of no reflection or critical level, the matrix $\mathcal{M}$ is analytic in an open subset of $\mathbb{C}$ containing the region of non-uniform background, and by the same arguments that were given in section 3.5, a unique analytic solution exists. We do not want too go to much into detail, as we do not gain much new insight from this limit. Although it is important that there exists an analytical solution, due to the good convergence behaviour of the multi-layer method, it is much more efficient to use it over a DNS of equation (3.90).

4.4 Scale analysis for curvature term

When studying literature on linear Boussinesq gravity waves, one discoveres that oftentimes, the equation which is used to describe the waves neglects the curvature term $u''/(k\hat{\omega})$. The question that comes up is how important that term actually is. In WKB theory (see for example Muraschko et al. (2015)), the dispersion relation derived from linear steady Boussinesq theory, in which the curvature term is excluded, is used, since the curvature term is of higher order. Hence we execute a scale analysis of all the terms occurring in the dispersion relation (4.14) and detect regimes, where the curvature term has a significant impact on the wavenumber. Moreover, we will compare transmission coefficient computations with and without it.

We assign some characteristic values to the terms and derive two dimensionless numbers in which the corresponding terms are expressed and which will yield as a basis for the scale analysis. Let U_0 be a (positive) characteristic value of $\overline{u}$, and let $\overline{u}$ change on a length scale H_U. Let L_x be a characteristic length scale for the horizontal wave length, i.e. $k \sim 1/L_x$ and let T_0 be a characteristic time scale, i.e. $N \sim 1/T_0$. We also choose $\omega \sim 1/T_0$, which corresponds to non-hydrostatic gravity waves, i.e. waves with frequencies close to the Brunt-Väisäla frequency. Then, the right hand side of equation (4.14) can be estimated as

$$\begin{aligned}&\frac{1}{L_x^2}\left(\frac{\frac{1}{T_0^2}}{\left(\frac{1}{T_0}-\frac{U_0}{L_x}\right)^2}+\frac{\frac{U_0}{H_U^2}}{\frac{1}{L_x}\left(\frac{1}{T_0}-\frac{U_0}{L_x}\right)}-1\right)\\ \Leftrightarrow&\frac{1}{L_x^2}\left(\left(1-\frac{T_0U_0}{L_x}\right)^{-2}+\frac{L_x^2}{H_U^2}\left(1+\frac{L_x}{T_0U_0}\right)^{-1}-1\right).\end{aligned} \tag{4.27}$$

We define

$$\alpha := \frac{L_x}{H_U}, \tag{4.28}$$

$$\beta := \frac{L_x}{T_0U_0}. \tag{4.29}$$

α gives the relation between horizontal wavelength and the scale of variation of the background wind. As we are assuming non-hydrostatic waves, the vertical wavelength can roughly be taken to be of the same order of magnitude as the horizontal wavelength. Hence, α can also be seen as a quantity that tells us if the waves have a short, comparable or long wave length compared to the length scale of the background wind. β can be seen as the ratio between phase speed of the wave and background wind speed, basically telling us which of the two is larger or if they are comparable in size. Then, the above equation writes as

$$\frac{1}{L_x^2}\left(\left(1-\beta^{-1}\right)^{-2}+\alpha^2\left(\beta-1\right)^{-1}-1\right) \tag{4.30}$$

In the way we chose our reference quantities, the term representing the curvature, U_0/H_U^2, is always positive, but in reality, it can be negative. We are, however, only interested in the magnitude of the second term, so this does not affect the case analysis. We first carry out a scaling analysis where α and β can vary independently. This will be followed by a discussion where we link both values via a distinguished limit.

1. $\beta \ll 1$. Then $\left(1-\beta^{-1}\right)^{-2} \ll 1$ and $|\beta-1|^{-1} \sim 1$.
    a) $\alpha \ll 1$. Then $\alpha^2\,|\beta-1|^{-1} \ll 1$, hence the third term is dominant.
    b) $\alpha \sim 1$. Then $\alpha^2\,|\beta-1|^{-1} \sim 1$, hence the second and third term are dominant.
    c) $\alpha \gg 1$. Then $\alpha^2\,|\beta-1|^{-1} \gg 1$, hence the second and third term are dominant.
2. $\beta \sim 1$. Then $\left(1-\beta^{-1}\right)^{-2} \gg 1$ and $|\beta-1|^{-1} \sim 1$.
    a) $\alpha \ll 1$. Then $\alpha^2\,|\beta-1|^{-1} \ll 1$, hence the first term is dominant.
    b) $\alpha \sim 1$. Then $\alpha^2\,|\beta-1|^{-1} \sim 1$, hence the first term is dominant.
    c) $\alpha \gg 1$. Then $\alpha^2\,|\beta-1|^{-1} \gg 1$. Here a distinguished limit for α and β is needed to determine which of the first two terms is dominant.
3. $\beta \gg 1$. Then $\left(1-\beta^{-1}\right)^{-2} \sim 1$ and $|\beta-1|^{-1} \ll 1$. This case has to be treated with special care, since the sign of the first term is always positive while that of the third is always negative. Hence it may very well be possible that their difference is very small, resulting in the second term being dominant.
    a) $\alpha \ll 1$. Then $\alpha^2\,|\beta-1|^{-1} \ll 1$.
    b) $\alpha \sim 1$. Then $\alpha^2\,|\beta-1|^{-1} \ll 1$.
    c) $\alpha \gg 1$. Then $\alpha^2\,|\beta-1|^{-1}$ either is ~ 1 or $\gg 1$. We need a distinguished limit for α and β, but in either case, the second term is among the dominant ones.

So the cases where the second term may play an important role are 1b, 1c, 2c and 3. We can reduce the amount of analysis to be made by choosing typical atmospheric reference values and rule out some of the regimes that are unrealistic.

For further analysis, we can relate α and β by a distinguished limit, i.e.

$$\beta = \alpha^c. \tag{4.31}$$

As we already figured out by the first part of the scaling analysis, the cases where a distinguished limit is needed to determine the dominant term are 2c and 3c, i.e. $\alpha \gg 1$ and $\beta \sim 1$ or $\beta \gg 1$, so we assume now that $\alpha \gg 1$.

The cases $c = 0$ results in $\beta = 1$, which means that background wind speed and wave phase velocity are the same. This corresponds to a critical level and requires special attention. This is, however, not the purpose of this work and is left for future research.

For the case $c < 0$, we obtain $\beta \ll 1$, which is not a case of interest here. The remaining values for c can basically be classified in two categories: $0 < c \ll 1$, for which $\beta \sim 1$ and all remaining positive values for c, which yield $\beta \gg 1$.

With the help of equation (4.31), we can write the term (4.30) as

$$\frac{1}{\left(1 - \frac{1}{\alpha^c}\right)^2} + \frac{\alpha^2}{\alpha^c - 1} - 1 \tag{4.32}$$

We equate the first and the second term and obtain the equation

$$\alpha^{2c-2} = \alpha^c - 1. \tag{4.33}$$

If we can solve this for c, we would have found the values where both terms coincide. With the help of a computer algebra system, we find the solutions to be

$$c_{+,-} = \ln(\alpha)^{-1} \ln\left(\frac{\alpha^2}{2} \pm \alpha\sqrt{\frac{\alpha}{4} - 1}\right) \tag{4.34}$$

For large α, one of the values is close to 2, while the other is close to 0. So when we have $c_- < c < c_+$, the second term in expression (4.32) is the dominant one, meaning overall that the curvature term has a non-negligible effect in these cases.

A typical atmospheric buoyancy period is $T_0 = 100\,\mathrm{s}$, which corresponds to a stratification strength of $N_0 = 0.01\,\mathrm{s}^{-1}$, a value often used in the troposphere. Waves usually oscillate faster in the stratosphere due to stronger stability there. As a reference horizontal scale, we choose $L_x^{(1)} = 50000\,\mathrm{m}$ corresponding to long waves, $L_x^{(2)} = 5000\,\mathrm{m}$ for waves of intermediate length and $L_x^{(2)} = 500\,\mathrm{m}$ for short waves. Now let us look at

$$\beta \ll 1 \Leftrightarrow \frac{L_x}{T_0 U_0} \ll 1 \Leftrightarrow U_0 \gg \frac{L_x}{T_0} \tag{4.35}$$

For long waves, the term on the right-hand side of the last equation is $500\,\mathrm{ms}^{-1}$ and for medium waves $50\,\mathrm{ms}^{-1}$, hence, the requirement of U_0 being much larger than this is very unrealistic in upper troposphere and lower stratosphere regimes. For shorter waves, the term is $5\,\mathrm{ms}^{-1}$. U_0 must still be pretty large, but the tropopause jet can reach velocities of like 30 to $50\,\frac{\mathrm{m}}{\mathrm{s}}$ (see for example Gisinger et al. (2017)). The relevant cases then are $\alpha \sim 1 \Leftrightarrow L_x^{(3)} \sim H_U$ and $\alpha \gg 1 \Leftrightarrow L_x^{(3)} \gg H_U$. The second case is completely unrealistic, since it requires the background wind to vertically increase very strongly over just a few tens of meters. The second case is still very unlikely, but one could argue that it corresponds to a very strong jet stream.

For

$$\beta \sim 1 \Leftrightarrow \frac{L_x}{T_0 U_0} \sim 1 \Leftrightarrow U_0 \sim \frac{L_x}{T_0}, \tag{4.36}$$

the long-wave regime is completely unrealistic with $U_0 \sim 500\mathrm{ms}^{-1}$, while the medium-wave regime is on the edge of reality with $U_0 \sim 50\mathrm{ms}^{-1}$. When looking at the relevant α-regime, i.e. $\alpha \gg 1 \Leftrightarrow L_x^{(2)} \gg H_U$, this can be a realistic scaling for a strong tropospheric jet, where the wind strongly increases over a few hundred meters. For short waves, the reference velocity is about $5\frac{m}{s}$, and the rate of increase in the case of $\alpha \gg 1$ is the same as in the strong jet stream case in the aforementioned paragraph and is also realistic.

The relation

$$\beta \gg 1 \Leftrightarrow \frac{L_x}{T_0 U_0} \gg 1 \Leftrightarrow U_0 \ll \frac{L_x}{T_0}, \tag{4.37}$$

is in general true. Let us now assume $\left(1-\beta^{-1}\right)^{-2} - 1 \sim 1$. Then, the relevant regime is $\alpha \gg 1 \Leftrightarrow L_x \gg H_U$. Although the scale of variation of U is small, the amount it changes is also small, e.g. for medium waves, the wind increases by about $5\mathrm{ms}^{-1}$ over a few hundred meters, which is very realistic. With a distinguished limit

$$\alpha \sim \beta \Leftrightarrow H_U \sim U_0 T_0 \tag{4.38}$$

for example, we get that the second term is dominant. The distinguished limit can be understood that the horizontal advection over one buoyancy period has the same length as the scale of variation of the background wind.

The scale analysis revealed only the effect the curvature term has on the vertical wavenumber. But this may also affect wave transmission and reflection, for example, if the curvature term causes the radiant to become negative, effectively causing the wave to encounter a reflection level, which it may otherwise not have. The scale analysis shows that the curvature term plays a minor role in most of the realistic cases, most notably in the classical WKB regime, where this term is usually neglected.

Figure 4.4 shows a parameter range for which transmission coefficients are computed. We use a constant stratification $N_0 = 0.01\,\mathrm{s}^{-1}$ and a bell-shaped wind profile

$$\overline{u} = u_0 \exp\left(-\frac{(z-z_u)^2}{\sigma^2}\right), \tag{4.39}$$

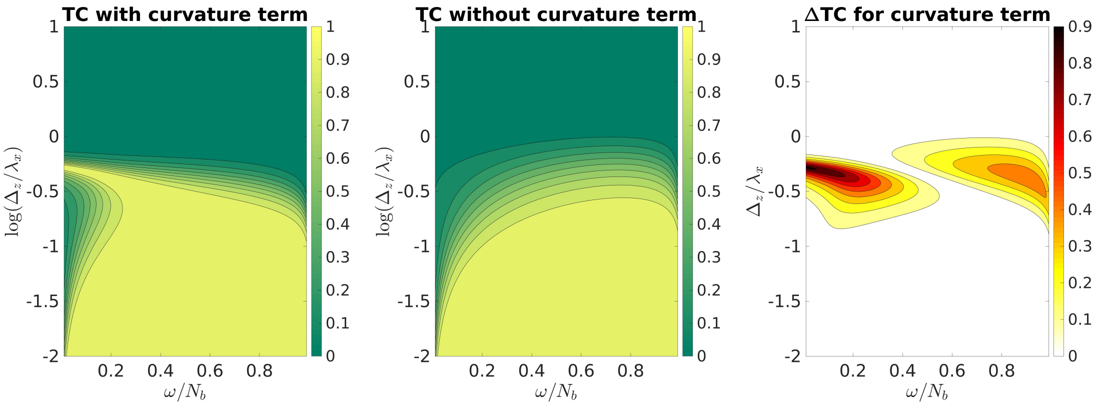

Figure 4.4: The left panel shows the transmission coefficient computed with the curvature term, the middle panel shows the computation without the curvature term. In the right panel, we see the absolute value of their difference.

with $\sigma = 100\text{m}$ and $u_0 = -5\text{ms}^{-1}$. The discretisation was made in the interval $[z_u - 5\sigma, z_u + 5\sigma]$, its length is $\mathit{\Delta}_z = 10\sigma = 1000\,\text{m}$ and z_u can be chosen arbitrarily. We use 300 frequencies, equally spaced between $0.01N_0$ and $0.99N_0$ as well as 300 logarithmically spaced horizontal wavelengths between 100 m and 100000 m. The number of layers is 200.

The left panel shows the computation that includes the curvature term, the middle one does not include the curvature term. Their absolute difference can be seen in the right panel. We can clearly see the influence the curvature term has, causing waves to either transmit better or worse. We detect two separated areas where the transmission behaviour differs significantly. Both occur for moderately large horizontal wavelengths. We see that hydrostatic waves, i.e. waves with small vertical wavelength compared to the horizontal wavelength, transmit much better than without the curvature term and non-hydrostatic waves are hindered in their transmission. To put this into the context of the scale analysis, we have a reference wavelength $L_x = 3000\,\text{m}$, a wind scale $H_U = 3\sigma = 300\,\text{m}$, a reference wind $U_0 = 5\text{ms}^{-1}$ and a timescale $T_0 = \sqrt{2}/N_0 \approx 141\,\text{s}$. This results in $\alpha = 10 \gg$ and $\beta \approx 4.25 \sim 1$. When we have a look at the scale analysis, this was exactly one of the regimes that we detected above in which the curvature term significantly impacts the vertical wavenumber.

In a similar fashion, it would be possible to derive a scale analysis for a hydrostatic wave scaling. This will not be taken on now but left for future research.

5 Wave packets

In chapters 3 and 4, the subject of study was a plane wave field, which technically extends infinitely in positive and negative vertical direction. Moreover, we focused on temporally periodic solutions (which are basically steady-state solutions in a coordinate frame moving with the constant horizontal phase velocity ω/k). In comparison to this, wave packets are confined in space and time. In the present chapter, we will extend the theory we developed in the preceding chapters so that it can be applied to wave packets. We will stay close to Pütz and Klein (2018), as a major part of this extension is also discussed there.

5.1 Basic thoughts on wave packets

For the interaction of small-amplitude gravity wave packets with the tropopause, we use again the linearised Boussinesq equations (2.13), but we will not be using a plane wave ansatz in x and t. Due to the explicit dependence of the solution on all 3 unknown variables, it is a priori not clear if the multi-layer method is applicable for wave packets, as we cannot derive a single ordinary differential equation that describes the evolution.

Luckily, it turns out that we can modify the multi-layer method and adapt it to the case of wave packets. To keep things simple, we first restrict ourselves to the case of quasi-1D wave packets, that are only confined in the vertical direction, but are still periodic in horizontal direction. A brief discussion on 2D wave packets can be found at the end of this chapter.

Starting points for the investigation are the linearised Boussinesq equations in a stationary atmosphere, i.e. equations (3.1). We can reduce them to a single equation for the vertical wind speed, as we already saw in equation (3.5), here again written for convenience

$$\left(\frac{\partial^2}{\partial x^2} + \frac{\partial^2}{\partial z^2}\right)\frac{\partial^2 w}{\partial t^2} + N^2\frac{\partial^2 w}{\partial x^2} = 0. \tag{5.1}$$

As in the previous chapters, N shall not depend on x. As we mentioned, we focus on horizontally periodic solutions. Hence, we set

$$w(x, z, t) = \tilde{w}(z, t)\exp(ikx), \tag{5.2}$$

where k denotes the horizontal wavenumber. This ansatz permits solutions that can be localised in z-direction and have explicit time dependence. This allows for an easier computation by not giving up the key aspects we are interested in, namely the evolution of the wave packet through a vertically non-uniform background. The resulting equation then reads

$$\left(k^2 + \frac{\partial^2}{\partial z^2}\right) \frac{\partial^2 \tilde{w}}{\partial t^2} + N^2 k^2 \tilde{w} = 0. \tag{5.3}$$

We will omit the tilde-superscript in the later equations.

For a constant stratification $N \equiv N_0$, plane waves are still solutions to equation (5.3). In particular, any function of the form

$$w(z,t) = A \exp(i(mz - \omega t)) + B \exp(-i(mz + \omega t)). \tag{5.4}$$

solves the equation as long as the vertical wavenumber m and the frequency ω are linked via the dispersion relation

$$\omega^2 = \frac{N_0^2 k^2}{k^2 + m^2}. \tag{5.5}$$

It is important to note that, although equation (5.3) is a fourth order equation, we assume the solution to depend only on the two unknown amplitudes A and B, as we assume $\omega > 0$, just like in the plane wave case. Although technically, there are two choices for either m and ω, they are linked via the dispersion relation (5.5). The two choices for m, which are m_+ and m_- with $m_- = -m_+$ can lead both to the same frequency branch. But the same is true for the frequency, so that we can a priori rule out two combinations by symmetry reasons.

Since equation (5.3) is linear, we can superimpose solutions to get new ones. A superposition of finitely many solutions is, in general, not periodic (an exception to this is when all wavenumbers are rational), but almost-periodic, i.e. for every $\varepsilon > 0$, there is a number $L_\varepsilon > 0$ such that in every interval $[z, z + L_\varepsilon]$, there is a number μ with

$$|f(z + \mu) - f(z)| < \varepsilon. \tag{5.6}$$

So the solutions, although not periodic, show recurring patterns up to a certain precision.

Wave packets can technically be seen as the superposition of infinitely many plane waves, all with different amplitudes and wavenumbers and frequencies, but each of those waves still has to fulfil the dispersion relation (5.5). Note that we fixed k, i.e. all solutions have the same horizontal wavenumber, which results in the wave packet being horizontally periodic. A way of constructing wave packets is to modulate a plane wave with an envelope function that has compact support or is at least rapidly decreasing. The question which arises is how the amplitude has to be distributed among the frequencies and wavenumbers in order to obtain a vertically confined wave packet. For a uniform stratification and wind, the answer can be obtained by a Fourier transform. However, in a background with non-uniform stratification and height-dependent wind, the wave parameters change during the propagation. Most notably, the vertical wave number distribution changes and the wave packet energy, which is proportional to the square of the amplitude, is shifted in wave number space. It is a priori not clear what the wave packet will look like after this change. The method that will be developed in this chapter finds a solution to this problem.

5.2 Uniform stratification

For uniform stratification $N \equiv N_0$, there is already well-established theory. Basically, the wave packet envelope moves with the vertical group velocity $\frac{\partial \omega}{\partial m}$ while it slowly disperses. For quasi-monochromatic wave packets, i.e. wave packets with an envelope much larger than the wavelength, the leading order influence on dispersion can be described by a linear Schrödinger equation. Details on this can for example be found in Sutherland (2010). Our interest, however, are wave packets in non-uniform media. Nonetheless, we are going to start the investigation with a view on uniform stratification. The results we obtain will be in line with the common literature, so that we can use the results as a cornerstone for the extension of the multi-layer method to wave packets in non-uniform media.

We start by modulating a plane wave with vertical wavenumber m_0 in physical space with a Gaussian function:

$$w(z,0) = \Re\left(\exp(-im_0 z)\exp\left(-\frac{z^2}{\sigma_z^2}\right)\right). \tag{5.7}$$

Without loss of generality, we choose the wave packet to be centred around $z = 0$. A common assumption is that the width σ_z of the wave packet is much larger than the vertical wavelength, i.e.

$$\frac{2\pi}{m_0} \ll \sigma_z. \tag{5.8}$$

These so-called quasi-monochromatic wave packets are the classical objects of study in WKB theory, since they allow for the definition of a local wave number and frequency whose scale of variation is much larger than the main wave length $\frac{2\pi}{m_0}$. We will also assume that equation (5.8) holds, but in fact, it is only necessary that $2\pi/m_0 \leq \sigma_z$. The wave packet then contains only a few vertical oscillations. Further, when we move to non-uniform background profiles, we are not restricted to a slowly varying stratification and wind when compared to the dominant wave length.

As the wave packet propagates, waves with larger wavelength will travel faster than shorter waves, as a result of the non-linear dispersion relation (5.5). Hence the wave packet will lose its initial shape. Moreover, non-uniform background will alter the shape as well.

Note that initial data of the shape (5.7) are only a special case. In general, atmospheric flow solvers can use a wide variety of wave packet initial data, but Gaussian wave packets are very convenient for use in idealized studies as they are smooth and analytically tractable in many ways. The method developed here is is applicable to initial conditions other than Gaussian, but we will showcase the method by the means of initial data of the form (5.7).

To link the amplitude modulation to wavenumbers and frequencies, we make use of the Fourier transform. We will not go into detail on this technique, but the interested reader might consult, e.g. Stein and Shakarchi (2003). The important part is that the Fourier transform exists for square-integrable functions, i.e. functions $f(z)$ with

$$\int_{\mathbb{R}} |f(z)|^2 \, \mathrm{d}z < \infty. \tag{5.9}$$

The space of all square-integrable functions is called L^2-space. The Fourier transform is the representation of such a function in the so-called phase space. It is defined as

$$F(f) = \widehat{f}(m) = \int_{\mathbb{R}} f(z) \exp(-imz) \, \mathrm{d}z \tag{5.10}$$

There is also the inverse transformation

$$F^*(\hat{f}) = f(z) = \frac{1}{2\pi} \int_{\mathbb{R}} \hat{f}(m) \exp(imz) \, \mathrm{d}m \tag{5.11}$$

with

$$F^*(F(f)) = f \text{ and } F(F^*(\hat{f})) = \hat{f}. \tag{5.12}$$

A feature of the Fourier transform is that a differentiation in physical space transfers to a multiplication in phase space, i.e.

$$\frac{\widehat{\mathrm{d}f}}{\mathrm{d}z}(z) = m\widehat{f}(m). \tag{5.13}$$

Moreover, constants do not affect the transformation, i.e.

$$\widehat{cf}(z) = c\widehat{f}(m). \tag{5.14}$$

Assuming a constant stratification $N \equiv N_0$ in equation (5.3) yields

$$\left(k^2 + \frac{\partial^2}{\partial z^2}\right) \frac{\partial^2 w}{\partial t^2} + N_0^2 k^2 w = 0. \tag{5.15}$$

Since none of the coefficients depends on z, we can Fourier transform this equation in z. Multiplying by $\exp(-imz)$ and integrating over z, using the above mentioned methods, yields

$$\frac{\partial^2 \widehat{w}}{\partial t^2}(m,t) + \frac{N_0^2 k^2}{k^2+m^2}\widehat{w}(m,t) = 0, \tag{5.16}$$

where

$$\widehat{w}(m,t) = \int_{\mathbb{R}} w(z,t)\exp(-imz)\,\mathrm{d}z. \tag{5.17}$$

This equation has the plane wave solution

$$\widehat{w}(m,t) = \Re\left(C(m)\exp\left(-i\omega(m)t\right) + D(m)\exp(i\omega(m)t)\right), \tag{5.18}$$

where

$$\omega(m) = \frac{N_0 k}{\sqrt{k^2+m^2}}, \tag{5.19}$$

$C(m)$ corresponds to the upward propagating wave component and $D(m)$ corresponds to the downward propagating wave component. Here, we only want an upward travelling wave packet, so $D(m) = 0$. In order to obtain $C(m)$ from the initial condition (5.7), we combine two different equations for $\widehat{w}(m,0)$. By evaluating equation (5.18) at $t = 0$, we find that

$$\widehat{w}(m,0) = C(m)\exp(-i\omega(m)\cdot 0) = C(m). \tag{5.20}$$

Moreover, evaluating equation (5.17) at $t = 0$ yields

$$\widehat{w}(m,0) = \int_{\mathbb{R}} w(z,0)\exp(-imz)\,\mathrm{d}z, \tag{5.21}$$

where the right-hand side can be seen as the Fourier transform of the initial condition (5.7). It basically corresponds to the wavenumber distribution of the Gaussian wave packet. So if we are able to compute the integral on the right-hand side of the above equation, we have the initial condition for equation (5.16). For a Gaussian wave packet, this can be done explicitly. First, we combine the exponentials:

$$\begin{aligned}\widehat{w}(m,0) &= \int_{\mathbb{R}} w(z,0)\exp(-imz)\,\mathrm{d}z \\ &= \int_{\mathbb{R}} \exp(-im_0 z)\exp\left(-\frac{z^2}{\sigma_z^2}\right)\exp(-imz)\,\mathrm{d}z \\ &= \int_{\mathbb{R}} \exp\left(-\frac{z^2}{\sigma_z^2} - i(m-m_0)z\right)\mathrm{d}z.\end{aligned} \tag{5.22}$$

The argument of the exp-function can be understood as an incomplete square:

$$\begin{aligned}(5.22) &= \int_{\mathbb{R}} \exp\left(-\frac{z^2}{\sigma_z^2} - i(m-m_0)z - i^2\sigma_z^2\frac{(m-m_0)^2}{4}\right)\exp\left(i^2\sigma_z^2\frac{(m-m_0)^2}{4}\right)\mathrm{d}z \\ &= \exp\left(-\frac{1}{4}\sigma_z^2(m-m_0)^2\right)\int_{\mathbb{R}}\exp\left(-\left(\frac{z}{\sigma_z}+i\sigma_z\frac{m-m_0}{2}\right)^2\right)\mathrm{d}z \\ &= \exp\left(-\frac{1}{4}\sigma_z^2(m-m_0)^2\right)\sqrt{\pi\sigma_z^2}.\end{aligned} \tag{5.23}$$

For the last equality, we used the well-known value of the integral of the Gaussian function (Forster, 2012)

$$\int_{\mathbb{R}} \exp\left(-\frac{(x-x_0)^2}{c^2}\right)\mathrm{d}x = \sqrt{\pi c^2}, \tag{5.24}$$

assuming $c \in \mathbb{R}$ and $x_0 \in \mathbb{C}$. We see that the Fourier transform of the Gaussian wave packet is a Gaussian function. Observe that it is centred around m_0, the main wavenumber of the wave packet, and that the width is $2/\sigma_z$, which is, in case of a quasi-monochromatic wave packet, much smaller than m_0 (this fact is derived from equation (5.8)). So the wave packet contains only wavenumbers that lie in a small area around m_0.[1]

If we allow for σ_z only slightly larger than λ_z, the Gaussian shape of $\widehat{w}(m,0)$ would be very broad, so that more waves actually contribute to the shape of the wave packet. Our approach is applicable to this situation without restriction but, as we are going to approximate wave packets by a finite superposition of plane waves, our method is particularly efficient for the approximation of quasi-monochromatic wave packets.

The solution to equation (5.16) with initial condition obtained by Fourier transforming equation (5.7) is

$$\widehat{w}(m,t) = \sqrt{\pi\sigma^2}\exp\left(-\frac{1}{4}\sigma^2(m-m_0)^2\right)\exp\left(-i\omega(m)t\right). \tag{5.25}$$

In order to obtain the solution in physical space, we have to apply the inverse Fourier

---

[1] Technically, the wave packet contains all wavenumbers since $\widehat{w}(m,0)$ is always non-zero, but the contributions of waves with wavenumbers that are outside a small neighbourhood of m_0 are negligible, since their amplitude is very small.

transform to equation (5.25):

$$\begin{aligned} w(z,t) &= \frac{1}{2\pi}\int_{\mathbb{R}} \widehat{w}(m,t)\exp(imz)\,\mathrm{d}m \\ &= \frac{1}{2\pi}\int_{\mathbb{R}} C(m)\exp(-i\omega(m)t)\exp(imz)\,\mathrm{d}m \\ &= \frac{1}{2\pi}\int_{\mathbb{R}} \sqrt{\pi\sigma^2}\exp\left(-\frac{1}{4}\sigma^2(m-m_0)^2\right)\exp(-i\omega(m)t)\exp(imz)\,\mathrm{d}m \end{aligned} \tag{5.26}$$

Unfortunately, this can not be evaluated explicitly, but numerically, as the actual integration domain is a small interval $I_{m_0} = [m_0 - \varDelta_m, m_0 + \varDelta_m]$, with $\varDelta_m$ chosen appropriately such that $m_0 + \varDelta_m < 0$ and wavenumbers outside I_{m_0} have a negligible amplitude. By performing this integration for several values of z and t, we obtain a wave packet that has downward travelling phases with an upward moving envelope that slowly disperses in time, just as we expected. The results are displayed in figure 5.1,

We initialised a wave packet with horizontal wavelength $\lambda_x = 30\,\mathrm{km}$, main vertical wave length $\lambda_{z,0} = 3\,\mathrm{km}$ and an envelope width $\sigma_z = 7\,\mathrm{km}$ for the upper row and $\sigma_z = 3\,\mathrm{km}$ for the lower row. We observe that the dispersion for the second case, where $\sigma_z = \lambda_{z,0}$, the initial wave packet contains only a few oscillations, is much smaller, but it disperses much stronger. This is because the wave number distribution is broader and hence, much longer waves contribute to the wave packet which have in turn a much higher vertical group velocity, given by $\partial\omega/\partial m$.

It is interesting to note that a numeric evaluation of the integral in equation (5.26), for example via composite Newten-Côtes formulae, corresponds to an approximation of the wave packet by a superposition of finitely many plane waves. To see this, we look at a quadrature formula for a fixed location z_0 and time t_0

$$w(z_0,t_0) = \int_{I_{m_0}} \widehat{w}(m,t_0)\exp(imz_0)\,\mathrm{d}m \approx |I_{m_0}|\sum_{l=1}^{n}\psi_l\widehat{w}(m_l,t_0)\exp(imz_0) \tag{5.27}$$

with weights ψ_l at wavenumbers m_l . As we said in the beginning of this section, for a fixed wavenumber, in this case m_l, the solution $\widehat{w}(m_l,t)$ has a plane wave structure. Therefore, the quadrature formula can be seen as a weighted superposition of finitely many plane waves that approximate the wave packet. This will be of great avail later.

If we have a look at equation (5.15) again, we see that the coefficients also do not depend on t, so the Fourier transform should also work with t instead of z, i.e.

$$\widetilde{w}(z,\omega) = \int_{\mathbb{R}} w(z,t)\exp(-i\omega t)\,\mathrm{d}t. \tag{5.28}$$

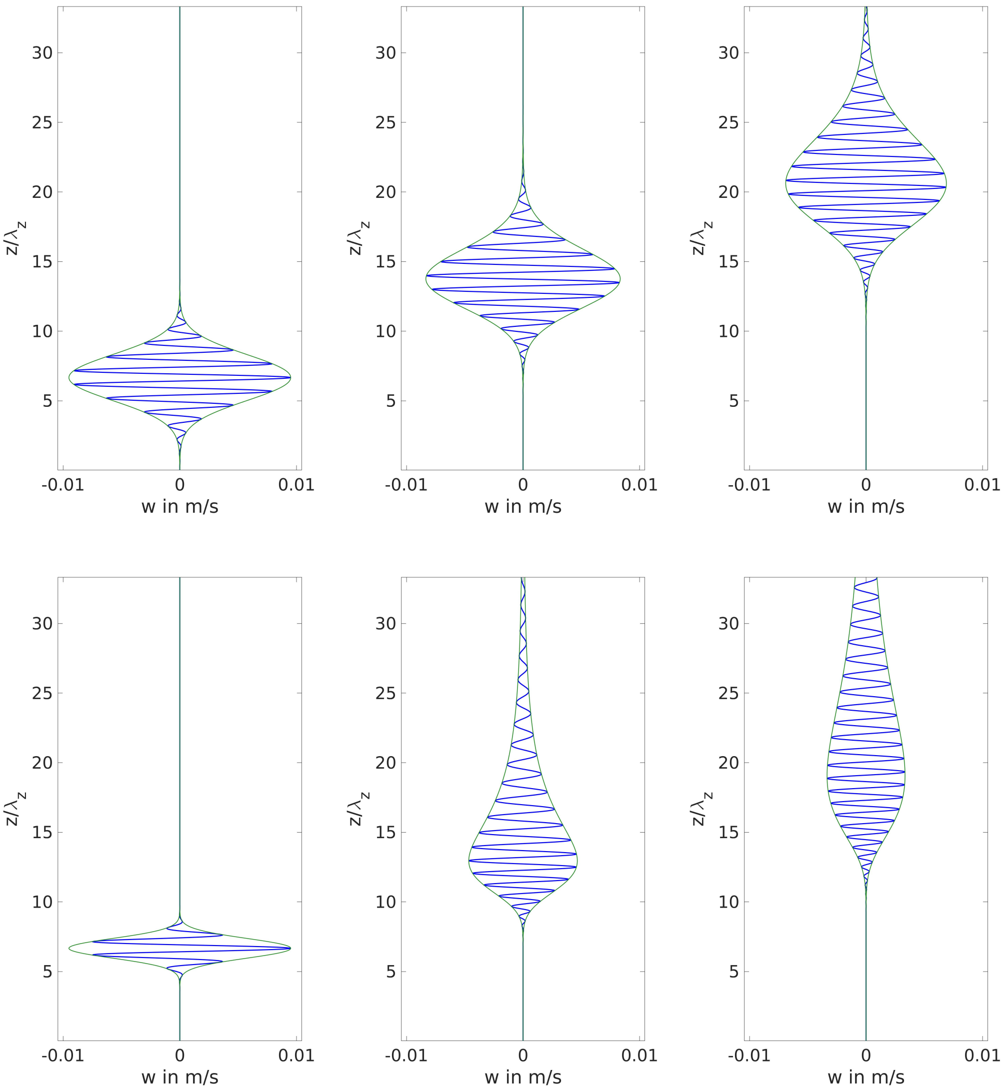

Figure 5.1: Snapshots an upward travelling Gaussian wave packet in uniform background $N \equiv N_0$ at different time points, computed with the multi-layer method. The left panel displays the initialised packet, the middle panel shows it after $tN_0 = 450$ and the right panels after $tN_0 = 900$. The blue curve is the wave packet itself, the green line is the envelope, plotted here to see the effect of the dispersion better. The wave packet broadens, with longer waves travelling faster than shorter ones. The wave amplitude is 1% of the static instability threshold ω_0^2/m_0, which was estimated by Achatz et al. (2010).

The resulting equation is

$$\frac{\partial^2 \widetilde{w}}{\partial z^2}(z,\omega) + \underbrace{k^2 \left(\frac{N_0^2}{\omega^2} - 1\right)}_{=:m(\omega)^2} \widetilde{w}(z,\omega) = 0. \tag{5.29}$$

In case of uniform stratification, we also have plane wave solutions

$$\widetilde{w}(z,\omega) = \Re(A(\omega)\exp(im(\omega)z) + B(\omega)\exp(-im(\omega)z)). \tag{5.30}$$

Again, if we want to initialise an upward propagating wave packet, we have to choose $B(\omega) = 0$. By using the inverse Fourier transform, we obtain the full solution in physical space and time:

$$w(z,t) = \frac{1}{2\pi}\int_{\mathbb{R}} \widehat{w}(z,\omega)\exp(i\omega t)\,\mathrm{d}\omega = \frac{1}{2\pi}\int_{\mathbb{R}} A(\omega)\exp(-im(\omega)z)\exp(i\omega t)\,\mathrm{d}\omega. \tag{5.31}$$

It is important to say that the integration domain is not $\mathbb{R}$, but the interval $(0, N_b)$ for two reasons. The first reason is that we assumed $\omega > 0$, as negative frequencies are ruled out by symmetry. The second is that waves with frequencies $\omega \geq N_b$ are evanescent in the troposphere and are assumed not to reach the tropopause[2]. Unfortunately, there is no direct way of using the initial condition $w(z, 0)$ to determine $A(\omega)$, since we transformed the time dependency into a frequency dependency. We would need a boundary condition $w(z_0, t)$, i.e. what an observer would see over all times at a fixed point z_0 in space. But since the phase velocity is negative while the group velocity is positive, it is a priori not clear if an initial Gaussian-shaped wave packet in space also produces a Gaussian-shaped packet in time. There is, however, a link between wavenumber and frequency, namely the dispersion relation (3.9). We can use it to apply a coordinate transformation in equation (5.26) from m to ω, where

$$m = m(\omega) = -k\sqrt{\frac{N^2}{\omega^2} - 1}. \tag{5.32}$$

Then, the integrand of equation (5.26) takes the shape of the integrand of equation (5.31). Hence, it will be possible to find $A(\omega)$, which then corresponds to the correct starting conditions for a Gaussian gravity wave packet in frequency space. To perform

---

[2] They might actually reach the tropopause, if their vertical wavelength is very large, similar to the tunnelling effect we saw in subsection 3.6.2, but we will focus on wave packets that propagate properly through the troposphere.

the transformation, we use

$$\mathrm{d}m = \frac{\mathrm{d}m}{\mathrm{d}\omega}\,\mathrm{d}\omega = \frac{N^2 k}{\omega^3\sqrt{\frac{N^2}{\omega^2}-1}}\,\mathrm{d}\omega. \tag{5.33}$$

We also have to make sure that the integration boundaries are correct. We know that the integration bounds for the inverse Fourier Transform in ω need to be 0 and N_b, hence the bounds before the coordinate transformation are $m(0) = -\infty$ and $m(N_b) = 0$. As we mentioned earlier in this section, only wavenumbers in I_{m_0}, i.e. close to m_0, actually contribute to the wave packet. Moreover, I_{m_0} was constructed to be contained in the negative real numbers. Hence the integration bounds are fine for the coordinate transformation. We obtain

$$\begin{aligned} w(z,t) &= \frac{1}{2\pi}\int_{-\infty}^{0} C(m)\exp\left(-i\omega(m)t\right)\exp\left(imz\right)\mathrm{d}m \\ &= \frac{1}{2\pi}\int_{0}^{N_b} C(m(\omega))\exp\left(-i\omega t\right)\exp\left(im(\omega)z\right)\frac{\mathrm{d}m}{\mathrm{d}\omega}\,\mathrm{d}\omega \\ &= \frac{1}{2\pi}\int_{0}^{N_b} A(\omega)\exp\left(-im(\omega)z\right)\exp\left(-i\omega t\right)\mathrm{d}\omega \end{aligned} \tag{5.34}$$

with

$$A(\omega) = \sqrt{\pi\sigma^2}\exp\left(-\frac{1}{4}\sigma^2\left(-k\sqrt{\frac{N^2}{\omega^2}-1}-m_0\right)^2\right)\frac{N^2 k}{\omega^3\sqrt{\frac{N^2}{\omega^2}-1}} \tag{5.35}$$

This is the correct starting condition for a gravity wave packet in frequency space which is initialised with a Gaussian shape in real space.

With this representation of Gaussian wave packets in frequency space, we will be able to extend the multi-layer method from chapter 3 to describe the evolution of a wave packet, while still being able to set up numerical simulations that take Gaussian wave packets as initial conditions. As long as we are able to explicitly compute the spatial Fourier transform of the initial wave packet, we are able to create a starting condition in frequency space. Hence it is also possible to show the evolution of, e.g., cosine-shaped wave packets, which were studied by Bölöni et al. (2016) in different atmospheric circumstances. They will be in fact the object of study in section 6.3, where we validate the theory numerically.

5.3 Non-uniform stratification

One could ask why it is important to translate wave packet-like initial conditions to frequency space when a transformation to wavenumber space also works and seems much more natural. The reason for this is that in case of non-uniform stratification, i.e. $N = N(z)$, we are not able to perform a Fourier transform in z of equation (5.3), since now the equation explicitly depends on z. But a Fourier transform in t is still possible, which yields equation (5.29) with the difference that N now depends on z. Similar to equation (3.7) for plane waves, it can, in general, not be solved explicitly for arbitrary stratification profiles. What we can do now is to use the method we developed for plane waves in chapter 3, i.e. approximating $N(z)$ by a piecewise constant function. We obtain local solutions that are valid in the layers where N is constant. Following the notations in chapter 3, we have equations

$$\frac{\partial^2 \widetilde{w}_j}{\partial z^2}(z,\omega) + k^2 \left(\frac{N_j^2}{\omega^2} - 1 \right) \widetilde{w}_j(z,\omega) = 0, \tag{5.36}$$

for $j = 1, \dots, J+1$. Similar to equation (5.18), we have plane wave solutions

$$\widetilde{w}_j(z,\omega) = A_j(\omega) \exp(-i m_j(\omega) z) + B_j(\omega) \exp(i m_j(\omega) z), \tag{5.37}$$

where again A_j corresponds to the upward propagating part and B_j to the downward propagating one, j indicates the corresponding layer and

$$m_j(\omega) = -k \sqrt{\frac{N_j^2}{\omega^2} - 1}. \tag{5.38}$$

Together with the matching conditions (3.21), we can derive relations

$$\begin{pmatrix} A_j \\ B_j \end{pmatrix} = \begin{pmatrix} q_{11}^{(j)} & q_{12}^{(j)} \\ q_{21}^{(j)} & q_{22}^{(j)} \end{pmatrix} \begin{pmatrix} A_{j+1} \\ B_{j+1} \end{pmatrix}. \tag{5.39}$$

similar to equation (3.24). Note that the matrix here is the inverse of (3.27). The matrix entries can however easily be derived with the matrix entries of the original matrix (3.28) and (3.29), the determinant (3.30) and the matrix inversion formula for 2-by-2 matrices

$$\begin{pmatrix} a & b \\ c & d \end{pmatrix}^{-1} = \frac{1}{ad - bc} \begin{pmatrix} d & -b \\ -c & a \end{pmatrix}. \tag{5.40}$$

Note that m_j and m_{j+1} are now functions of ω, as displayed in equation (5.38). The reason why we decide to use this direction for the matching is rather simple, as it is easier to handle during the upcoming transformations and optimises computation time.

But still, the multi-layer method is not yet applicable, since there is a major difference to the case with plane waves. When looking at a single plane wave with fixed wavenumber and frequency, then requiring that we have only upward propagating waves above a region of non-uniform stratification is the same as saying we initially have only upward propagating waves below the non-uniform stratification that are incident on this region, since we eventually get a steady state. But now we have an explicit temporal dependence of the solution and when initialising a single Gaussian wave packet below a region of non-uniform stratification is not guaranteed to yield a single wave packet above the region, let alone Gaussian-shaped. It could and will be that some partial reflected part of the wave packet is again reflected inside this region, causing the double reflected part to travel upwards again so that the wave packet has some sort of a “tail” or that we have multiple distinguishable wave packets.

Therefore, we are not able to provide the amplitude information for upward and downward propagating waves in the uppermost layer, which would let us solve equation (5.39) recursively for all j. So the correct approach is to require no downward travelling wave packets in the upper layer and only a single upward travelling wave packet in the lowest layer. Hence, we choose $A_1(\omega)$ in a way that it corresponds to a wave packet, for example via equation (5.35) and we require $B_{J+1}(\omega) = 0$.

We can gather the conditions at all interfaces in a large equation system:

$$\begin{pmatrix} 1 & 0 & -q_{11}^{(1)} & -q_{12}^{(1)} & 0 & 0 & \dots & 0 & 0 & 0 & 0 \\ 0 & 1 & -q_{21}^{(1)} & -q_{22}^{(1)} & 0 & 0 & \dots & 0 & 0 & 0 & 0 \\ 0 & 0 & 1 & 0 & -q_{11}^{(2)} & -q_{12}^{(2)} & \dots & 0 & 0 & 0 & 0 \\ 0 & 0 & 0 & 1 & -q_{21}^{(2)} & -q_{22}^{(2)} & \dots & 0 & 0 & 0 & 0 \\ \vdots & \vdots & \vdots & \vdots & \vdots & \vdots & \vdots & \vdots & \vdots & \vdots & \vdots \\ 0 & 0 & 0 & 0 & 0 & 0 & \dots & 1 & 0 & -q_{11}^{(J)} & -q_{12}^{(J)} \\ 0 & 0 & 0 & 0 & 0 & 0 & \dots & 0 & 1 & -q_{21}^{(J)} & -q_{22}^{(J)} \end{pmatrix} \begin{pmatrix} A_1 \\ B_1 \\ A_2 \\ B_2 \\ \vdots \\ A_{J+1} \\ B_{J+1} \end{pmatrix} = 0 \qquad (5.41)$$

The matrix has a size of $2J \times (2J + 2)$, so we have $2J$ equations for the $2J + 2$ amplitudes. But we already know two of them, namely A_1 and B_{J+1}, so we actually have only $2J$ unknown amplitudes. So the equation system that we need to solve is

$$\begin{pmatrix} 0 & -q_{11}^{(1)} & -q_{12}^{(1)} & 0 & 0 & \dots & 0 & 0 & 0 \\ 1 & -q_{21}^{(1)} & -q_{22}^{(1)} & 0 & 0 & \dots & 0 & 0 & 0 \\ 0 & 1 & 0 & -q_{11}^{(2)} & -q_{12}^{(2)} & \dots & 0 & 0 & 0 \\ 0 & 0 & 1 & -q_{21}^{(2)} & -q_{22}^{(2)} & \dots & 0 & 0 & 0 \\ \vdots & \vdots & \vdots & \vdots & \vdots & \vdots & \vdots & \vdots & \vdots \\ 0 & 0 & 0 & 0 & 0 & \dots & 1 & 0 & -q_{11}^{(J)} \\ 0 & 0 & 0 & 0 & 0 & \dots & 0 & 1 & -q_{21}^{(J)} \end{pmatrix} \begin{pmatrix} B_1 \\ A_2 \\ B_2 \\ A_3 \\ \vdots \\ B_{n-1} \\ A_n \end{pmatrix} = \begin{pmatrix} -A_1 \\ 0 \\ 0 \\ 0 \\ \vdots \\ 0 \\ 0 \end{pmatrix} \qquad (5.42)$$

In general, the matrix in equation (5.42) has maximal rank, unless the first row or last column is zero, but this can happen only if the matrices in equation (5.39) for $j = 1$ or $j = J$ are defect. As we can derive from equation (3.30), this only happens if $m_2 = 0$

or $m_{J+1} = 0$. The second case can be ruled out as it would correspond to a neutrally stratified stratosphere, not allowing for wave propagation. Although that case is allowed theoretically, it is not of particular interest, as all the transmission coefficients would be 0, resulting in a total reflection. The first case however might appear. But as we discussed already in section 3.2, we avoid evaluating at points that cause the vertical wavenumber to vanish, supposed it occurs at an isolated point in space. Therefore, the linear equation system (5.42) can be assumed to have full rank and by solving it, we find a unique solution.

Theoretically, it is possible to use the matrix structure to write down the solution in a closed formula, but the computation of this approach is very costly, since the matrix entries are in fact functions depending on ω and the equation system needs to be solved symbolically. Due to this fact, it was not manageable to compute the closed formula, even for a small number of layers.

Therefore, we had to develop another way of finding the solution. Even if we would find the analytic solution, we expect that we can evaluate the integral that appears in the inverse Fourier transform only numerically. This would correspond to an approximation of the wave packet by a superposition of finitely many plane waves, as we already pointed out in section 5.2. Hence, it seems convenient to take certain values for ω at which the corresponding functions are evaluated and the resulting linear equation system is solved numerically. These values will then serve as grid points for the numeric approximation of the inverse Fourier transform.

In order to get accurate results, we describe the wave packet as a superposition of several thousands of plane waves. By what we said at the beginning of this chapter, such a superposition is almost-periodic in space and time, but the almost-periods for reasonably small ε are much larger than the temporal and spatial envelope, so that the wave packets do not influence each other in the region of interest.

The transmission coefficient is computed as a weighted sum, where each plane wave contributes as much as its fraction of the initial wave energy. To be precise, this writes down as

$$TC_{total} = \sum_{\omega} \frac{A_1(\omega)^2}{\sum_{\omega'} A_1(\omega')^2} TC(\omega), \tag{5.43}$$

where the sum runs over all frequencies at which we evaluate and with the usual formula for the transmission coefficient

$$TC(\omega) = \frac{m_{J+1}(\omega)}{m_1(\omega)} \left| \frac{A_{J+1}(\omega)}{A_1(\omega)} \right|^2 \tag{5.44}$$

that we already know from section 3.3.

Table 5.1 shows the comparison of some calculations for several wave packets in different stratification profiles and their plane wave counterparts, i.e., plane waves with the

$\lambda_z/d_{\mathrm{TP}}$	0.4	1	2	5	case
realistic TP	0.9673	0.8092	0.6616	0.4184	Wave packet
	0.9668	0.8095	0.6620	0.4189	Plane wave
Reflection	0.9764	0.2904	0.0916	0.0298	Wave packet
	0.9791	0.2873	0.0916	0.0299	Plane wave

Table 5.1: As stratification, we use the realistic tropopause and the reflection layer profiles from Pütz et al. (2018). The tropopause depth is $d_{\mathrm{TP}} = 1000\,\mathrm{m}$, $\lambda_x = 2000\,\mathrm{m}$ and $\sigma_z = 5\lambda_z$ in all cases. We find that the energy transmission of Gaussian wave packets can very well be approximated by plane waves with vertical wave number equal to the main wave number of the packet.

same horizontal wave number and the main frequency ω_0:

$$\omega_0 = \frac{N_0 k}{\sqrt{k^2 + m_0^2}}. \tag{5.45}$$

We fixed the horizontal wave length to be $\lambda_x = 2000\,\mathrm{m}$ and the tropopause depth was set to be $d_{\mathrm{TP}} = 1000\,\mathrm{m}$. We chose to display the main vertical wavelength instead of the frequency, because it gives a better intuition about how large the wave packet is compared to the region of non-uniform stratification. We make an interesting observation. The transmission of the wave packets can be described very well by just using the transmission coefficient for the corresponding plane wave. This permits a very fast and efficient estimate of partial reflection and transmission of gravity wave packets incident on a region of non-uniform stratification.

5.4 Evolution of wave packets

The transmission coefficient gives a measure for how much wave energy propagated through the tropopause. What we do not know is how the transmitted and reflected wave packet look like. Fortunately, this approach gives the possibility to compute the full spatial and temporal evolution of the initialised gravity wave packet. In order to do this, we need to calculate the inverse Fourier transform of the solution we obtain from the multi-layer method. We recall that

$$w(z,t) = \frac{1}{2\pi} \int_0^{N_b} \widetilde{w}(z,\omega) \exp(-i\omega t)\,\mathrm{d}\omega, \tag{5.46}$$

where $\widetilde{w}$ is the piecewise defined function

$$\widetilde{w}(z,\omega) = A_j(\omega) \exp(-im(\omega)z) + B_j(\omega) \exp(im(\omega)z), \quad z \in I_j \tag{5.47}$$

for $j = 1, \ldots, J+1$. As we already mentioned in sections 5.2 and 5.3, the integral will be approximated by a quadrature formula

$$\int_0^{N_b} \widetilde{w}(z,\omega) \exp\left(-i\omega t\right) \mathrm{d}\omega = N_b \sum_{l=1}^{n} \psi_l \widetilde{w}(z,\omega_l) \tag{5.48}$$

with weights ψ_l. Let $\Omega = \{\omega \mid |\omega - \omega_0| \leq \Delta_\omega\}$ where ω_0 is the main frequency of the wave packet and Δ_ω be chosen appropriately such that $A_1(\omega)$ is small compared to $\max_{\omega' \in (0,N_b)} |A_1(\omega')|$ for all ω with $|\omega - \omega_0| > \Delta_\omega$, i.e. waves with frequencies outside of Ω contribute negligibly to the wave packet. Let n_ω be a positive integer. Define $\omega_l = \omega_h + \frac{l}{n_\omega}\Delta_\omega$ for $l = -n_\omega, \ldots n_\omega$ and set $\Omega^\sharp = \{\omega_l \mid l = -n_\omega \ldots n_\omega\}$. Assume that we have solved equation system (5.42) for every $\omega_l \in \Omega^\sharp$, i.e we have the amplitudes $A_j(\omega_l), B_j(\omega_l)$, where j indicates the layer. Given that we already have an equidistant grid on $\Omega^\sharp$, the most natural choice is a composite Newton-Côtes formula.

As we have $2n_\omega + 1$ grid points, it is possible to use the composite Simpson rule (which is for example also used in the MATLAB built-in integrator *quad*). We split up the integral in a sum of smaller integrals, which then are individually solved by the Simpson rule. To be precise, the integral in equation (5.46) written as

$$\int_\Omega \widetilde{w}(z,\omega) \exp\left(-i\omega t\right) \mathrm{d}\omega = \sum_{l=1}^{n_\omega} \int_{\omega_{2(l-1)-n_\omega}}^{\omega_{2l-n_\omega}} \widetilde{w}(z,\omega) \exp\left(-i\omega t\right) \mathrm{d}\omega. \tag{5.49}$$

Each integral is then approximated by

$$\begin{aligned} &\int_{\omega_{2(l-1)-n_\omega}}^{\omega_{2l-n_\omega}} \widetilde{w}(z,\omega) \exp\left(-i\omega t\right) \mathrm{d}\omega \\ &\qquad\qquad \approx \frac{2\Delta_\omega}{6n_\omega} \left(I(\omega_{2(l-1)-n_\omega}) + 4I(\omega_{2(l-1)-n_\omega+1}) + I(\omega_{2l-n_\omega}) \right), \end{aligned} \tag{5.50}$$

where

$$I(\omega_l) = \left(A_j(\omega_l) \exp\left(-im_j(\omega_l)z\right) + B_j(\omega_l) \exp\left(im_j(\omega_l)z\right)\right) \exp\left(-i\omega_l t\right). \tag{5.51}$$

The index j depends on the evaluated point z. To be precise, we choose the unique j such that $z \in I_j$, where we use the definition of I_j from subsection 3.2. Defining $h_\omega = \Delta_\omega / n_\omega$, the full solution is then approximated by

$$w(z,t) \approx \frac{1}{2\pi} \frac{h_\omega}{3} \sum_{l=1}^{n_\omega} I(\omega_{2(l-1)-n_\omega}) + 4I(\omega_{2(l-1)-n_\omega+1}) + I(\omega_{2(l-1)-n_\omega+2}), \tag{5.52}$$

Performing this calculation for a fixed discrete vertical domain D and several discrete time steps $\{t_s\}_{s=1}^{n_t}$, we obtain a temporal evolution of the gravity wave packet in the domain D.

One major advantage over the use of numerical flow solvers is that we can construct an approximate solution for the whole space and all times. We can just pick any time t_0 and display the solution in an area we are interested in rather than initialising a wave packet and simulating up to t_0. Of course the method describes just the linear behaviour of the wave packet in a Boussinesq setup, but it is nonetheless an interesting result that gives a good qualitative hint of how gravity wave packets behave in certain stratification profiles. As we will see in section 6.3, the results derived here match up very well against simulations of small-amplitude wave packets with the full non-linear Boussinesq equations.

We shall discuss another method to approximate the integral in equation (5.46). One could make the argument that, given the solutions $\widetilde{w}(z, \omega_l)$, one could simply superimpose $I(\omega_l)$ to obtain a solution depending on z and t. While this is a feasible approach, the solutions have to be scaled by a factor that accounts for the number of waves we superimpose in order to obtain the correct physical solution. Sticking to the notation from above, it turns out that this factor is $h_\omega/(2\pi)$, so that we can approximate the solution as

$$w(z,t) \approx \frac{h_\omega}{2\pi} \sum_{l=-n\omega}^{n_\omega} I(\omega_l). \tag{5.53}$$

A closer inspection of this approximation reveals that it is actually a Riemann sum for solving the integral in equation (5.46). Hence, the simple superposition of plane waves also corresponds to an approximation of the inverse Fourier transform.

We tested both methods for several test cases and it turned out that both are equally fine. The theory predicts both methods to converge to the real value of the integral with the composite Simpson rule doing so faster. The difference can be seen when using only a few plane waves, but for the computations we did, the number of plane waves was at least 1000. The error between both methods then was on the order of machine precision, so none of them could be declared superior over the other in terms of accuracy. Nonetheless, the Riemann approach has the advantage of being easier to implement and is therefore computationally cheaper. The saving in computational time is on the order of a few percent. While this does not seem much (in fact, the method is still very efficient when running with the composite Simpson rule), it will allow us to extend the method to wave packets that are horizontally and vertically localised. This will be briefly discussed in section 5.6. All computations presented in here were carried out with the composite Simpson rule.

In figure 5.2 we show vertical cuts through a wave packet that propagates through the realistic tropopause profile (3.111) with the same specifications as in section 3.6. We used $\varDelta_z = 1000\,\mathrm{m}$ and wavelengths $\lambda_x = \lambda_z = 2000\,\mathrm{m}$ at time points $t = 0\,\mathrm{h}, 2.5\,\mathrm{h}, \ldots, 12.5\,\mathrm{h}$. We can observe a partial reflection at the region of non-uniform stratification. In the upper right panel, the partial reflection is about to take place, which is indicated by the strong oscillations of the envelope. In the lower panels, we can detect two separated wave packets, travelling in different directions. In this particular case, the wave packet more or less keeps its shape: both the reflected and transmitted packet do look Gaussian-like. It is not possible to give an explicit formula for the envelope, though. The transmission coefficient is 0.6616. Although the amplitude in the stratosphere seems to be slightly smaller, the stratospheric wave packet contains more energy as we assumed a stronger stratification there than in the troposphere. Hence, the vertical wavenumber is larger and the amplitude smaller for wave packets with the same energy (it scales with the square of vertical wavenumber ratio).

Figure 5.3 shows the propagation of the same gravity wave packet through the twin peaks profile (3.112) with $d = 10L$. What happens here is that a part of the wave is transmitted through the first peak as well as thorough the second peak. The part that is reflected at the second peak is then incident again on the first peak, but from above, causing again a partial reflection and transmission of the wave packet so that there is again an upward travelling wave packet, which has smaller amplitude than the first transmitted packet and which is located at a different point in space. In the upper right panel, the partial reflection at the first peak is finished and the wave packet is at the second peak. In the lower left panel, one can see the second downward travelling packet as well as the transmitted packet. In the lower middle and right panel, one can see a second upward travelling packet, which corresponds to a reflection of the second downward packet at the first peak. This is a case where the method really shines. Not only yields the computation of the transmission coefficients for the initial wave packet and the corresponding plane wave slightly different values (0.8246 for the wave packet versus 0.7394 for the corresponding plane wave), it is the visualisation of the evolution of the wave packet that tells us that the transmitted as well as the reflected wave energy is split between multiple distinguishable wave packets.

5.5 Wave packets with wind

We are now able to describe the propagation of gravity waves through a non-uniform, but steady background. This is already quite an achievement as such an approximate solution, to the best of the authors' knowledge, was never derived before. But for real atmospheric applications, height-dependent background wind is an important factor and this is why we are going to extend the theory even further to account for a non-steady background. In order to do this, we combine the discoveries from chapter 4 and the current chapter.

As it turns out, both extensions are straight-forward to combine, as the plane-wave solution with and without wind works almost identical, with the difference of absolute frequency replaced by relative frequency and the additional curvature term in the equation. Basically the same is true for wave packets. The equation we want to solve is

$$\frac{\partial^2 \hat{w}}{\partial z^2}(z,\omega) + k^2 \left(\frac{N(z)^2}{(\omega - k\overline{u}(z))^2} + \frac{\overline{u}''(z)}{k(\omega - k\overline{u}(z))} - 1 \right) \hat{w}(z,\omega) = 0, \tag{5.54}$$

which will be done in a similar way as we did for no background wind. We approximate N, $\overline{u}$ and $\overline{u''}$ in the same way as in chapter 4 and the ω-dependency will be dealt with as we did in section 5.3 by evaluating the equation for fixed values of ω and solving the corresponding linear equation system numerically. The last missing ingredient is the transformation of the initial wave packet to a starting condition in Fourier space.

Recall that the dispersion relation for the vertical wavenumber with background wind is

$$m = -k\sqrt{\frac{N^2}{(\omega - k\overline{u})^2} + \frac{\overline{u}''}{k(\omega - k\overline{u})} - 1}. \tag{5.55}$$

Hence, its derivative after the absolute frequency yields

$$\frac{\mathrm{d}m}{\mathrm{d}\omega} = \frac{k}{2\sqrt{\frac{N^2}{(\omega - k\overline{u})^2} - 1}} \left(\frac{2N^2}{(\omega - k\overline{u})^3} + \frac{\overline{u}''}{k(\omega - k\overline{u})^2} \right). \tag{5.56}$$

Therefore, we obtain for the starting condition the expression

$$\sqrt{\pi\sigma^2} \exp\left(-\frac{1}{4}\sigma^2 \left(-k\sqrt{\frac{N^2}{\hat{\omega}^2} + \frac{\overline{u}''}{k\hat{\omega}^2} - 1} - m_0 \right)^2 \right) \frac{k\left(\frac{2N^2}{\hat{\omega}^3} + \frac{\overline{u}''}{\hat{\omega}^2}\right)}{2\sqrt{\frac{N^2}{\hat{\omega}^2} - 1}}, \tag{5.57}$$

where $\hat{\omega} = \omega - k\overline{u}$. So basically, the absolute frequency was replaced by the relative frequency and the additional term coming from the curvature occurs. Apart from these small changes, we can apply the method as derived in section 5.3 and also compute the full spatio-temporal evolution, analogous to section 6.3.

With this point reached, we developed a very strong and versatile method that describes the evolution of small-amplitude gravity wave packets under arbitrary background conditions. Moreover, it provides the solution for any given point in time when given an initial condition. This is a huge advantage over numerical simulations, which have to integrate the governing equations step by step to eventually reach a time point of interest. To be a serious contender for WKB ray tracer, an extension to higher dimensions (at least two-dimensional) must be done. This is discussed briefly in the forthcoming section. Moreover, we do not know by now how well the solutions obtained from the multi-layer method match against numerical simulations of the full non-linear Boussinesq equations. This is a task that will be taken on in chapter 6.

5.6 Two-dimensional wave packets

We will close this chapter with a few comments on two-dimensional wave packets, as the methods we developed throughout this chapter will also work for them. Assume we have an initial condition

$$w(x,z,0) = f(x)g(z) \tag{5.58}$$

for equation (3.5), then a Fourier transform in x would give equation (5.3), but with k as an independent variable. The initial condition can than be transferred to this equation and reads

$$\widetilde{w}(k,z,0) = \widetilde{f}(k)g(z), \tag{5.59}$$

where $\widetilde{f}$ corresponds to the Fourier transform of f. From this point on, we can go the same route as for 1D wave packets, but we are not only superimposing waves with different frequencies but also with different horizontal wavenumbers. Nevertheless, it is possible to compute the full spatio-temporal evolution of a 2D wave packet with this method. The inverse Fourier transform however now also needs to be done for a horizontal domain D_x, effectively increasing the number of computation steps by a factor of $|D_x|$. Moreover, since the inverse Fourier transform is now a double integral, the number of waves we use in the horizontal direction is also a factor that increases the computation steps, since for every wavenumber k_j, we have to compute a Fourier integral in the sense of section 5.4 before eventually computing the second integral, also with a quadrature rule. If we use the composed Simpson rule for both integrals, we obtain a massive increase in computation time, effectively losing the advantage of a fast computation that we have in the 1D-case.

However, if we use the Riemann sum approach for both integrals like in equation (5.53), it is possible to increase the efficiency of the computation such that we can find results reasonably fast. For reference, a test case with 100 values for both k and ω took with the Simpson rule approximately one hour to compute a time point in a domain with 301 horizontal and 501 vertical grid points. In the same setup, the Riemann sum approach only needed 30 seconds to give a result. The reason for the faster computation is that in the Riemann sum, every grid point has the same weight (unlike the Simpson rule, where the middle point has a weight of $2/3$ compared to $1/6$ at the end points). This allows us to solve both integrals by only one summation. Moreover, we can perform the summation for all x-values at the same time.

Another solution could be to implement a splitting ansatz, where we use the multilayer approach in the vertical and a numerical method in the horizontal, but this is an open problem.

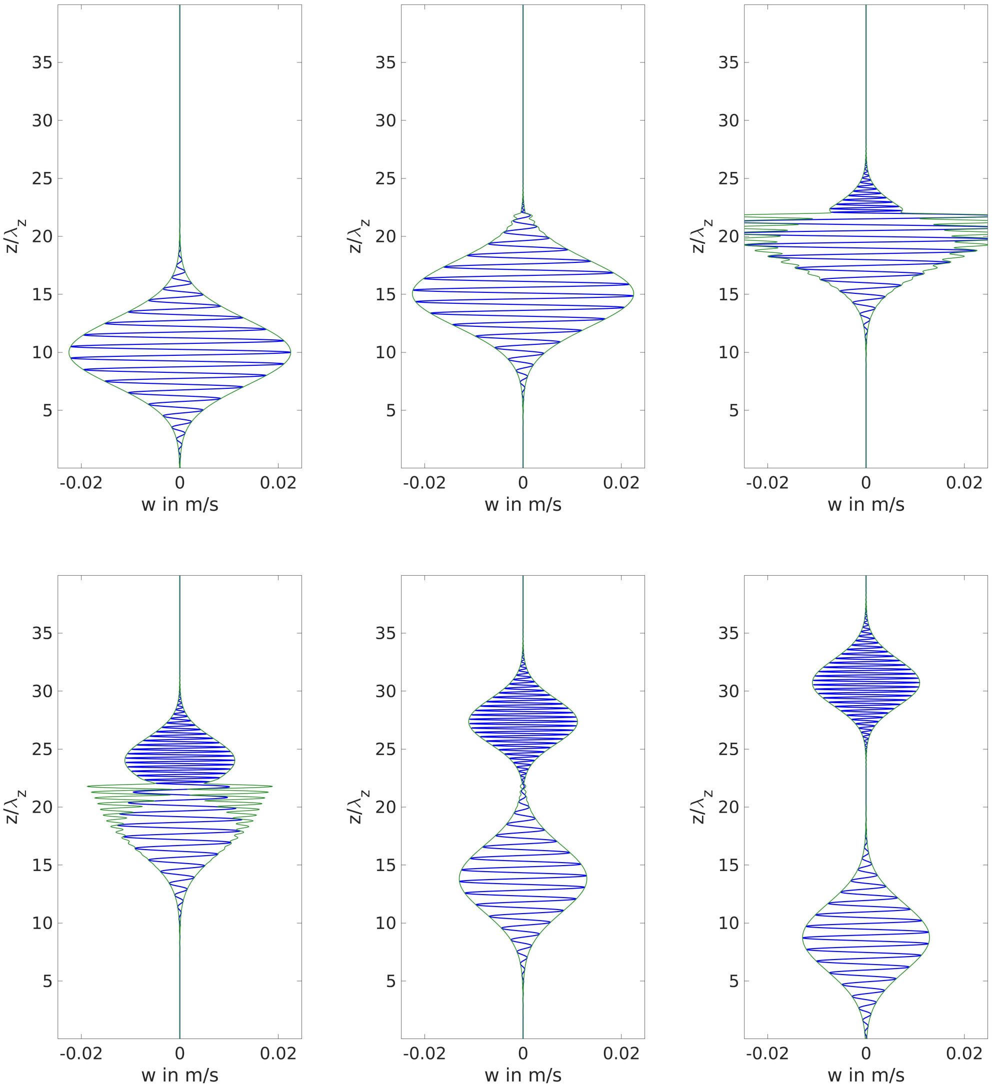

Figure 5.2: Reflection of a wave packet at tropopause profile of the shape that can be seen in figure 3.6. Snapshots are taken at at $t_N b = 0, 90, \ldots, 450$. Blue lines represent the vertical wind field, green lines indicate the envelope.

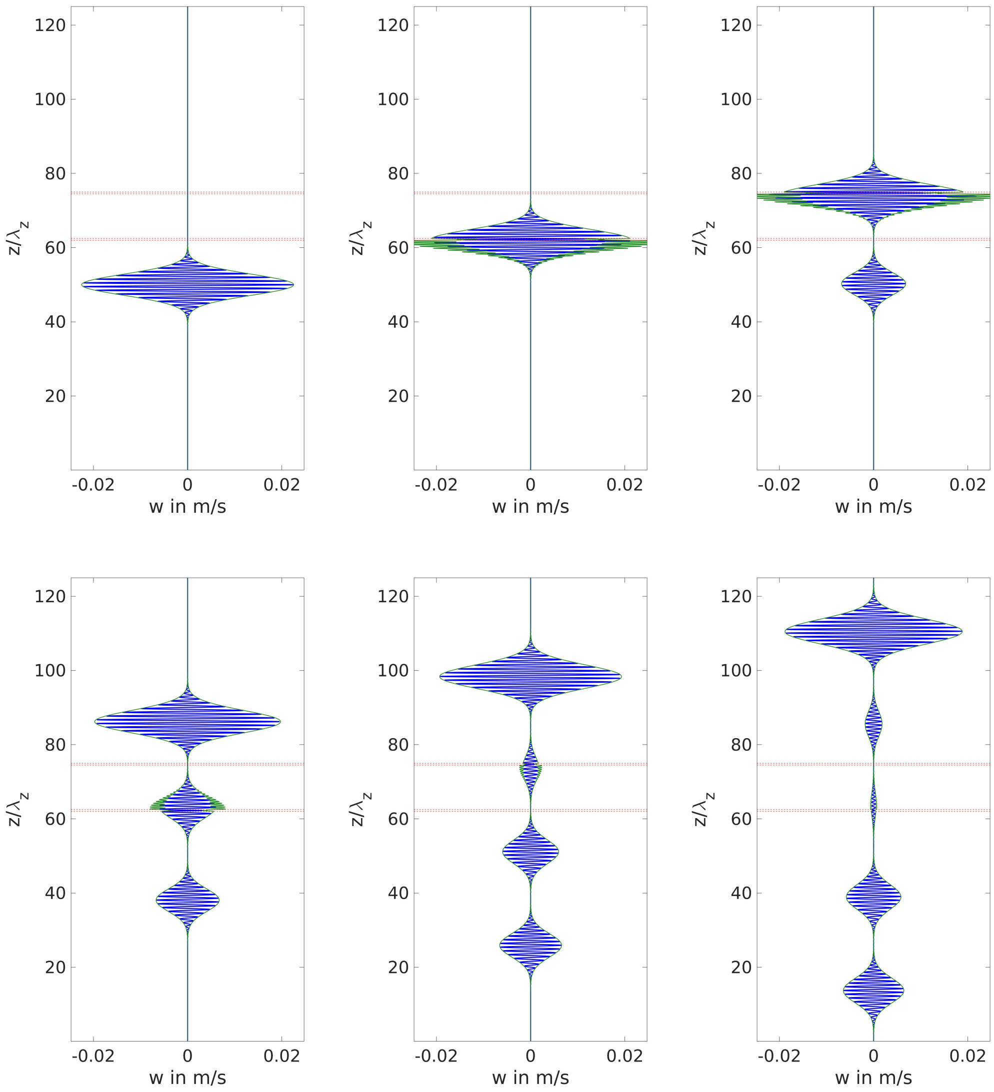

Figure 5.3: Propagation of a wave packet through twin peaks. The upper left panel shows the profile, the others show the wave packet. Snapshots taken at $tN_b = 0, 216, \ldots, 1080$. Blue lines represent the vertical wind field, green lines indicate the envelope, red horizontal lines show the locations of the peaks, which have a width of $\lambda_z/2$.

6 Numerical validation of the theoretical models

This section is devoted to the numerical validation of the multi-layer method. We conduct simulations of the full Boussinesq equations with an atmospheric flow solver and compare the findings to the solutions provided by the multi-layer method. We separate the cases for plane waves and wave packets. The focus for plane waves lies in the computation of transmission coefficients. For wave packets, we will investigate the propagation of the wave packets under different atmospheric conditions. The basic results of this chapter will also be found in the manuscripts Pütz et al. (2018) and Pütz and Klein (2018), but the exact values might differ from the ones found in there, as we made additional simulations for the thesis.

6.1 Model description

As reference model, we will use PincFloit (Pseudo-Incompressible Flow Solver with Implicit Turbulence), presented by Rieper et al. (2013b). The model conserves mass, energy and momentum. Moreover, it is a sound-proof model, which has two major advantages which make it a good choice for our needs. The first one is that all waves that occur are gravity waves. The second advantage is a direct consequence from the first one as the supressing of sound waves allows for larger time steps due the CFL criterion not having to consider the speed of sound. The model was tested favourably against standard cases. Rieper et al. (2013a) used PincFloit to check the range of validity of the extended WKB theory that was derived in Achatz et al. (2010). Very recently, Schlutow et al. (2017) used the model to validate their theoretical findings of travelling wave solutions to their modulation equations.

PincFloit has several built-in variants for the time scheme, flux, flux limiter and spatial reconstruction. We made several test runs, varying those parameters as well as others, for example the spatial resolution, CFL threshold, but also wave amplitude, in order to find a convenient setup that delivers accurate results as well as acceptable run times.

As time scheme, we used the low-storage third order Runge-Kutta scheme, which were extensively studied by Williamson (1980). The exact method can be found in Durran (1999). For spatial reconstruction, we pair the Runge-Kutta scheme with either a Godunov schmeme and central flux evaluations or a MUSCL scheme and upwind flux computations. For all computations, we have a monotonized central flux limiter and the

CFL threshold was chosen to be 0.9. The exact specifications for each simulation are available upon request.

PincFloit has a built-in switch for a Boussinesq atmosphere, i.e. constant background density, but due to extensions implemented by Dr. Gergely Bölöni, it is possible to have a non-constant profile for the Brunt-Väisälä frequency. Hence it was possible to implement the test cases of we needed into the solver. We use the same PincFloit version that was used by Bölöni et al. (2016) as a reference LES model. The only changes are the implementation of our atmospheric setups and the addition of a sponge layer at the bottom of the domain, which was written by Dr. Mark Schlutow for the purpose of generating plane waves in an atmosphere at rest.

6.2 Transmission coefficients for plane waves

This section focuses on numerical simulations with a plane wave forcing. We wish to compute transmission coefficients form the runs in order to compare them to the theoretically predicted values.

The model runs on a two-dimensional x-z-domain and covers 10000 m in z-direction and one horizontal wavelength in x-direction, which lies between 1000 m and 3000 m in the selected cases. This is necessary, since we have horizontally periodic boundary conditions. The vertical resolution is 10 m, which corresponds to 1000 grid cells in the vertical, the horizontal resolution is 25 m, if not stated otherwise.

We implement two sponge layers, one at the bottom of the domain and one at the top of the domain, but they serve inherently different purposes. While the top sponge layer absorbs and damps the wave, the bottom sponge layer is responsible for the excitation of the wave. Its relaxed state is a plane wave, so after a few time steps, the bottom sponge initialised a plane wave with given parameters that propagates freely above it in positive z-direction. The bottom sponge covers the lower 40% of the domain, which contains either two or four complete vertical wavelengths for the cases we are going to present. The top sponge occupies the upper 20% of the domain and is chosen such that the wave is completely damped away before reaching the top of the domain. This is important, since technically, we also have periodic boundary conditions in the vertical direction, so we do not want waves that reach the stratosphere to run into the domain again at the bottom. Moreover, we move the coordinate system with the horizontal phase velocity ω/k, which removes the temporal dependence of the wave field so that the waves eventually reach a steady state.

In all simulated runs, we can observe such a steady state after several hours of simulated time. It is very stable and lasts until the end time of the simulations, which was 10 hours in all cases. This has the effect that the steady state is present for a few hours of simulated time. This permits a very good computation of the transmission coefficient. As initial amplitude, we take the mean amplitude of the excited wave in the middle of the bottom sponge layer at a fixed time step after the wave has fully developed, as transmitted amplitude we take the mean amplitude of the wave in the stratospheric region. Moreover, the transmitted amplitude is computed every ten minutes of simulated time and the transmission coefficient is taken as mean over all computed values after reaching the steady state, which was in general assumed to be after 3 hours of simulated time.

Since our theory is developed for the linearised equations, but PincFloit uses the full Boussinesq equations we have to make sure that we set up the wave amplitudes small enough to ensure non-linear wave interactions are not affecting our results. Therefore, a variable that controls the amplitude of the initialised wave is introduced. This variable was chosen in a way that in all computations, the waves had an excitement amplitude of around $0.0743\,\mathrm{ms}^{-1}$, which in none of the cases was more than 7% of the static instability threshold, which is given by (see, for example, Achatz et al. (2010))

$$w_{stat} = \frac{km}{N^3\sqrt{k^2+m^2}}. \tag{6.1}$$

Besides eliminating non-linear wave-mean flow interaction, it has the additional advantage that the waves do not break during the simulations.

6.2.1 Linear increase

λ_z \ λ_x	1000	1500	2000	2500	3000	method
1000	0.9950	0.9964	0.9979	0.9985	0.9988	multi-layer
	0.9780	0.9713	0.9806	0.9911	0.9972	PincFloit
2000	0.9560	0.9799	0.9884	0.9892	0.9894	multi-layer
	0.9477	0.9826	0.9948	0.9957	0.9777	PincFloit

Table 6.1: Transmission coefficients for profile from figure 3.3 with a dimensional tropopause depth of 1000 m for different horizontal and vertical wavelength (also in m), computed theoretically with the multi-layer method and from PincFloit simulations.

In table 6.1, we find the comparison of the transmission coefficients obtained from the multi-layer method and from the numerical simulations of PincFloit. We see an impressive agreement of the values, deviations are in the order of 2%. If one wants to nitpick on this, a possible reason for the deviations could be the method we compute incident and reflected amplitude. Due to the nature of the sponge, there are some fluctuations in the initialised wave amplitude and hence also in the transmitted amplitude. We take care of this by averaging over a larger area, but this produces minor errors in the value for the transmission coefficient. Also a shifting of the averaging area produces slightly different values, but all in a very small range around the value we put in table 6.1. We should mention at this point that for each calculation, we used the same areas over which

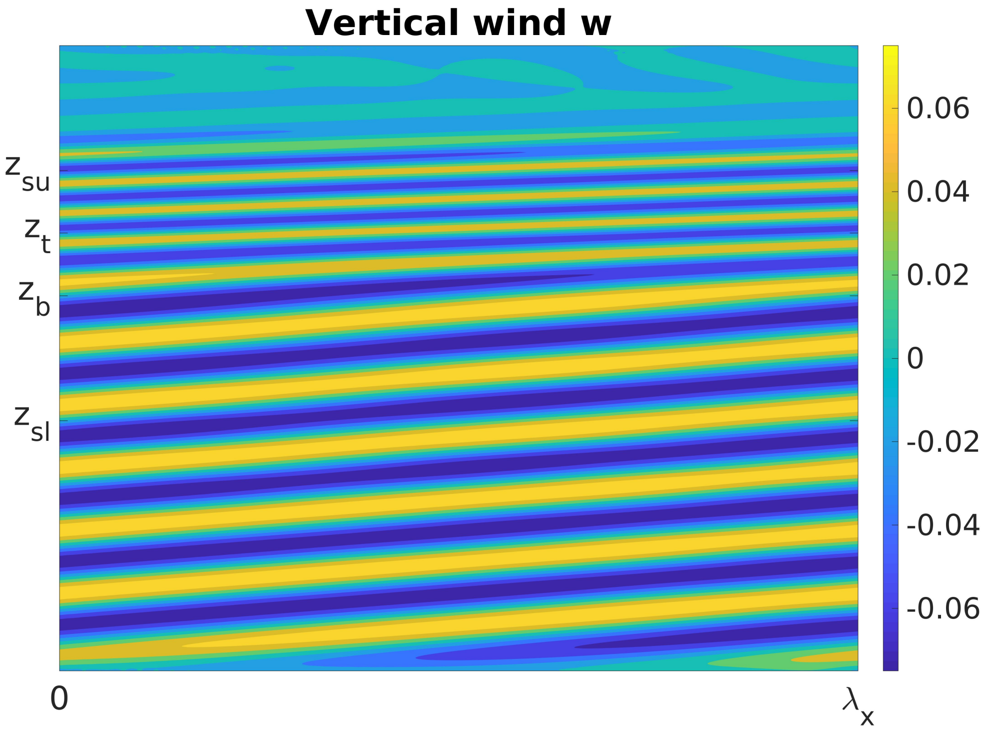

Figure 6.1: Vertical wind field of a PincFloit simulation for the linear case with a horizontal wavelength of 2500 m and an incident vertical wavelength of 1000 m. z_{sl} indicates where the lower sponge ends, the tropopause is between z_b and z_t and the top spnge extends from z_{su} to the domain top.

initial and transmitted amplitudes are averaged, as well as the same time point for the computation of the initial amplitude. This holds also true for the other cases.

The steady state for $\lambda_x = 2500\,\text{m}$ and $\lambda_z = 1000\,\text{m}$ can be seen in figure 6.1. We can see a refraction of the wave due to the change in vertical wavelength as well as no superposition of waves in the troposphere, which implies that the wave transmits almost completely. The smaller wave amplitude in the stratosphere (i. e. between 7000 m and 8000 m) is a result of the stronger stratification in this altitude.

6.2.2 Wave tunnelling

The simulation setup in this case uses fixed values for horizontal and vertical wavelength, but changes the depth of the tropopause, as this is numerically more convenient. Technically, we have the same wave frequency, but change the ratio between horizontal/ver-

$\frac{\Delta_z}{\lambda_z}$	0.1	0.2	0.5	1	method
TC	0.8648	0.5846	0.0916	0.0028	multi-layer
	0.8259	0.5580	0.0971	0.0030	PincFloit

Table 6.2: Transmission coefficients for profile from figure 3.4 with fixed vertical and horizontal wavelengths $\lambda_z = \lambda_x$ and varying tropopause depth Δ_z. This corresponds to a vertical cut along $\omega \approx 0.7$ in the left panel of figure 3.4.

tical wavelength and tropopause depth, so this corresponds to a vertical slice in the left panel of figure 3.4. By choosing $\lambda_x = \lambda_z$, as we did here, this results in a frequency $\omega = \frac{1}{\sqrt{2}} N_b \approx 0.707 N_b$. For tropopause depths that are comparable to λ_x, we expect strong reflection, while for a very short tropopause, we should obtain a wave tunnelling effect. The results can be seen in table 6.2. We used $\lambda_x = \lambda_z = 1000\,\mathrm{m}$.

PincFloit shows the behaviour that was anticipated by the theory. This is as much a quality check for the numerical model as it is supporting our theoretical findings. A ray tracer based on WKB theory would have found total reflection in all of the cases. This is because the WKB assumption is not valid any longer when the stratification changes significantly over a vertical extend much smaller than a wavelength.

Snapshots of the steady state for a high transmission and low transmission case can be seen in figure 6.2. It gives a very good comparison between the two cases as we can clearly see the differently pronounced alternating patterns, which are produced by the superposition of incident and reflected wave, as well as the disparity in the stratospheric amplitudes.

6.2.3 Realistic tropopause profile

$\lambda_z \backslash \lambda_x$	1000	1500	2000	2500	3000	method
1000	0.7858	0.8010	0.8095	0.8151	0.8185	multi-layer
	0.7757	0.8293	0.8428	0.8825	0.9046	PincFloit
2000	0.5635	0.6237	0.6620	0.6913	0.7113	multi-layer
	0.5347	0.6468	0.6358	0.7000	0.6991	PincFloit

Table 6.3: Transmission coefficients for profile from figure 3.6 with a dimensional tropopause depth of 1000 m for different horizontal and vertical wavelength (also in m).

Table 6.3 shows a comparison of values for the transmission coefficient obtained from the multi-layer method and values computed from PincFloit simulations.

For $\lambda_z = 2000\,\mathrm{m}$, we find that the values from the simulation coincide very nicely with the theoretically predicted ones. For $\lambda_z = 1000\,\mathrm{m}$ however, we see that the simulation produces a higher transmission than expected from the multi-layer method. To get to the

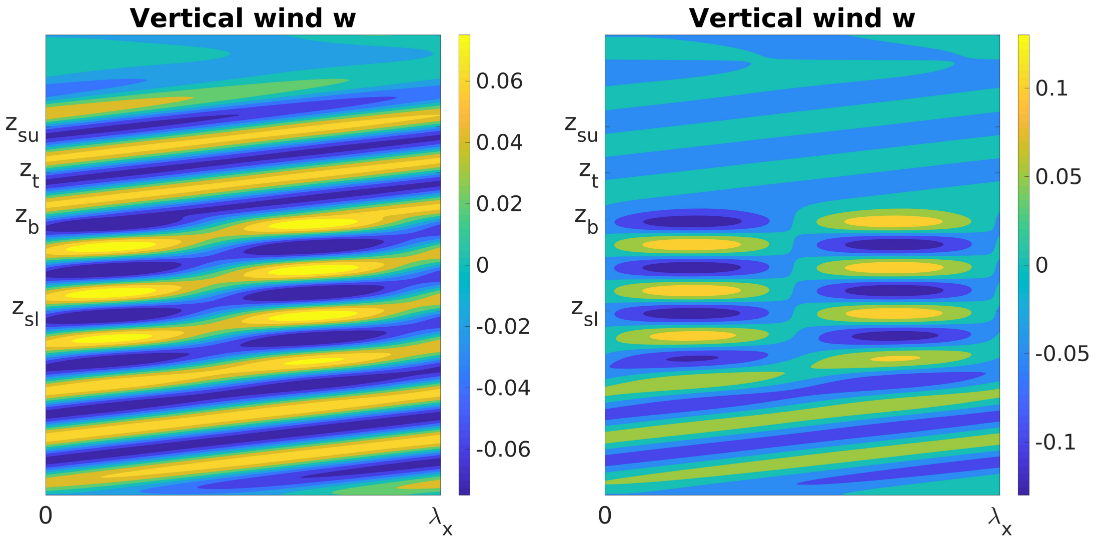

Figure 6.2: Snapshots of the wave field after 8 hours of simulated time from PincFloit simulations for the profile from figure 3.4. In both cases, we have horizontal and vertical wavelengths of 1000 m. In the left panel, the tropopause depth is 100 m. There is only a slight chequerboard pattern and comparable amplitudes above and below the tropopause. This suggests a high transmission. In the right panel, the tropopause depth is 500 m. Note the different color codes.

bottom of this, we pick the case $\lambda_x = 2000\,\text{m}, \lambda_z = 1000\,\text{m}$ and simulate with different setups. The results can be found in table 6.4.

The reference case was the resolution as described at the beginning of this section. We also distinguish between simulations done with a MUSCL scheme and with a Godunov scheme. We observe from the reference simulation that the Godunov scheme has an even higher transmission. For the different computation (DiffComp) of the initial amplitude, we did not compute it once at took this value for all transmitted amplitudes, but took a new initial amplitude for each time step. We estimated how long the wave needs to propagate from the sponge layer into the stratosphere and took the corresponding

Case	Reference	DiffComp	CFL05	$dx = 50\,\text{m}$	$dx = 10\,\text{m}$
TC, MUSCL	0.8428	0.8392	0.8429	0.7858	0.8624
TC, Godunov	0.8520	0.8482	no data	0.8277	no data

Table 6.4: Transmission coefficients for the realistic tropopause with $\lambda_x = 2000\,\text{m}, \lambda_z = 1000\,\text{m}$ and different numerical setups.

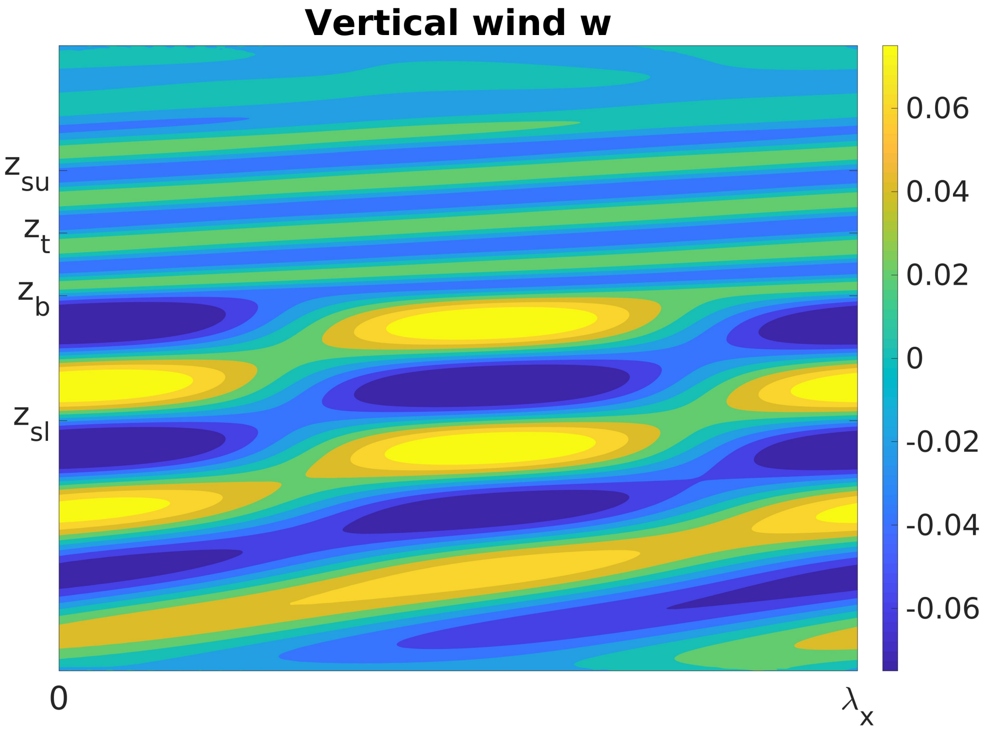

Figure 6.3: Vertical wind field of a PincFloit simulation for the case of the realistic tropopause profile with a horizontal wavelength of 2000 m and a vertical wavelength of 2000 m and with a tropopause depth of 1000 m. z_{sl} indicates where the lower sponge ends, the tropopause is between z_b and z_t and the top sponge extends from z_{su} to the domain top.

average in the sponge layer at that time point. This should eliminate potential biases through fluctuations from the initialised wave. As we can see, this has a rather minor effect. The next setup set the CFL-condition to 0.5, resulting in shorter time steps. This had no influence on the wave transmission at all, and hence we passed on simulating this case also with the Godunov scheme. As we already knew from Pütz et al. (2018), where we simulated the case with a coarser horizontal resolution, we should find transmission coefficients closer to the theoretically predicted one when decreasing the resolution. Therefore, we run simulations with a horizontal resolution of 50 m and could confirm this assumption. A test run with a 10 m horizontal resolution had the effect of further increasing the transmission.

As the decrease in horizontal resolution seems to have an impact on the wave propagation, we did test runs for different wave parameters and stratification profiles. We could

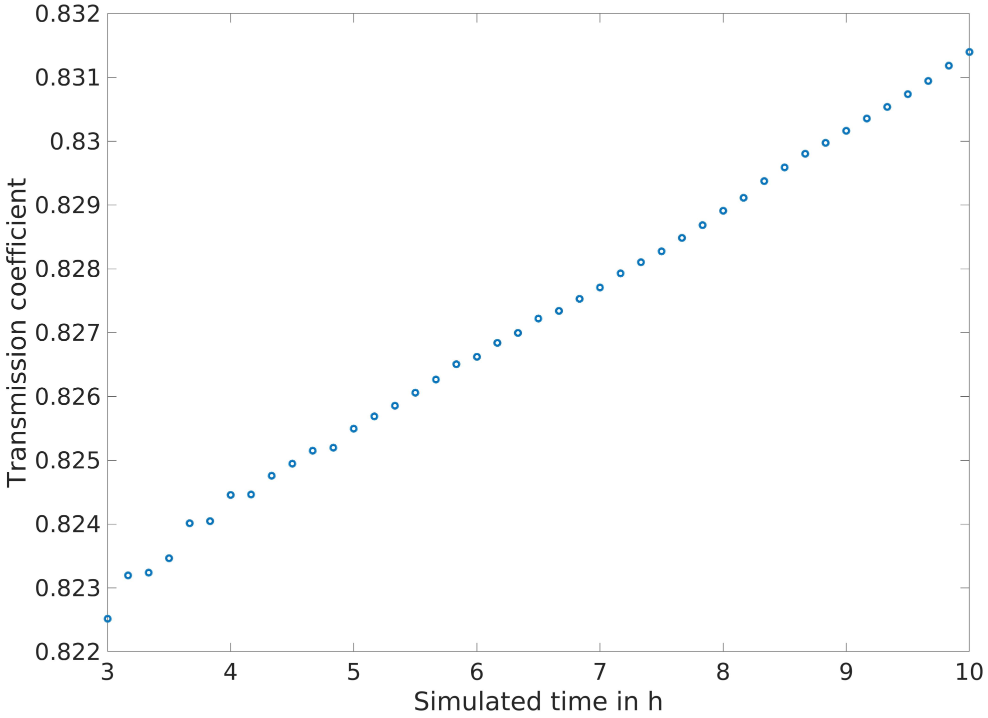

Figure 6.4: Transmission coefficient over time for $\lambda_x = 1000\,\mathrm{m}, \lambda_z = 1000\,\mathrm{m}$, retrieved from a PincFloit simulation with a Godunov scheme.

partially observe the same effect, although it is not certain if the low resolution underestimates or the high resolution overestimates the transmission.

Another effect that could sometimes be observed for the realistic tropopause case was an increase in the transmission coefficient over time, most prominent in the case with $\lambda_x = 1000\,\mathrm{m}, \lambda_z = 1000\,\mathrm{m}$, simulated with a Godunov scheme. This can be seen in figure 6.4. We observe that over the course of the simulation, the stratospheric amplitude grows, leading to larger values for the transmission coefficient. Increasing the simulation time from 10 to 80 hours revealed that the simulation eventually gets unstable at some point, producing highly oscillating noise.

Our guess is that because of the sharp increase in stratification, which is resolved rather coarse by the model, PincFloit has some issues with the conservation of energy, causing wave amplitudes that are higher than they should be. We are, however, no experts on numerical simulations in general and on PincFloit in particular, but this seems to be an interesting point to hook in some more research.

To conclude this section, we can say that in general, the numerical simulations match very well with the theoretical predictions. Hence, the multi-layer method is a potent tool to predict gravity wave transmission and reflection in non-uniform background. Because the computation of the transmission coefficient is very fast and cheap, there is the incentive to use it as a black box in numerical weather prediction.

6.3 Evolution of wave packets in non-uniform background

In this section, we will compare the evolution of gravity wave packets that is obtained with the method presented in section 5.4 and the evolution that is computed with PincFloit.

We emphasise again that our approach addresses the linearised equations, so that there is no interaction of the wave packet with the background flow. This will be realised by choosing the initial wave amplitude small compared to the static instability threshold, an estimate of which is discussed by Achatz et al. (2010). For the vertical wind, it is given by

$$w_{\mathrm{si}} = \left| \frac{\hat{\omega}}{m} \right| . \tag{6.2}$$

Case	Wave packet specs	background wind specs
REFR	$z_0 = 10\,\mathrm{km}$, $\varDelta_{wp} = 10\,\mathrm{km}$, $\lambda_x = 10\,\mathrm{km}$, $\lambda_z = 1\,\mathrm{km}$	$z_U = 30\,\mathrm{km}$, $\varDelta_U = 20\,\mathrm{km}$, $U_0 = -5\,\mathrm{ms}^{-1}$
REFL	$z_0 = 10\,\mathrm{km}$, $\varDelta_{wp} = 10\,\mathrm{km}$, $\lambda_x = 10\,\mathrm{km}$, $\lambda_z = 1\,\mathrm{km}$	$z_U = 30\,\mathrm{km}$, $\varDelta_U = 20\,\mathrm{km}$, $U_0 = -40\,\mathrm{ms}^{-1}$
PREFL	$z_0 = 20\,\mathrm{km}$, $\varDelta_{wp} = 10\,\mathrm{km}$, $\lambda_x = 6\,\mathrm{km}$, $\lambda_z = 3\,\mathrm{km}$	$z_U = 45\,\mathrm{km}$, $\varDelta_U = 20\,\mathrm{km}$, $U_0 = -9.75\,\mathrm{ms}^{-1}$

Table 6.5: Wave packet setups

As reference cases, we have a look at atmospheric setups with a refraction (REFR), a total reflection (REFL) and a partial reflection (PREFL) of a wave packet by a wind jet, as already studied by Bölöni et al. (2016). In all three cases, the initial wave packet is a cosine-shaped wave packet with a total width of $\varDelta_{wp} = 2\sigma_{wp} = 10\,\mathrm{km}$. The complete formula for the initial vertical wind is

$$w(x,z,0) = \begin{cases} \Re\left(a_0 w_{\mathrm{si}} \frac{1}{2} \left(1 + \cos\left(\frac{\pi(z-z_0)}{\sigma_{wp}} \right) \right) \exp(i(kx + m_0 z)) \right), & \text{if } |z - z_0| \le \sigma_{wp} \\ 0, & \text{otherwise.} \end{cases} \tag{6.3}$$

Here, a_0 is a parameter that controls the wave amplitude, z_0 is the center of the wave packet and $\sigma = \varDelta_{wp}/2$ is the half-width of the packet. As we are interested in the linear behaviour, we set $a_0 = 0.01$. It can be shown that the Fourier transform of the initial condition is

$$\widehat{w}(x,m,0) = \exp(ikx)\left(\frac{\pi^2 \sin(\sigma_{wp}(m_0 - m))}{(\pi - m\sigma_{wp} + m_0\sigma_{wp})(\pi + m\sigma_{wp} - m_0\sigma_{wp})(m_0 - m)} + \frac{\pi^2 \sin(\sigma_{wp}(m_0 + m))}{(\pi + m\sigma_{wp} + m_0\sigma_{wp})(\pi - m\sigma_{wp} - m_0\sigma_{wp})(m_0 + m)}\right) \tag{6.4}$$

hence we can apply the multi-layer method. Although it might seem at first glance that $\widehat{w}(x,m,0)$ has a singularity at $m = m_0$, it can be shown that the limit $m \to m_0$ of the first term in parenthesis exists, as both numerator and denominator tend to 0, so we can use the L'Hôpital's rule, which then reveals that the limit tends to a finite value.

For the background wind, we assume a cosine-shaped jet with width $\mathit{\Delta}_U = 2\sigma_U = 20\,\mathrm{km}$ and peak velocity U_0 at location z_U. Expressed in formulas, this is

$$\overline{U}(z) = \begin{cases} \frac{U_0}{2}\left(1 + \cos\left(\frac{\pi(z - z_U)}{\sigma_U}\right)\right), & \text{if } |z - z_U| \leq \sigma_U \\ 0, & \text{otherwise.} \end{cases} \tag{6.5}$$

Here, $\sigma_U = \frac{\mathit{\Delta}_U}{2}$ is the half-width of the jet profile. The exact wave packet and background specifications for the cases REFR, REFL and PREFL can be found in table 6.5. Wen ran the methods on a domain of 80 km in the vertical for the cases REFR and PREFL and on a domain of 40 km for the case REFL. The number of grid points was 1200 for REFR and PREFL, and 600 for REFR, resulting in a vertical resolution of 66.67 m in each of the cases. The time span was 33.33 h for REFR, with an output created every 1200 s, resulting in 101 outputs, when counting the initial output at time 0. The time span for REFR was 24 h, with an output created every 1200 s, resulting in 73 outputs. The time domain for PREFL was 6h, with an output every 180 s, resulting in 121 outputs.

In figure 6.5, we see a Hovmöller plot of the horizontally averaged wave action, normalised by the background density, given by

$$2\rho_0^{-1}\langle\mathcal{A}\rangle = 2\rho_0^{-1}\frac{\langle E\rangle}{\hat{\omega}} = \frac{N_0^2}{\hat{\omega}_0^2}\frac{(\max_x w(x, z_s, t_s))^2}{(\omega - k\overline{u}(z_s))} \tag{6.6}$$

for the case REFR. Here, z_s and t_S represent space and time points of interest. The left panel displays the solution computed with the multi-layer method, the middle panel was created from a PincFloit simulation of the full Boussinesq equations with the same setup. We can see a very good agreement of both approaches, not only qualitatively but also quantitatively. This can be seen in the right panel, where the absolute error between both methods is shown. For reference, we chose the same color code in all three plots. The amplitudes of the initialised wave packets in our model setup differ by approximately 4%, but this value further decreases when we increase the vertical resolution. Moreover, both methods behave almost identically in terms of quality. We can see what appears

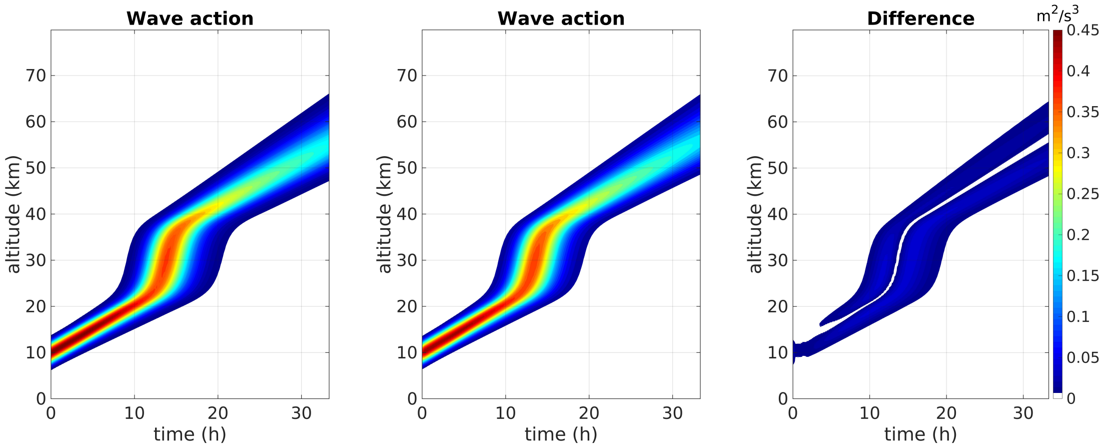

Figure 6.5: Hovmöller plot of wave action for the case REFR. The left panel displays the solution computed with the multi-layer method, the middle panel shows the solution from a PincFloit simulation, the right panel shows their difference.

to be a refraction of the propagation direction in the area where $\overline{u}$ is different from zero (steeper angle). In fact, we have an increase in vertical group velocity due to a decrease in vertical wavenumber. This looks like a refraction in the Hovmöller plot. The increase in vertical group velocity is also responsible for the broadening of the wave packet in the jet area, additionally to the broadening that occurs due to dispersion.

In figure 6.6, we see a Hovmöller plot of the horizontally averaged wave action for the case REFL. Again, the left panel shows the multi-layer solution, the middle panel shows the PincFloit simulation. In the right panel, we can see their difference. As in the REFR case, the solutions match very well. There is however some wiggling in the PincFloit solution near the bottom. This occurs because the solver is set up with periodic boundary conditions and a sponge layer at the top of the domain which relaxes to a steady background. This causes the solution, that runs out of the bottom and right into the sponge to partially reflect from there, causing the wiggles. This issue could be fixed by enlarging the sponge locally, but also increasing the relaxation time. This has however the disadvantage of enlarging the whole simulation domain, making the whole simulation more costly and not giving appropriately better results. Near the reflection level, we see the superposition of the wave packet with itself: the front part is already reflected while the back part is still travelling upward. The reflection level is too strong for partial reflection to occur, the whole packet is eventually reflected. The multi-layer method captures time and location of the reflection from the simulation very well.

In figure 6.7, we see a Hovmöller plot of the horizontally averaged wave action for the case PREFL. Again, the left panel shows the multi-layer solution, the middle panel shows

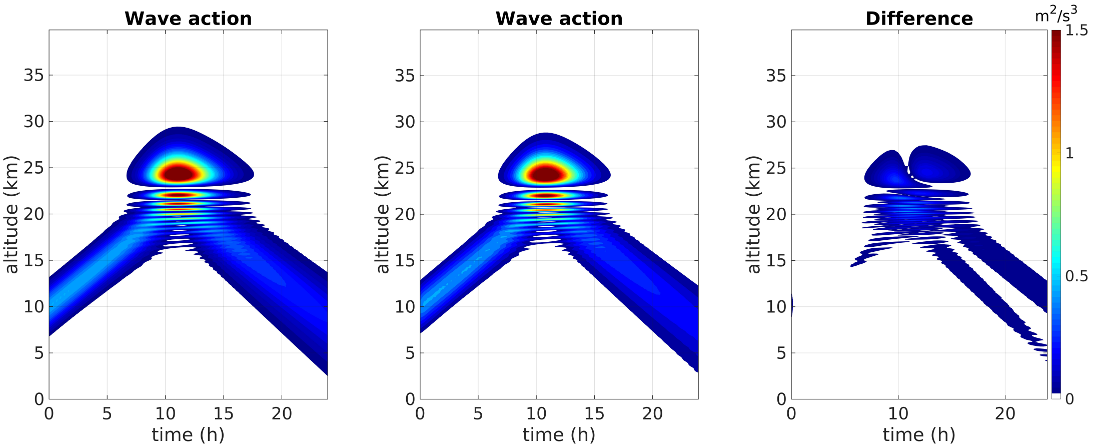

Figure 6.6: Hovmöller plot of wave action for the case REFL. The left panel displays the solution computed with the multi-layer method, the middle panel shows the solution from a PincFloit simulation, the righ panel shows their difference.

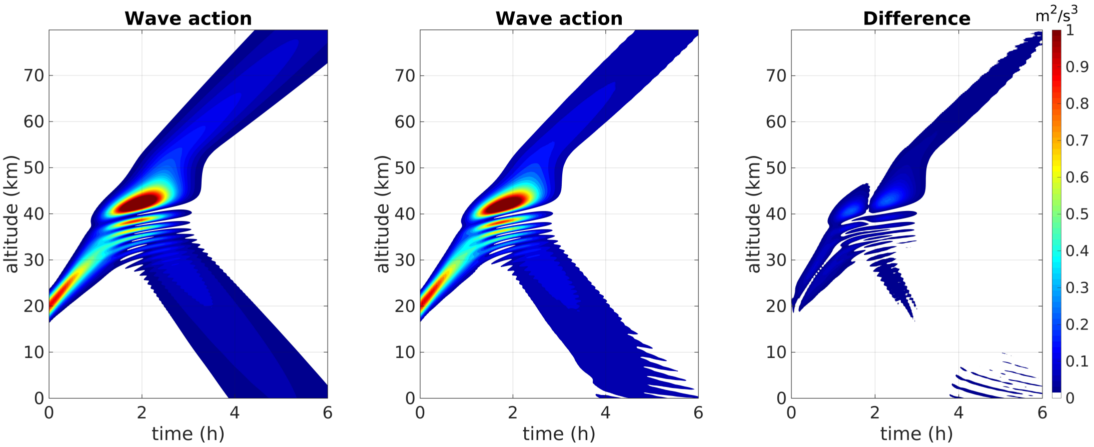

Figure 6.7: Hovmöller plot of wave action for the case PREFL. The left panel displays the solution computed with the multi-layer method, the middle panel shows the solution from a PincFloit simulation, the righ panel shows their difference.

the PincFloit simulation and the right panel displays their difference. The wiggling near the bottom is even stronger here, but apart from that, the solutions match pretty well. The reflection level in this case is moderately strong and we have only a partial reflection of wave action from the jet. This is a feature that can not be represented by classical ray tracers. Wave packet with this setup would totally reflect from such a level, while other methods do allow for partial reflection (see Bölöni et al. (2016)). As in the REFL case, time and location of the partial reflection coincide very well between both methods.

It is impressive how well the multi-layer method approximates the numerical solution in all three test cases. The qualitative as well as the quantitative behaviour of the wave packet is completely captured by the multi-layer approach. There is no downside in using it over a simulation of the full Boussinesq equations, as long as the wave amplitudes are reasonably small.

6.4 Non-linear effects

By increasing a_0 in equation (6.3), we increase the wave amplitude, essentially increasing the importance of non-linear wave-wave and wave-mean flow interactions. Since the multi-layer method is fully based on linear theory, we used a small value for a_0, effectively reducing PincFloit to a linear solver. On the one hand, this section serves the purpose of showing that PincFloit accounts for non-linear effects as well as wave breaking and on the other hand gives a hint until when the linear theory yields sufficient results.

In figure 6.8, we see Hovmöller plots of the wave action for wave packets with $a_0 = 0.1$ (upper row), $a_0 = 0.3$ (middle row) and $a_0 = 0.7$ (lower row), computed with the multi-layer method (left column) and PincFloit (middle column). In the right column, we can see the difference between the two methods. For comparison, the middle panel in figure 6.7 was computed with $a_0 = 0.01$. The three images in the left column are practically identical, except for the scale. The reason for this is that the multi-layer method is a linear method, hence increasing the amplitude does not change the dynamics. The upper middle panel is very similar to the left and middle panel of figure 6.7. Even though we increased the amplitude by a factor of 10, the linear approximation does a fairly good job, as can be seen in the difference of the two methods. In the middle panel, the overall behaviour is still captured quite nicely, although there is much more wave energy reflected, probably due to the acceleration of the jet by the wave packet itself. In the middle lower panel, the initialised wave packet is close to static instability. We can still see that the first part of the wave packet is partially reflected (indicated by the wave action that reaches the bottom of the domain at around 2.5 h), but due to non-linear interactions, it causes the remainder of the wave packet to break and dissipate.

In table 6.6, we can see the maximum vertical wind speed for the initial wave packet for the different cases. When we compare these values with findings for gravity waves in the upper troposphere by Thomas et al. (1999), who find gravity waves with vertical

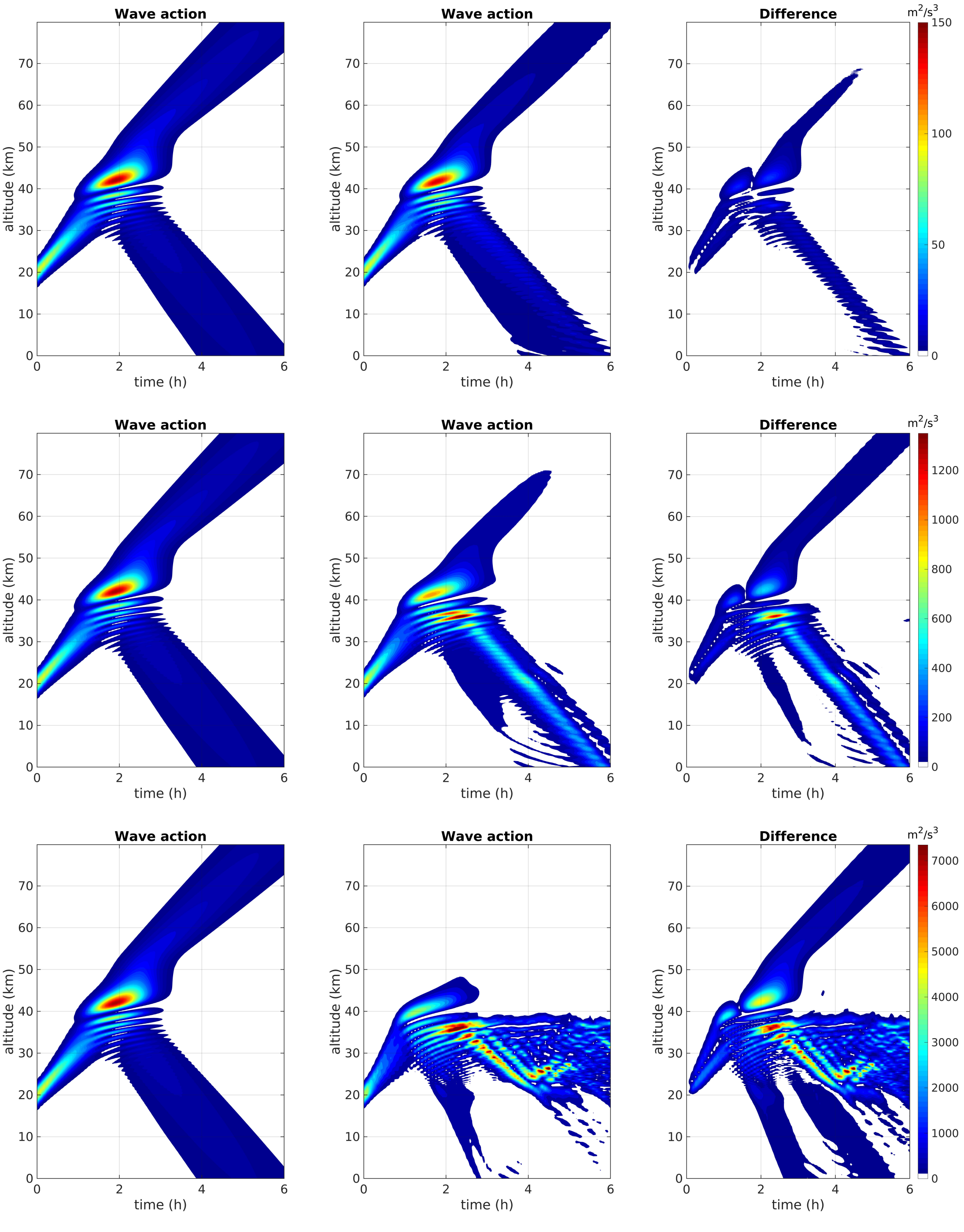

Figure 6.8: Hovmöller plot of wave action for the case PREFL, computed with the Multi-layer method (first column), PincFloit (second column) and their difference (third column). The rows represent different values for a_0: $a_0 = 0.1$ in the upper row, $a_0 = 0.3$ in the middle row and $a_0 = 0.7$ in the lower row.

	$a_0 = 0.1$	$a_0 = 0.3$	$a_0 = 0.7$
multi-layer	0.3639	1.0917	2.5474
PincFloit	0.3829	1.1461	2.6741

Table 6.6: Maximal vertical wind speed in ms^{-1} for the initialised wave packet for the different setups

wind amplitudes around $0.3\,\mathrm{ms}^{-1}$, we observe that the case $a_0 = 0.1$ seems realistic, while the other cases represent very strong gravity waves. Hence, we can conclude that the multi-layer method can also serve as a valid approximation for gravity waves in the tropopause region.

7 Scale analysis of the governing equations

This chapter presents a different approach to the gravity wave-tropopause interaction. We will have a look at the governing equations in a non-dimensional setup, where we use different reference values for different scaling regimes. As we already noticed in section 3.6, waves show different behaviour for different ratios of wavelength to tropopause depth. We will put emphasis on three different regimes of wavelengths: short, comparable and long compared to the tropopause depth. For each of these regimes, we will find an appropriate scaling and derive the governing equations that describe the interaction of gravity waves with the tropopause. The idea behind that procedure is the hope that we can find solutions for the simplified leading- and maybe first-order equations.

For the remainder of the chapter, we will assume an atmosphere at rest.

7.1 Short waves

This section covers the theory of gravity waves that encounter the tropopause and have a wavelength $\mathit{\Lambda}$ much shorter than the tropopause depth L_{TP}. This is reflected with a small separation parameter δ in the relation

$$\mathit{\Lambda}_{\mathrm{ref}} = \delta L_{\mathrm{TP}}. \tag{7.1}$$

Moreover, the depth of the tropopause is small when compared to the potential temperature scale height H_θ. We indicate this by a small separation parameter ε, i.e.

$$L_{\mathrm{TP}} = \varepsilon H_\theta. \tag{7.2}$$

As both ε and δ shall reflect a similar ratio, we choose the distinguished limit $\delta = \varepsilon$. Moreover, we use the isothermal approximation $H_\theta = c_p T_{\mathrm{ref}}/g$ for the potential temperature scale height, where T_{ref} is a reference value for the absolute temperature. We obtain the relation,

$$\mathit{\Lambda}_{\mathrm{ref}} = \varepsilon^2 H_\theta = \varepsilon^2 \frac{c_p T_{\mathrm{ref}}}{g} \Leftrightarrow \varepsilon^2 = \frac{\mathit{\Lambda}_{\mathrm{ref}} g}{c_p T_{\mathrm{ref}}}, \tag{7.3}$$

We want to focus on non-hydrostatic waves with $\mathit{\Lambda}_x \sim \mathit{\Lambda}_z \sim \mathit{\Lambda}$. As wavelengths and frequency $\mathit{\Omega}_{\mathrm{ref}}$ should be related by the dispersion relation (5.5), we obtain a scaling for the frequency via

$$\Omega_{\mathrm{ref}} = N_{\mathrm{ref}} = \frac{g}{\sqrt{c_p T_{\mathrm{ref}}}}. \tag{7.4}$$

where $N_r f$ is the isothermal approximation of the Brunt-Väisälä frequency, as it is a good indicator for the values that are present especially above the tropopause. This results in a time scaling

$$t_{\mathrm{ref}} = \Omega_{\mathrm{ref}}^{-1}. \tag{7.5}$$

For the velocity scaling, we use the advective scaling

$$U_{\mathrm{ref}} = \Lambda_{\mathrm{ref}}\Omega_{\mathrm{ref}} = \Lambda_{\mathrm{ref}} N_{\mathrm{ref}}, \tag{7.6}$$

as this is the usual regime for the Boussinesq equations (Klein, 2010). Moreover, we choose values for the background potential temperature and Exner pressure to be

$$\Theta_b = T_{\mathrm{ref}}, \tag{7.7}$$

$$\Pi_b = 1, \tag{7.8}$$

(see also Achatz et al. (2010)). With the help of the polarisation relations (3.11) and(3.12), we find a scaling for the wave fluctuations in potential temperature and pressure:

$$\theta_{\mathrm{ref}} = \frac{N_{\mathrm{ref}}^2}{\Omega_{\mathrm{ref}}}\frac{T_{\mathrm{ref}}}{g}\Lambda_{\mathrm{ref}}\Omega_{\mathrm{ref}} = \frac{\Lambda_{\mathrm{ref}} g}{c_p T_{\mathrm{ref}}} T_{\mathrm{ref}} \tag{7.9}$$

and

$$\Pi_{\mathrm{ref}} = \frac{\Lambda_{\mathrm{ref}}^{-1}}{\Lambda_{\mathrm{ref}}^{-2}}\frac{\Omega_r f}{c_p T_{\mathrm{ref}}}\Lambda_r f \Omega_r f = \frac{\Lambda_{\mathrm{ref}}^2 g^2}{c_p^2 T_{\mathrm{ref}}^2} \tag{7.10}$$

Using equation (7.3), we obtain

$$\frac{\theta_{\mathrm{ref}}}{\Theta_b} = \varepsilon^2 \tag{7.11}$$

and

$$\frac{\Pi_{\mathrm{ref}}}{\Pi_b} = \varepsilon^4. \tag{7.12}$$

Hence, we expect wave fluctuations for potential temperature in second order and for pressure in fourth order. Using the notation

$$f^* = \frac{f}{f_{\mathrm{ref}}} \tag{7.13}$$

for the dimensionless representation of all dependent and independent variables, we obtain the following scaling (this notation should not be confused with the *-operator we used earlier). We start with the Euler equations (2.1), but we already replace the conservation of mass (2.1d) with its incompressible counterpart (2.7), as we assume a constant background in leading order due to the Boussinesq approximation.

7.1.1 Non-dimensional equations

For the horizontal momentum equation, we find

$$\begin{aligned}\frac{\varLambda_{\mathrm{ref}}N_{\mathrm{ref}}}{N_{\mathrm{ref}}^{-1}}\frac{\partial u^*}{\partial t^*}+\frac{\varLambda_{\mathrm{ref}}^2N_{\mathrm{ref}}^2}{\varLambda_{\mathrm{ref}}}\left(u^*\frac{\partial u^*}{\partial x^*}+w^*\frac{\partial u^*}{\partial z^*}\right)+\frac{c_pT_{\mathrm{ref}}}{\varLambda_{\mathrm{ref}}}\theta^*\frac{\partial \pi^*}{\partial x^*}&=0\\ \Leftrightarrow\frac{\varLambda_{\mathrm{ref}}^2N_{\mathrm{ref}}^2}{c_pT_{\mathrm{ref}}}\left(\frac{\partial u^*}{\partial t^*}+u^*\frac{\partial u^*}{\partial x^*}+w^*\frac{\partial u^*}{\partial z^*}\right)+\theta^*\frac{\partial \varPi^*}{\partial x^*}&=0\\ \Leftrightarrow\frac{\varLambda_{\mathrm{ref}}^2g^2}{c_p^2T_{\mathrm{ref}}^2}\left(\frac{\partial u^*}{\partial t^*}+u^*\frac{\partial u^*}{\partial x^*}+w^*\frac{\partial u^*}{\partial z^*}\right)+\theta^*\frac{\partial \varPi^*}{\partial x^*}&=0\\ \Leftrightarrow\varepsilon^4\left(\frac{\partial u^*}{\partial t^*}+u^*\frac{\partial u^*}{\partial x^*}+w^*\frac{\partial u^*}{\partial z^*}\right)+\theta^*\frac{\partial \varPi^*}{\partial x^*}&=0\end{aligned}\tag{7.14}$$

In a similar fashion, the vertical momentum equation reads

$$\begin{aligned}\frac{\varLambda_{\mathrm{ref}}N_{\mathrm{ref}}}{N_{\mathrm{ref}}^{-1}}\frac{\partial w^*}{\partial t^*}+\frac{\varLambda_{\mathrm{ref}}^2N_{\mathrm{ref}}^2}{\varLambda_{\mathrm{ref}}}\left(u^*\frac{\partial w^*}{\partial x^*}+w^*\frac{\partial w^*}{\partial z^*}\right)+\frac{c_pT_{\mathrm{ref}}}{\varLambda_{\mathrm{ref}}}\theta^*\frac{\partial \varPi^*}{\partial z^*}&=-g\\ \Leftrightarrow\frac{\varLambda_{\mathrm{ref}}^2N_{\mathrm{ref}}^2}{c_pT_{\mathrm{ref}}}\left(\frac{\partial w^*}{\partial t^*}+u^*\frac{\partial w^*}{\partial x^*}+w^*\frac{\partial w^*}{\partial z^*}\right)+\theta^*\frac{\partial \varPi^*}{\partial z^*}&=-\frac{\varLambda_{\mathrm{ref}}g}{c_pT_{\mathrm{ref}}}\\ \Leftrightarrow\frac{\varLambda_{\mathrm{ref}}^2g^2}{c_p^2T_{\mathrm{ref}}^2}\left(\frac{\partial w^*}{\partial t^*}+u^*\frac{\partial w^*}{\partial x^*}+w^*\frac{\partial w^*}{\partial z^*}\right)+\theta^*\frac{\partial \varPi^*}{\partial z^*}&=-\frac{\varLambda_{\mathrm{ref}}g}{c_pT_{\mathrm{ref}}}\\ \Leftrightarrow\varepsilon^4\left(\frac{\partial w^*}{\partial t^*}+u^*\frac{\partial w^*}{\partial x^*}+w^*\frac{\partial w^*}{\partial z^*}\right)+\theta^*\frac{\partial \varPi^*}{\partial z^*}&=-\varepsilon^2\end{aligned}\tag{7.15}$$

For the entropy equation as well as the divergence constraint, we will see that all terms have the same factor, thus, it can be removed:

$$\begin{aligned}\frac{T_{\mathrm{ref}}}{N_{\mathrm{ref}}^{-1}}\frac{\partial \theta^*}{\partial t^*}+\frac{\varLambda_{\mathrm{ref}}N_{\mathrm{ref}}T_{\mathrm{ref}}}{\varLambda_{\mathrm{ref}}}\left(u^*\frac{\partial \theta^*}{\partial x^*}+w^*\frac{\partial \theta^*}{\partial z^*}\right)&=0\\ \Leftrightarrow\frac{\partial \theta^*}{\partial t^*}+\left(u^*\frac{\partial \theta^*}{\partial x^*}+w^*\frac{\partial \theta^*}{\partial z^*}\right)&=0\end{aligned}\tag{7.16}$$

and

$$\begin{aligned} \frac{\Lambda_{\text{ref}} N_{\text{ref}}}{\Lambda_{\text{ref}}} \left(\frac{\partial w^*}{\partial x^*} + \frac{\partial w^*}{\partial z^*} \right) &= 0 \\ \Leftrightarrow \frac{\partial w^*}{\partial x^*} + \frac{\partial w^*}{\partial z^*} &= 0 \end{aligned} \tag{7.17}$$

Summarised, the non-dimensional Boussinesq equations for a short wave scaling are

$$\varepsilon^4 \left(\frac{\partial u^*}{\partial t^*} + u^* \frac{\partial u^*}{\partial x^*} + w^* \frac{\partial u^*}{\partial z^*} \right) + \theta^* \frac{\partial \Pi^*}{\partial x^*} = 0 \tag{7.18a}$$

$$\varepsilon^4 \left(\frac{\partial w^*}{\partial t^*} + u^* \frac{\partial w^*}{\partial x^*} + w^* \frac{\partial w^*}{\partial z^*} \right) + \theta^* \frac{\partial \Pi^*}{\partial x^*} = -\varepsilon^2 \tag{7.18b}$$

$$\frac{\partial \theta^*}{\partial t^*} + \left(u^* \frac{\partial \theta^*}{\partial x^*} + w^* \frac{\partial \theta^*}{\partial z^*} \right) = 0 \tag{7.18c}$$

$$\frac{\partial w^*}{\partial x^*} + \frac{\partial w^*}{\partial z^*} = 0 \tag{7.18d}$$

7.1.2 Multi-scale ansatz

We make a general multi-scale ansatz

$$f^*(x, z, \zeta, t) = \sum_{j=0}^{\infty} \varepsilon^j f^{(j)}(x, z, \zeta, t), \tag{7.19}$$

with two vertical scales z^* and ζ^*, where z^* represents the wavelength scale and $\zeta^* = \varepsilon z^*$ represents the tropopause scale. Remember that we are in the Boussinesq approximation, saying that the density does not vary significantly over the tropopause. The same is true for the potential temperature and hence the pressure.Therefore, we anticipate that the leading order values $\theta^{(0)}$ and $\Pi^{(0)}$ are constant. It is, however, only necessary to require this for the potential temperature, the statement for the leading order pressure is then derived from the leading- and first order momentum balances. Hence, we only assume that the leading order potential temperature is constant and not zero, i.e.

$$\theta^{(0)} \equiv \theta_0 > 0 \tag{7.20}$$

and that the background variables are time-independent.

Horizontal momentum equation

The leading order analysis gives

$$\frac{\partial \Pi^{(0)}}{\partial x^*} = 0 \tag{7.21}$$

Similar to this, we obtain in the next three orders that

$$\frac{\partial \Pi^{(j)}}{\partial x^*} = 0 \tag{7.22}$$

for $j \in \{1, 2, 3\}$. The fourth-order equation then yields

$$\frac{\partial u^{(0)}}{\partial t^*} + u^{(0)} \frac{\partial u^{(0)}}{\partial x^*} + w^{(0)} \frac{\partial u^{(0)}}{\partial z^*} + \theta_0 \frac{\partial \Pi^{(4)}}{\partial x^*} = 0 \tag{7.23}$$

Vertical momentum equation

The analysis of the vertical momentum equation holds two new challenges compared to the horizontal momentum equation. On the one hand, we have two scales in this direction, so that derivatives for the long vertical coordinate also appear one order higher than the corresponding derivatives for the short vertical coordinate. On the other hand, we have the non-dimensional buoyancy term $-\varepsilon^2$ on the right-hand side of the equation. The leading order is rather simple and yields

$$\frac{\partial \Pi^{(0)}}{\partial z^*} = 0. \tag{7.24}$$

In the first order equation, the ζ-derivative of the leading order pressure occurs:

$$\theta_0 \frac{\partial \Pi^{(0)}}{\partial \zeta^*} + \theta_0 \frac{\partial \Pi^{(1)}}{\partial z^*} + \theta^{(1)} \frac{\partial \Pi^{(0)}}{\partial z^*} = 0. \tag{7.25}$$

The last term is zero due to the leading order equation (7.24). It remains a balance between the large-scale change in the leading order pressure and the small-scale change in the first order-pressure:

$$\frac{\partial \Pi^{(0)}}{\partial \zeta^*} + \frac{\partial \Pi^{(1)}}{\partial z^*} = 0. \tag{7.26}$$

We can integrate equation (7.26) in z^*. Using equation (7.24), this procedure gives us

$$\frac{\partial \Pi^{(0)}}{\partial \zeta^*} = -\frac{[\Pi^{(1)}]_{z_1^*}^{z_2^*}}{z_2^* - z_1^*}. \tag{7.27}$$

We assume sublinear growth of $\Pi^{(1)}$ in z^* (compare Achatz et al. (2010), where this condition is also used in the scale analysis). Then, by taking the limit of $|z_2^* - z_1^*| \to \infty$, the right-hand side of equation (7.27) tends to zero, leaving us with

$$\frac{\partial \Pi^{(0)}}{\partial \zeta^*} = 0. \tag{7.28}$$

This shows that the leading order pressure is constant. Using this in equation (7.26), we find that

$$\frac{\partial \Pi^{(1)}}{\partial z^*} = 0. \tag{7.29}$$

The second-order equation, again with the sub-linear growth condition for $\Pi^{(2)}$ yields

$$\frac{\partial \Pi^{(1)}}{\partial \zeta^*} = \frac{-1}{\theta_0}, \tag{7.30}$$

which is the hydrostatic equilibrium for the background atmosphere. With this, we also obtain

$$\frac{\partial \Pi^{(2)}}{\partial z^*} = 0. \tag{7.31}$$

The next order yields

$$\theta_0 \frac{\partial \Pi^{(2)}}{\partial \zeta^*} + \theta^{(1)} \frac{\partial \Pi^{(1)}}{\partial \zeta^*} = 0, \tag{7.32}$$

which we can rewrite as

$$\frac{\partial \Pi^{(2)}}{\partial \zeta^*} = \frac{\theta^{(1)}}{\theta_0^2}, \tag{7.33}$$

which symbolises higher-order hydrostatics. We observe that, as neither θ_0 nor $\Pi^{(2)}$ depends on x^* and z^*, also $\theta^{(1)}$ does not depend on x^* and z^*. This is an indication that $\theta^{(1)}$ belongs to the background atmosphere and that wave contributions to the total potential temperature appear in second order at earliest. Using the equation above, we also obtain

$$\frac{\partial \Pi^{(3)}}{\partial z^*} = 0. \tag{7.34}$$

The full fourth-order equation is then

$$\frac{\partial w^{(0)}}{\partial t^*} + u^{(0)} \frac{\partial w^{(0)}}{\partial x^*} + w^{(0)} \frac{\partial w^{(0)}}{\partial z^*} + \theta_0 \left(\frac{\partial \Pi^{(4)}}{\partial z^*} + \frac{\partial \Pi^{(3)}}{\partial \zeta^*} \right) = -\frac{{\theta^{(1)}}^2}{\theta_0^2} + \frac{\theta^{(2)}}{\theta_0} \tag{7.35}$$

Entropy equation

With the assumption that θ_0 is constant, the leading order equation is trivial. The first order equation reads

$$\frac{\partial \theta^{(1)}}{\partial t^*} + u^{(0)} \frac{\partial \theta^{(1)}}{\partial x^*} + w^{(0)} \frac{\partial \theta^{(1)}}{\partial z^*} + w^{(0)} \frac{\partial \theta_0}{\partial \zeta^*} \tag{7.36}$$

Apart from the first term, we already know that the others equate to zero. Hence,

$$\frac{\partial \theta^{(1)}}{\partial t^*} = 0, \tag{7.37}$$

which concludes that $\theta^{(1)}$ only has large-scale dependence. The second-order equation is

$$\frac{\partial \theta^{(2)}}{\partial t^*} + u^{(0)}\frac{\partial \theta^{(2)}}{\partial x^*} + w^{(0)}\frac{\partial \theta^{(2)}}{\partial z^*} + w^{(0)}\frac{\partial \theta^{(1)}}{\partial \zeta^*} = 0. \tag{7.38}$$

Divergence constraint

As we assume the leading order velocity to already contain wave fluctuations, we obtain the divergence constraint

$$\frac{\partial u^{(0)}}{\partial x^*} + \frac{\partial w^{(0)}}{\partial z^*} = 0. \tag{7.39}$$

7.1.3 Special ansatz

From the previous subsection, we assume that leading order potential temperature and pressure are constant and anticipate that wave contributions in the potential temperature occur not earlier than in the second-order term and in the pressure in the fourth-order term. Moreover, we assume small amplitudes, meaning the wave terms are multiplied by an additional factor ε. We make the following ansatz, where the subscripts b and w are for background and wave parts respectively:

$$u = \varepsilon u_w \tag{7.40a}$$

$$w = \varepsilon w_w \tag{7.40b}$$

$$\theta = \theta_0 + \varepsilon\theta_b + \varepsilon^3\theta_w \tag{7.40c}$$

$$\mathit{\Pi} = \mathit{\Pi}_0 + \varepsilon\mathit{\Pi}_b + \varepsilon^5\mathit{\Pi}_w. \tag{7.40d}$$

(7.40e)

The background variables only have a large scale dependence. Observe that we omitted the second- and third order background pressure variables. They are not important for resulting equations, as they would all balance each other in the respective orders via hydrostatic equilibrium, just as we found in equations (7.30) and (7.33). So we exclude them a priori from the ansatz. Then, the term $\theta_b \partial\mathit{\Pi}_b/\partial\zeta^*$ appears as the only term in the order ε^3, which would lead to $\theta_b \equiv 0$. We assume, however, that this term is already balanced by the hydrostatics, thus, we ignore it. The equation for the leading order hydrostatic equilibrium then reads

$$\frac{\partial \mathit{\Pi}_b}{\partial \zeta^*} = \frac{-1}{\theta_0} \tag{7.41}$$

When plugged in into equation system (7.18a) and eliminating the lowest power of ε respectively, we obtain the following system:

$$\frac{\partial u_w}{\partial t^*} + \varepsilon \left(u_w \frac{\partial u_w}{\partial x^*} + w_w \frac{\partial u_w}{\partial z^*} \right) + \theta_0 \frac{\partial \mathit{\Pi}_w}{\partial x^*} + \varepsilon \theta_b \frac{\partial \mathit{\Pi}_w}{\partial x^*} + \varepsilon^3 \theta_w \frac{\partial \mathit{\Pi}_w}{\partial x^*} = 0 \tag{7.42a}$$

$$\frac{\partial w_w}{\partial t^*} + \varepsilon \left(u_w \frac{\partial w_w}{\partial x^*} + w_w \frac{\partial w_w}{\partial z^*} \right) + \theta_0 \frac{\partial \mathit{\Pi}_w}{\partial z^*} + \varepsilon \theta_b \frac{\partial \mathit{\Pi}_w}{\partial z^*} + \varepsilon^3 \theta_w \frac{\partial \mathit{\Pi}_w}{\partial z^*} + \theta_w \frac{\partial \mathit{\Pi}_b}{\partial \zeta^*} = 0 \tag{7.42b}$$

$$\frac{\partial \theta_w}{\partial t^*} + \varepsilon \left(u_w \frac{\partial \theta_w}{\partial x^*} + w_w \frac{\partial \theta_w}{\partial z^*} \right) + w_w \frac{\partial \theta_b}{\partial \zeta^*} = 0 \tag{7.42c}$$

$$\frac{\partial u_w}{\partial x^*} + \frac{\partial w_w}{\partial z^*} = 0 \tag{7.42d}$$

We extract the leading-order system:

$$\frac{\partial u_w}{\partial t^*} + \theta_0 \frac{\partial \mathit{\Pi}_w}{\partial x^*} = 0 \tag{7.43a}$$

$$\frac{\partial w_w}{\partial t^*} + \theta_0 \frac{\partial \mathit{\Pi}_w}{\partial z^*} + \theta_w \frac{\partial \mathit{\Pi}_b}{\partial \zeta^*} = 0 \tag{7.43b}$$

$$\frac{\partial \theta_w}{\partial t^*} + w_w \frac{\partial \theta_b}{\partial \zeta^*} = 0 \tag{7.43c}$$

$$\frac{\partial u_w}{\partial x^*} + \frac{\partial w_w}{\partial z^*} = 0 \tag{7.43d}$$

We recognize a similarity between the present equation system and system (3.1). Using the definition

$$N^{*2} = \frac{1}{\theta_0} \frac{\partial \theta_b}{\partial \zeta *} \tag{7.44}$$

for the non-dimensional Brunt-Väisälä frequency, we can transform the system into a single equation for w_w, in a similar fashion as we derived equation (3.5) from system (3.1). We find the following equation:

$$\left(\frac{\partial^2}{\partial x^{*2}} + \frac{\partial^2}{\partial z^{*2}} \right) \frac{\partial^2 w_w}{\partial t^{*2}} + N^{*2} \frac{\partial^2 w_w}{\partial x^{*2}} = 0. \tag{7.45}$$

We start with a plane-wave ansatz in x^* and t^* in order to investigate the impact of the stratification on the vertical structure of the wave:

$$w_w = \hat{w}(z)\exp(i(kx - \omega t)). \tag{7.46}$$

The resulting equation is

$$\frac{\partial^2 \hat{w}}{\partial z^{*2}} + k^2 \left(\frac{N^{*2}}{\omega^2} - 1\right)\hat{w} = 0. \tag{7.47}$$

We name the coefficient in front of the second term as

$$m^2 = k^2 \left(\frac{N^{*2}}{\omega^2} - 1\right). \tag{7.48}$$

Note that this expression does not depend on z^* , as N^* depends only on ζ^*. This means, that locally, i.e. on a scale of a vertical wavelength, the solution looks like a plane wave:

$$\hat{w}(z^*) = \hat{w}_0 \exp(im(\zeta^*)z^*). \tag{7.49}$$

If we want to analyse the large scale behaviour of $\hat{w}$, we have to rescale the equation on the scale of the tropopause, which is resolved by ζ^*. We recall that $\zeta^* = \varepsilon z^*$, therefore, we write

$$\frac{\partial \hat{w}}{\partial z^*} = \varepsilon \frac{\partial \hat{w}}{\partial \varepsilon z^*} = \varepsilon \frac{\partial \hat{w}}{\partial \zeta^*}. \tag{7.50}$$

Using this, we obtain the re-scaled Taylor-Goldstein equation

$$\varepsilon^2 \frac{\partial^2 \hat{w}}{\partial \zeta^{*2}} + m(\zeta^*)^2 \hat{w} = 0. \tag{7.51}$$

This is the classical WKB equation (see Bender and Orszag (1978), chapter 10), so it seems appropriate to use a WKB ansatz for $\hat{w}$:

$$\hat{w} = \left(\hat{w}^{(0)}(\zeta^*) + \varepsilon \hat{w}^{(1)}(\zeta^*)\right)\exp\left(i\frac{\phi(\zeta^*)}{\varepsilon}\right). \tag{7.52}$$

Here, $\hat{w}^{(j)}$ is the j-th order amplitude, which has a long-scale dependence and ϕ is the possibly non-linear phase function that contains information about the short-scale wavenumber. Remember that equation (7.51) is derived from the leading-order system (7.43), therefore it is not necessary to develop the WKB ansatz past leading order. We, however, include the first order for a specific reason. When inserting the approach into equation (7.51), the leading order equation is an equation for the phase while the first order equation describes the evolution of the leading order amplitude. To see that this is not affected by the first-order amplitude, we include it in the ansatz and show that its contributions do not appear in the first order equation.

For the first derivative of $\hat{w}$, we obtain

$$\begin{aligned}
\frac{\mathrm{d}\hat{w}}{\mathrm{d}\zeta^*} &= \frac{\mathrm{d}}{\mathrm{d}\zeta^*}\left(\left(\hat{w}^{(0)}(\zeta^*) + \varepsilon\hat{w}^{(1)}(\zeta^*)\right)\exp\left(i\frac{\phi(\zeta^*)}{\varepsilon}\right)\right) \\
&= \left(\frac{\mathrm{d}\hat{w}^{(0)}}{\mathrm{d}\zeta^*} + \varepsilon\frac{\mathrm{d}\hat{w}^{(1)}}{\mathrm{d}\zeta^*}\right)\exp(i\frac{\phi}{\varepsilon}) + \left(\hat{w}^{(0)} + \varepsilon\hat{w}^{(1)}\right)\frac{\mathrm{d}}{\mathrm{d}\zeta^*}\left(\exp\left(i\frac{\phi(\zeta^*)}{\varepsilon}\right)\right) \qquad (7.53) \\
&= \left(\frac{\mathrm{d}\hat{w}^{(0)}}{\mathrm{d}\zeta^*} + \varepsilon\frac{\mathrm{d}\hat{w}^{(1)}}{\mathrm{d}\zeta^*}\right)\exp(i\frac{\phi}{\varepsilon}) + \varepsilon^{-1}i\left(\hat{w}^{(0)} + \varepsilon\hat{w}^{(1)}\right)\frac{\mathrm{d}\phi}{\mathrm{d}\zeta^*}\exp(i\frac{\phi}{\varepsilon})
\end{aligned}$$

In a similar fashion, we can derive the second derivative of $\hat{w}$:

$$\begin{aligned}
\frac{\mathrm{d}^2\hat{w}}{\mathrm{d}\zeta^{*2}} = &\left(\frac{\mathrm{d}^2\hat{w}^{(0)}}{\mathrm{d}\zeta^{*2}} + \varepsilon\frac{\mathrm{d}^2\hat{w}^{(1)}}{\mathrm{d}\zeta^{*2}}\right)\exp(i\frac{\phi}{\varepsilon}) \\
&+ \varepsilon^{-1}i\left(2\left(\frac{\mathrm{d}\hat{w}^{(0)}}{\mathrm{d}\zeta^*} + \varepsilon\frac{\mathrm{d}\hat{w}^{(1)}}{\mathrm{d}\zeta^*}\right)\frac{\mathrm{d}\phi}{\mathrm{d}\zeta^*} + \left(\hat{w}^{(0)} + \varepsilon\hat{w}^{(1)}\right)\frac{\mathrm{d}^2\phi}{\mathrm{d}\zeta^{*2}}\right)\exp(i\frac{\phi}{\varepsilon}) \\
&- \varepsilon^{-2}\left(\hat{w}^{(0)} + \varepsilon\hat{w}^{(1)}\right)\left(\frac{\mathrm{d}\phi}{\mathrm{d}\zeta^*}\right)^2\exp(i\frac{\phi}{\varepsilon}).
\end{aligned}$$

This is basically the standard WKB theory for the Boussinesq equations, which should not be surprising, as we are considering waves that have wavelengths short compared to the langht scales of the background parameters.

We insert (7.54) into equation (7.51) and collect in different powers of ε. The leading order equation is

$$-\left(\frac{\mathrm{d}\phi}{\mathrm{d}\zeta^*}\right)^2\hat{w}^{(0)} + m(\zeta^*)^2w^{(0)} = 0, \qquad (7.54)$$

which can be solved for ϕ:

$$\phi(\zeta^*) = \int_{\zeta_0^*}^{\zeta^*} m(s)\,\mathrm{d}s \qquad (7.55)$$

Note that if m is constant, we get the usual linear phase function $\phi = m\zeta^*$. The first-order equation describes the vertical change of the leading-order amplitude:

$$2m\frac{\mathrm{d}w^{(0)}}{\mathrm{d}\zeta^*} + \frac{\mathrm{d}m}{\mathrm{d}\zeta^*}w^{(0)} = 0. \qquad (7.56)$$

Rearranging yields

$$\frac{\mathrm{d}(\ln(w^{(0)}))}{\mathrm{d}\zeta^*} = \frac{\mathrm{d}(\ln(m^{-\frac{1}{2}}))}{\mathrm{d}\zeta^*}. \tag{7.57}$$

This can be integrated and we obtain the leading-order solution

$$w^{(0)}(\zeta^*) = \frac{w_0\sqrt{m_0}}{\sqrt{m(\zeta^*)}}, \tag{7.58}$$

where w_0 is a constant determined by some boundary condition and m_0 is the initial vertical ave number. We find a scaling of the solution by the square root of the wavenumber ratio, similar to what we said in chapter 3 for perfectly transmitting plane waves. This is consistent, as we assumed no classical reflection layer and therefore, WKB theory predicts propagating waves without any reflection.

7.1.4 Discussion of higher-order terms

One might have noticed that we analysed the first-order equation (7.56) while the equation (7.51) was derived from the leading order system (7.43). One might ask whether the first-order terms from system (7.42) would appear as higher-order terms in equation (7.51) and influence the leading order solution. But since the wind field we consider is divergence-free, advection terms appear not earlier than second order (see also (Achatz et al., 2010)), therefore, we do not need to take them into account. There are, however, first-order terms in the momentum equations of system (7.42) that are not advection terms and therefore could impact the leading order solution. But as we will see, they also cancel when we combine the system to a single equation.

We are able to derive an equation similar to equation (7.47) from system (7.42), but including all first-order terms. The third-order terms from the momentum equations are left out as they are too high in order to influence the leading order solution. The resulting equation then is

$$\frac{\partial^2 \hat{w}}{\partial z^{*2}} + m^2\hat{w} + \varepsilon^2\frac{1}{k^2}\left(\left(\frac{\partial \hat{w}}{\partial z}\right)^2\frac{\partial^2 \hat{w}}{\partial z^{*2}} - \hat{w}\frac{\partial \hat{w}}{\partial z^*}\frac{\partial^3 \hat{w}}{\partial z^{*3}} + \left(\frac{\partial^2 \hat{w}}{\partial z^{*2}}\right)^2 - \hat{w}\frac{\partial^4 \hat{w}}{\partial z^{*4}}\right) = 0, \tag{7.59}$$

or when transformed for the larger scale,

$$\varepsilon^2\frac{\partial^2 \hat{w}}{\partial \zeta^{*2}} + m^2\hat{w} + \varepsilon^6\frac{1}{k^2}\left(\left(\frac{\partial \hat{w}}{\partial \zeta}\right)^2\frac{\partial^2 \hat{w}}{\partial \zeta^{*2}} - \hat{w}\frac{\partial \hat{w}}{\partial \zeta^*}\frac{\partial^3 \hat{w}}{\partial \zeta^{*3}} + \left(\frac{\partial^2 \hat{w}}{\partial \zeta^{*2}}\right)^2 - \hat{w}\frac{\partial^4 \hat{w}}{\partial \zeta^{*4}}\right) = 0. \tag{7.60}$$

When inserting the WKB ansatz (7.52) into the above equation, we see that the lowest order for the non-linear terms is ε^2, thus they do not affect the leading order solution (7.58) as found from the first-order equation (7.56) in the previous subsubsection.

7.1.5 Non-stationary case

In subsection 7.1.3, we used a plane wave ansatz for x^* and t^* in equation (7.45), allowing us to find a stationary leading-order WKB solution. We want to drop now the plane wave ansatz in t^* and investigate the resulting equation

$$\left(-k^2 + \frac{\partial^2}{\partial z^{*2}}\right)\frac{\partial^2 \hat{w}}{\partial t^{*2}} - N^{*2}k^2 w \hat{=} 0 \tag{7.61}$$

with a WKB ansatz of the form

$$\hat{w} = \left(\hat{w}^{(0)}(\zeta^*, \tau^*) + \varepsilon \hat{w}^{(1)}(\zeta^*, \tau^*)\right) \exp\left(i \frac{\phi(\zeta^*, \tau^*)}{\varepsilon}\right). \tag{7.62}$$

Here $\tau^* = \varepsilon t^*$ is a stretched time coordinate that resolves the scale of a wave packet travelling vertical distances on a scale ζ^*. Inserting the ansatz and collecting in different powers of ε yields the following. The leading-order equation is

$$\left(\frac{\partial \phi}{\partial \zeta^*}\right)^2 \left(\frac{\partial \phi}{\partial \tau^*}\right)^2 + k^2 \left(\frac{\partial \phi}{\partial \tau^*}\right)^2 - k^2 N^{*2} = 0. \tag{7.63}$$

To solve this equation, we separate the unknowns by a sum with the ansatz

$$\phi(\zeta^*, \tau^*) = \phi_z(\zeta^*) + \phi_t(\tau^*) \tag{7.64}$$

and receive the equation

$$\left(\frac{\mathrm{d}\phi_z}{\mathrm{d}\zeta^*}\right)^2 \left(\frac{\mathrm{d}\phi_t}{\mathrm{d}\tau^*}\right)^2 + k^2 \left(\frac{\mathrm{d}\phi_t}{\mathrm{d}\tau^*}\right)^2 - k^2 N^{*2} = 0. \tag{7.65}$$

Except ϕ_t, none of the other variables depend on τ^*, hence

$$\phi_t = c_t \tau^*, \tag{7.66}$$

where c_t is some constant. With this knowledge, we can solve equation (7.65) for ϕ_z:

$$\phi_z(\zeta^*) = -k \int_{\zeta_0^*}^{\zeta^*} \sqrt{\frac{N^*(s)^2}{c_t^2} - 1}\,\mathrm{d}s. \tag{7.67}$$

With the usual notation $c_t = -\omega$ and $m = -k\sqrt{\frac{N^{*2}}{\omega^2} - 1}$, we obtain the phase function

$$\phi(\zeta^*) = -\omega \tau^* + \int_{\zeta_0^*}^{\zeta^*} m(s)\,\mathrm{d}s. \tag{7.68}$$

We observe that the function is still linear in time and has the same shape for the vertical coordinate. This seems meaningful, as the waves still locally obey the dispersion relation. Moreover, we are in a setup with a time-independent background.

The main difference is that the leading-order amplitude also has a time dependence, which is reflected in the first-order equation

$$2\frac{\partial w^{(0)}}{\partial \tau^*}(m^2+k^2)\omega + 2\frac{\partial w^{(0)}}{\partial \zeta^*}m\omega^2 + w^{(0)}\frac{\mathrm{d}m}{\mathrm{d}\zeta^*}\omega^2 = 0. \tag{7.69}$$

This is a first-order semi-linear partial differential equation. A common method to find solutions for this is the method of characteristics (see Evans (2010) for a detailed discussion on this method). In order to apply it, we rewrite equation (7.69) as

$$\omega\frac{\partial w^{(0)}}{\partial \zeta^*} + 2\frac{\partial w^{(0)}}{\partial \tau^*}\frac{m^2+k^2}{m\omega} = -w^{(0)}\frac{m'}{2m}. \tag{7.70}$$

Here, $m' = \mathrm{d}m/\,\mathrm{d}\zeta^*$. Moreover, we use a characteristic initial condition $w^{(0)}(\zeta^*,0) = f(\zeta^*)$. We introduce two parameters r and s, where r parametrises the initial curve $\mathcal{C}_0 = \{\zeta^*, 0, f(\zeta^*)\}$, i.e. $\mathcal{C}_0 = \{r, 0, f(r)\}$, and s parametrises $\mathcal{C} = \{\zeta^*(s;r), \tau^*(s;r), y(s;r)\}$, which is, for each r, the characteristic curve. When identifying $w^{(0)}(\zeta^*,\tau^*)$ with $y(s;r) = y(s(\zeta^*,\tau^*); r(\zeta^*,\tau^*))$, we have

$$\frac{\mathrm{d}w^{(0)}}{\mathrm{d}s} = \frac{\mathrm{d}y}{\mathrm{d}s} = \frac{\mathrm{d}\zeta^*}{\mathrm{d}s}\frac{\partial w^{(0)}}{\partial \zeta^*} + \frac{\mathrm{d}\tau^*}{\mathrm{d}s}\frac{\partial w^{(0)}}{\partial \tau^*} \tag{7.71}$$

Together with the characteristic equations

$$\frac{\mathrm{d}\zeta^*}{\mathrm{d}s} = 1 \tag{7.72}$$

$$\frac{\mathrm{d}\tau^*}{\mathrm{d}s} = \frac{m(\zeta^*(s;r)^2+k^2}{m(\zeta^*(s;r))\omega}, \tag{7.73}$$

we obtain via equation (7.70) that

$$\frac{\mathrm{d}y}{\mathrm{d}s} = -\frac{m'}{2m}. \tag{7.74}$$

Using the initial condition $y(0;r) = f(r)$, we can solve (7.74) to be

$$y(s;r) = f(r)\exp\left(\int_0^s -\frac{m(\zeta^*(s;r))'}{2m(\zeta^*(s;r))}\,\mathrm{d}q\right). \tag{7.75}$$

The other two characteristic equations (7.72) and (7.73) give the relationship between the coordinates ζ^* and τ^* and the parameters r and s. Together with the initial conditions

$$\zeta^*(0;r) = r \tag{7.76}$$

$$\tau^*(0;r) = 0, \tag{7.77}$$

we obtain

$$\zeta^*(s;r) = s + r \tag{7.78}$$

$$\tau^*(s;r) = \int_0^s \frac{m(\zeta^*(q;r)^2 + k^2}{m(\zeta^*(q;r))\omega}\,\mathrm{d}q = \int_0^s \frac{m(s+r)^2 + k^2}{m(s+r)\omega}\,\mathrm{d}q. \tag{7.79}$$

With the first of these two equations, we can further simplify the solution for y:

$$\begin{aligned} y(s;r) &= f(r)\exp\left(\int_0^s -\frac{m(q+r)'}{2m(q+r)}\,\mathrm{d}q\right) \\ &= f(r)\exp\left(-\frac{1}{2}(\ln(m(r+s) - \ln(m(r))\right) \\ &= f(r)\exp\left(\ln\left(\left(\frac{m(s+r)}{m(r)}\right)^{-\frac{1}{2}}\right)\right) \\ &= \frac{f(r)\sqrt{m(r)}}{\sqrt{m(s+r)}}. \end{aligned} \tag{7.80}$$

This looks very similar to the solution in the stationary case (equation (7.58)), with the difference that we have an implicit time dependence through the variable r. What remains is to solve equations (7.78) and (7.79) for the parameters r and s. Unfortunately, this is not possible for arbitrary stratification profiles, as the integral in equation (7.79) is hard to solve explicitly. But if we consider $(\zeta^*(s,r), \tau^*(s,r))$ as a function from $\mathbb{R}^2 \to \mathbb{R}^2$, the inverse function theorem (see Forster (2013), Chapter 8) guarantees a local representation of s and r in terms of ζ^* and τ^*, as long as

$$\frac{m(s+r)^2 + k^2}{m(s+r)\omega} - \int_0^s \frac{\partial \frac{m(q+r)^2+k^2}{m(q+r)\omega}}{\partial r}\,\mathrm{d}q \neq 0 \tag{7.81}$$

holds.

We are going to present a simple example, which shows that the solution we obtain is in line with existing theory. We assume a constant stratification N_0, which leads to a constant vertical wavenumber, i.e. $m' = 0$. Therefore, the solution for $y(s;r)$ is

$$y(s;r) = f(r) \tag{7.82}$$

The solutions to the characteristic equations then are

$$\zeta^* = s + r \tag{7.83}$$

$$\tau^* = \frac{m^2 + k^2}{m\omega} s, \tag{7.84}$$

which yields the equations

$$s = \frac{m\omega}{m^2 + k^2} \tau^* \tag{7.85}$$

$$r = \zeta^* - \frac{m\omega}{m^2 + k^2} \tau^*, \tag{7.86}$$

so that the solution is

$$w^{(0)}(\zeta^*, \tau^*) = y\left(s(\zeta^*, \tau^*); r(\zeta^*, \tau^*)\right) = f\left(r(\zeta^*, \tau^*)\right) = f\left(\zeta^* - \frac{m\omega}{m^2 + k^2}\tau^*\right). \tag{7.87}$$

Hence, the initial condition for the wave envelope gets translated with a fixed velocity $c = \frac{m\omega}{m^2+k^2}$. By using the dispersion relation (5.19), we see that this velocity can be written as

$$c = \frac{N_0 k m}{(m^2 + k^2)^{\frac{3}{2}}}, \tag{7.88}$$

which is exactly the group velocity $\frac{\partial \omega}{\partial m}$, which is in classical theory the speed at which the wave envelope travels. This is what one would expect from a wave packet in uniform stratification. We see however no dispersion in the leading-order solution. This is an effect that will occur in higher order.

The second-order equation is

$$2\frac{\partial w^{(1)}}{\partial \tau^*}(m^2 + k^2)\omega + 2\frac{\partial w^{(1)}}{\partial \zeta^*} m\omega^2 + w^{(1)}\frac{\mathrm{d}m}{\mathrm{d}\zeta^*}\omega^2 = if(\zeta^*, \tau^*), \tag{7.89}$$

where f is a real function containing derivatives of $w^{(0)}$ and also a term that is non-linear in $w^{(0)}$. The solution for $w^{(1)}$ is then the sum of the solution for the homogeneous equation (i.e. the same solution that we found for $w^{(0)}$) and a special solution for the inhomogeneous equation.

7.1.6 Reflection layer analysis

A reflection layer occurs, when the wave frequency matches the Brunt-Väisälä frequency, resulting in a vanishing vertical wavenumber. This is a classical turning point for the WKB equation (7.51) (see (Bender and Orszag, 1978) for more details). Ray tracing predicts total reflection from such a level (see Sutherland (2010)), but as we have seen in subsection 3.6.2, there might still be wave transmission depending on how large the waves are compared to the region where propagation is suppressed. Moreover, as the vertical wavenumber approaches zero, the vertical wavelength is locally very large such that the scaling assumptions we did beforehand might be violated and a rescaling is necessary.

Let us write the scaled Taylor-Goldstein equation (7.51) as

$$\varepsilon^2 \frac{\partial^2 \widehat{w}}{\partial \zeta^{*2}} + q(\zeta^*)\widehat{w} = 0. \tag{7.90}$$

At a reflection level ζ_r^*, we have $q(\zeta_r^*) = 0$. We introduce a rescaled variable around the reflection level

$$\psi = \frac{\zeta^* - \zeta_r^*}{\varepsilon^\alpha} \Leftrightarrow \zeta^* = \zeta_r^* + \varepsilon^\alpha \psi. \tag{7.91}$$

In the area around the reflection layer, we can approximate $q(\zeta^*)$ via

$$q(\zeta^*) = q(\zeta_r^* + \varepsilon^\alpha \psi) \approx q(\zeta_r^*) + \varepsilon^\alpha \psi q'(\zeta_r^*), \tag{7.92}$$

where q' is the derivative of q. We note that the first term equals zero. Using the rescaling, the equation around the reflection layer can be written as

$$\varepsilon^{2-2\alpha} \frac{\partial^2 \widehat{w}}{\partial \psi^2} + \varepsilon^\alpha \psi q'(\zeta_r^*)\widehat{w} = 0. \tag{7.93}$$

For the terms to balance, we find that $2 - 3\alpha = 0$, or $\alpha = \frac{2}{3}$. This yields

$$\psi = \frac{\zeta^* - \zeta_r^*}{\varepsilon^{\frac{2}{3}}} \sim \varepsilon^{\frac{1}{3}} z^*. \tag{7.94}$$

Hence, ψ is a variable with a scale between the original vertical wavelength and the tropopause and resolves the reflection process. By stretching the coordinate with a constant factor $q'(\zeta_r^*)^{\frac{1}{3}}$, i.e.

$$\psi^* = \psi q'(\zeta_r^*)^{\frac{1}{3}}, \tag{7.95}$$

the equation reduces to

$$\frac{\partial^2 \widehat{w}}{\partial \psi^{*2}} + \psi^* \widehat{w} = 0. \tag{7.96}$$

This is Airy's equation, which is solved by Airy fucntions $\mathrm{Ai}(\psi^*)$ and $\mathrm{Bi}(\psi^*)$. Both functions have an oscillatory part for negative ψ^*, while for positive ψ^*, Ai decays exponentially and approaches 0 and Bi grows exponentially and is unbounded. A plot of both functions around $\psi^* = 0$ can be found in figure 7.1, for more coverage, see Abramowitz and Stegun (1964). Together with the conservation of energy, we rule out Bi as a physical

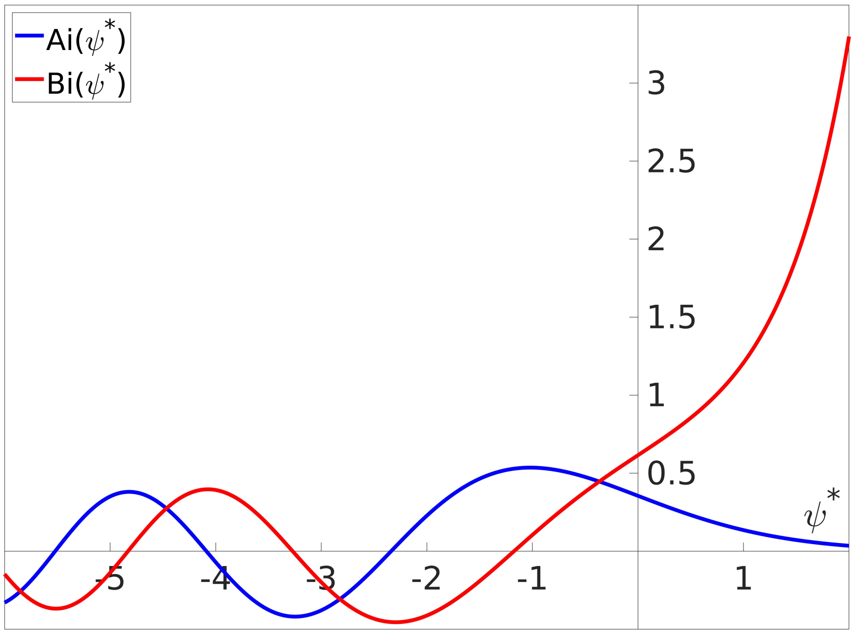

Figure 7.1: Airy functions Ai(ψ^*) in blue and Bi(ψ^*) in red.

solution. Therefore, the shape of the waves is described by Ai around a reflection layer. We conclude that the waves decay exponentially after reaching the level, but we also see that, if the layer where the waves cannot propagate is small, and eventually reach a second turning point at which waves can propagate again, wave tunnelling solutions might be supported. A detailed mathematical discussion on such a two-turning point problem points to an interesting topic for future research. An approach for this could be to solve each turning point problem individually and match the solutions via a technique called matched asymptotics (see Bender and Orszag (1978) for further reference).

7.2 Waves with wavelengths comparable to the tropopause

We anticipate this regime to be the hardest to make theoretical progress, as we do not have a scale separation between the tropopause and the wavelengths. By what we saw from the previous section, we anticipate that the leading order system can be reduced to a single equation, but this time, without a separation in the scales for the vertical derivative and the Brunt-Väisälä frequency. This turns out to be the case. As the equation we obtain is the Taylor-Goldstein equation, finding an explicit equation is in general not possible.

To derive this properly, we have a look at the full non-dimensional Boussinesq equations. Using the same notion for the reference parameters, but with aspect ratio $L_{\mathrm{TP}} \sim \Lambda$, this leads to

$$\frac{\Lambda_{\mathrm{ref}}}{H_\theta} = \frac{\Lambda_{\mathrm{ref}} g}{c_p T_{\mathrm{ref}}} = \varepsilon. \tag{7.97}$$

So although the wavelengths are comparable in size to the tropopause, they are still much smaller than the potential temperature scale height. Using this new ratio, we obtain the non-dimensional equation system

$$\varepsilon^2 \left(\frac{\partial u^*}{\partial t^*} + u^* \frac{\partial u^*}{\partial x^*} + w^* \frac{\partial u^*}{\partial z^*} \right) + \theta^* \frac{\partial \Pi^*}{\partial x^*} = 0 \tag{7.98a}$$

$$\varepsilon^2 \left(\frac{\partial w^*}{\partial t^*} + u^* \frac{\partial w^*}{\partial x^*} + w^* \frac{\partial w^*}{\partial z^*} \right) + \theta^* \frac{\partial \Pi^*}{\partial x^*} = -\varepsilon \tag{7.98b}$$

$$\frac{\partial \theta^*}{\partial t^*} + \left(u^* \frac{\partial \theta^*}{\partial x^*} + w^* \frac{\partial \theta^*}{\partial z^*} \right) = 0 \tag{7.98c}$$

$$\frac{\partial w^*}{\partial x^*} + \frac{\partial w^*}{\partial z^*} = 0 \tag{7.98d}$$

On first glance, one might think that this system corresponds to the scaling (Achatz et al., 2010) found, but there are two main differences. Here, we used the Boussinesq assumption, leading to constant leading-order pressure and ultimately to a divergence-free wave field. Although this also holds for their leading order solutions, the higher order equations would look much different. The most crucial difference, however, is the fact that the wavelengths in this case change on the same scale as the potential temperature (even though they are small and occur in first order), so that we effectively do not have a multiple-scale problem. We use a general perturbation ansatz

$$f^*(x^*, z^*, t^*) = \sum_{j=0}^{\infty} \varepsilon^j f^{(j)}(x^*, z^*, t^*) \tag{7.99}$$

and assume that leading order pressure and and potential temperature are constant and not zero. Moreover, we expect to find the same background dependencies, as we did not change the scaling for the tropopause, but only for the wave. From equations (7.9), (7.10) and(7.97), we anticipate to find wave fluctuations for potential temperature in first order and for pressure in second order. Using the perturbation ansatz, we make the following observations.

Horizontal momentum equation

The leading- and first-order analysis gives

$$\frac{\partial \Pi^{(j)}}{\partial x^*} = 0 \tag{7.100}$$

for $j \in \{0, 1\}$. The second-order equation reads

$$\frac{\partial u^{(0)}}{\partial t^*} + u^{(0)} \frac{\partial u^{(0)}}{\partial x^*} + w^{(0)} \frac{\partial u^{(0)}}{\partial z^*} + \theta_0 \frac{\partial \Pi^{(2)}}{\partial x^*} = 0 \tag{7.101}$$

Vertical momentum equation

In the investigation of the vertical momentum equation, we again hope to find hydrostatic equilibrium. The leading order equation holds nothing new:

$$\frac{\partial \Pi^{(0)}}{\partial z^*} = 0, \tag{7.102}$$

which is what we already assumed. In the first order equation, we find hydrostatic equilibrium of the first-order pressure perturbation

$$\theta_0 \frac{\partial \Pi^{(1)}}{\partial z^*} = -1. \tag{7.103}$$

The second-order equation reads

$$\frac{\partial w^{(0)}}{\partial t^*} + u^{(0)} \frac{\partial w^{(0)}}{\partial x^*} + w^{(0)} \frac{\partial w^{(0)}}{\partial z^*} + \theta_0 \frac{\partial \Pi^{(2)}}{\partial z^*} + = -\frac{\theta^{(1)}}{\theta_0} \tag{7.104}$$

Entropy equation

With the assumption that $\theta_0 \equiv$ const., the leading order equation is trivial. The first order equation reads

$$\frac{\partial \theta^{(1)}}{\partial t^*} + u^{(0)} \frac{\partial \theta^{(1)}}{\partial x^*} + w^{(0)} \frac{\partial \theta^{(1)}}{\partial z^*} = 0 \tag{7.105}$$

This leads to the assumption, that the first-order potential temperature does not only contain changes in the background, but has also contributions from wave activity.

Divergence constraint

As we assume the leading order velocity to already contain wave structures, the divergence constraint applies to them as usual:

$$\frac{\partial u^{(0)}}{\partial x^*} + \frac{\partial w^{(0)}}{\partial z^*} = 0. \tag{7.106}$$

7.2.1 Special ansatz

From equation (7.105) and also from the scaling, we anticipate that the first order potential temperature perturbation already contributes to the waves, but it also contains the change of the background potential temperature. Hence we make the assumption that

$$\theta = \theta_0 + \varepsilon(\theta_b + \theta_w). \tag{7.107}$$

We are, however, only interested in small-amplitude waves, which will push the wave contributions effectively to the second order. This leads us to the special ansatz

$$u = \varepsilon u_w \tag{7.108a}$$
$$w = \varepsilon w_w \tag{7.108b}$$
$$\theta = \theta_0 + \varepsilon\theta_b + \varepsilon^2\theta_w \tag{7.108c}$$
$$\varPi = \varPi_0 + \varepsilon\varPi_b + \varepsilon^3\varPi_w. \tag{7.108d}$$
$$\tag{7.108e}$$

Again, the hydrostatic equilibrium reads

$$\frac{\partial \varPi_b}{\partial z^*} = \frac{-1}{\theta_0}. \tag{7.109}$$

Then, we obtain the following equation system

$$\frac{\partial u_w}{\partial t^*} + \varepsilon\left(u_w\frac{\partial u_w}{\partial x^*} + w_w\frac{\partial u_w}{\partial z^*}\right) + \theta_0\frac{\partial \varPi_w}{\partial x^*} + \varepsilon\theta_b\frac{\partial \varPi_w}{\partial x^*} + \varepsilon^2\theta_w\frac{\partial \varPi_w}{\partial x^*} = 0 \tag{7.110a}$$

$$\frac{\partial w_w}{\partial t^*} + \varepsilon\left(u_w\frac{\partial w_w}{\partial x^*} + w_w\frac{\partial w_w}{\partial z^*}\right) + \theta_0\frac{\partial \varPi_w}{\partial z^*} + \varepsilon\theta_b\frac{\partial \varPi_w}{\partial z^*} + \varepsilon^2\theta_w\frac{\partial \varPi_w}{\partial z^*} + \theta_w\frac{\partial \varPi_b}{\partial z^*} = 0 \tag{7.110b}$$

$$\frac{\partial \theta_w}{\partial t^*} + \varepsilon\left(u_w\frac{\partial \theta_w}{\partial x^*} + w_w\frac{\partial \theta_w}{\partial z^*}\right) + w_w\frac{\partial \theta_b}{\partial z^*} = 0 \tag{7.110c}$$

$$\frac{\partial u_w}{\partial x^*} + \frac{\partial w_w}{\partial z^*} = 0 \tag{7.110d}$$

Isolating the leading order system yields

$$\frac{\partial u_w}{\partial t^*} + \theta_0 \frac{\partial \Pi_w}{\partial x^*} = 0 \tag{7.111a}$$

$$\frac{\partial w_w}{\partial t^*} + \theta_0 \frac{\partial \Pi_w}{\partial z^*} + \theta_w \frac{\partial \Pi_b}{\partial z^*} = 0 \tag{7.111b}$$

$$\frac{\partial \theta_w}{\partial t^*} + w_w \frac{\partial \theta_b}{\partial z^*} = 0 \tag{7.111c}$$

$$\frac{\partial u_w}{\partial x^*} + \frac{\partial w_w}{\partial z^*} = 0 \tag{7.111d}$$

This is the same as equation system (7.43), but the background and wave variables now depend on the same vertical coordinate z^*. With the definition

$$N^{*2} = \frac{1}{\theta_0} \frac{\partial \theta_b}{\partial z^*} \tag{7.112}$$

for the non-dimensional Brunt-Väisälä frequency, we can find a single equation for w_w:

$$\left(\frac{\partial^2}{\partial x^{*2}} + \frac{\partial^2}{\partial z^{*2}} \right) \frac{\partial^2 w_w}{\partial t^{*2}} + N^{*2} \frac{\partial^2 w_w}{\partial x^{*2}} = 0 \tag{7.113}$$

Using a plane-wave ansatz

$$w_w = \hat{w}(z) \exp(i(kx - \omega t)). \tag{7.114}$$

in x^* and t^* the resulting equation is again the well-known Taylor-Goldstein equation

$$\frac{\partial^2 \hat{w}}{\partial z^{*2}} + k^2 \left(\frac{N^*(z^*)^2}{\omega^2} - 1 \right) \hat{w} = 0. \tag{7.115}$$

As the coefficient in front of the second term depends on the same coordinate as the function $\hat{w}$ itself, we will not be able to gain new insights with a perturbation or WKB ansatz. Moreover, we have seen that the Taylor-Goldstein equation has no explicit solution except for some special cases. Hence, we do not gain new insights from this approach and can tackle this problem only numerically.

7.3 Long waves

As we have seen multiple times now, the Taylor-Goldstein equation appears in various forms when we are discussing small-amplitude linear plane wave propagation. Hence, for the regime of long wavelengths, we assume that the Taylor-Goldstein equation describes their interaction with the tropopause as well[1].

$$\frac{\mathrm{d}^2 w_w}{\mathrm{d}z^{*2}} + k^2 \left(\frac{N(\zeta^*)^2}{\omega^2} - 1 \right) w_w = 0. \tag{7.116}$$

Here z^* is the scale resolving a wavelength and ζ^* is the scale resolving the tropopause. The wavelength Λ_{ref} is now much longer than the tropopause depth L_{TP}, resulting in an aspect ratio

$$\frac{\Lambda_{\mathrm{ref}}}{L_{\mathrm{TP}}} = \frac{1}{\varepsilon}. \tag{7.117}$$

This gives the relation $\zeta^* = z^*/\varepsilon$. When rescaling the equation for the tropopause scale, we obtain

$$\frac{1}{\varepsilon^2} \frac{\mathrm{d}^2 w_w}{\mathrm{d}\zeta^{*2}} + k^2 \left(\frac{N^*(\zeta^*)^2}{\omega^2} - 1 \right) w_w = 0, \tag{7.118}$$

or, when multiplied by ε^2,

$$\frac{\mathrm{d}^2 w_w}{\mathrm{d}\zeta^{*2}} + \varepsilon^2 k^2 \left(\frac{N(\zeta^*)^2}{\omega^2} - 1 \right) w_w = 0. \tag{7.119}$$

We can see this as a regular perturbation problem, which can easily be solved with a perturbation ansatz (Bender and Orszag, 1978)

$$w_w = \sum_{j=0}^{\infty} \varepsilon^j w^{(j)}. \tag{7.120}$$

The first-equation is then the solution to the unperturbed problem:

$$\frac{\mathrm{d}^2 w^{(0)}}{\mathrm{d}\zeta^{*2}} = 0, \tag{7.121}$$

with the solution

$$w^{(0)}(\zeta^*) = a_0 \zeta^* + b_0. \tag{7.122}$$

The constants of integration a_0 and b_0 are determined via boundary conditions. This means that, in leading order, the wave does not get influenced by the stratification but looks like a linear function. The first-order equation is basically the same equation for the first-order wave contribution, as the perturbed part appears earliest in second order:

---

[1] This is a valid assumption, as the tropopause is still small compared to the density scale height and therefore, density variations only play a minor role. For the full description of such long-scale waves, the Boussinesq assumption would, however, not be valid any more.

$$\frac{\mathrm{d}^2 w^{(1)}}{\mathrm{d}\zeta^{*2}} = 0. \tag{7.123}$$

Usually, the whole information from the boundary data only influences the leading-order solution. This has two reasons. The first one is that the leading order solution coincides with the real solution at the boundary and one can see error development much better. The second one is that the solution stays valid for arbitrary aspect ratios, hence the computation does not need to be done again for different values of ε. Therefore, the boundary conditions for the first-order equation sets the value of the first-order solution and its derivative to 0, resulting in

$$w^{(1)} \equiv 0. \tag{7.124}$$

The second-order equation yields a correction to the first order solution:

$$\frac{\mathrm{d}^2 w^{(2)}}{\mathrm{d}\zeta^{*2}} = -k^2 \left(\frac{N^{*2}}{\omega^2} - 1 \right) w^{(0)}, \tag{7.125}$$

This is an inhomogeneous version of equation (7.121), which is solved by double integration.

$$w^{(2)}(\zeta^*) = \int\int -k^2 \left(\frac{N^*(\zeta^*)^2}{\omega^2} - 1 \right) w^{(0)}(\zeta^*)\, \mathrm{d}\zeta^* \mathrm{d}\zeta^* \tag{7.126}$$

This obviously depends on the stratification profile N^*, hence we can not give a general closed form of the solution here, but an explicit expression might be found for particular N^*-profiles. We might, for example, look at a linearly increasing profile for N^* in the tropopause:

$$N^*(\zeta^*) = 1 + \zeta^*, \quad \zeta^* \in [0, 1]. \tag{7.127}$$

Remember that ζ^* resolves the tropopause and N^* is non-dimensionalised by a reference value N_{ref}. Then, we find that

$$\begin{aligned} w^{(2)}(\zeta^*) = {} & \frac{1}{20} a_0 \zeta^{*5} + \frac{1}{4} \left(\frac{2}{3} a_0 + \frac{1}{3} b_0 \right) \zeta^{*4} \\ & + \frac{1}{3} \left(\frac{1}{2} (1 - \omega^2) a_0 + b_0 \right) \zeta^{*3} + \frac{1}{2} \left(1 - \omega^2 \right) b_0 \zeta^{*2} + c_0 \zeta^{*1} + d_0, \end{aligned} \tag{7.128}$$

where a_0, b_0 are given by the solution (7.122) and c_0, d_0 are determined by boundary conditions. To be consistent with the first order equation, $w^{(2)}(0) = 0 = w^{(2)\prime}(0)$, therefore $c_0 = 0 = d_0$.

8 Conclusion and outlook

The main purpose of this work was to study the interaction between gravity waves and the tropopause. We took on this task with different methods to shed light on many aspects of this interaction.

As the tropopause covers a rather shallow area compared to typical atmospheric scale heights, we decided to use the Boussinesq equations. Since we were also not interested in wave breaking, we assumed small amplitudes which allowed a linearisation of the Boussinesq equations.

The first part of the work focused on the interaction of plane waves with the tropopause. Starting with an atmosphere at rest, we inserted a plane wave ansatz into the governing equations and found out that the vertical dependency of the solution is described by the Taylor-Goldstein equation. Following an ansatz by (Eliassen and Palm, 1961), we divided the tropopause, which has a non-constant stratification in general, into layers with constant stratification. Each layer allowed for a local solution, which were then matched at the layer interfaces in a meaningful way to yield a global solution. A proof for the convergence of this method was given. A major advantage over a direct numerical simulation of the Taylor-Goldstein equation was the fact that we could separate upward and downward propagating wave components, which allowed for a computation of a transmission coefficient, which was derived from energy conservation.

We investigated the limit of the number of layers tending to infinity. Although it was not possible to find a closed formula for the occurring matrix product, we found a reformulation of the Taylor-Goldstein equation in a set of variables that allowed for the computation of transmission and reflection coefficients directly form the solution of a numerical simulation.

A study was carried out to investigate the convergence behaviour. Not only did we find that the transmission coefficients from the multi-layer method converged to the ones from the reformulated Taylor-Goldstein equation with convergence order two, but also that the errors are small already for a low number of layers which makes the multi-layer method a very efficient way to predict wave transmission. The computational cost was lower by a factor 1000 than comparable methods (e.g. Nault and Sutherland (2007)).

The next task was the inclusion of a non-steady background wind. The Taylor-Goldstein equation then included the relative wave frequency as well as an additional term involving the curvature of the wind. We extended the multi-layer method in the way that we now also used constant approximations for the background wind and its curvature in each layer. We discussed the correct matching conditions and showed that, with the matching conditions we used, the method was still convergent. To conclude that chapter, we made a scale analysis of the curvature term and showed that there could be realistic atmospheric conditions under which the term is not negligible.

We continued our studies with the development of a method to describe the interaction of wave packets and the tropopause. Via Fourier transform, we were able to derive a partial differential equation together with initial data corresponding to wave packets. When modelling wave packets as an approximation of finitely many plane waves, it was possible to apply the multi-layer method for each of those waves and we obtained a result for wave packets. Although we could also compute the transmission of a given wave packet through the tropopause, a much more powerful application was found in computing the spatio-temporal evolution of a given wave packet. In the way we formulated the method, we could apply inverse Fourier transform on the solution to find the wave packet evolution in real space. This corresponds to a weighted superposition of the plane wave solutions we found from the multi-layer method. The biggest advantage over the use of numerical flow solvers was that we neither had time stepping restrictions nor any scaling assumptions like a WKB-like scale separation. We briefly discussed the extension of this approach to two-dimensional wave packets.

A numerical study was carried out to corroborate our findings. We used PincFloit (see Rieper et al. (2013b)) to set up simulations of the full non-linear Boussinesq equations for several test cases, starting with a plane wave set-up. The transmission coefficients we computed did coincide very well with their theoretical counterparts. We found, however, that the transmission was a little bit to high for some simulations with a realistic tropopause profile. This seemed to be related to the resolution of the model. For the wave-packet setup, we decided to compare the evolution of the same wave packet but computed with different methods. Again, the numerical simulations confirmed the theoretical findings.

The last part of the work dealt with a different approach for finding gravity wave-tropopause interaction. As we saw from the previous work that waves exhibited different behaviour for different wavelength regimes, we decided to have a closer look at this and divided the waves into classes characterised by the aspect ratio of their wavelength and the tropopause depth. For waves with short wavelength compared to the tropopause, we could find a scaling that allowed a WKB ansatz. We showed via the method of characteristics that leading order solutions exist, but can not be written down explicitly in most cases. Waves with wavelength similar to the tropopause depth did not permit a scale separation, hence no further theoretical insights could be gained. Long waves were found to ignore the stratification changes in the tropopause in their leading order solution, only the first order corrections were found to incorporate the stratification.

Over the course of our research, a few challenges arose, which shall be included here as a concluding discussion. Although the multi-layer method agrees very well with numerical simulations, it is still based on the linearised Boussinesq equations. It would be worth investigating if the method can still be applied for more general circumstances, such as (weak) non-linearity. Also using a different sound-proof system such as the anelastic equations or the pseudo-incompressible equations give a task that is worthwhile persuading. At least in the case of the anelastic equations, one can find a single equation for the vertical wind (Sutherland, 2010). (Klein et al., 2010) find a Sturm-Liouville-type second order differential equation for the vertical structure of w for the anelastic, pseudo-incompressible and compressible models. The same methodology as developed in the present work could be applied to either of those equations. Another challenge is the adaptation of the multi-layer method to two dimensional wave packets. Although there was some work done in this direction and there is an existing code that seems to compute the evolution of a 2D-wave packet correctly, there is still some theoretical work behind the scenes that needs to be done in order to ensure the correctness of the method. Alternatively, one could try to use the efficiency we found for the vertical dimension and combine it with a grid-based approach for the horizontal dimension. If this succeeds, the multi-layer method could represent an alternative to ray tracers in weather and climate models. On the mathematical side, the reflection layer analysis for short waves showed that it seems possible to support wave tunnelling, but a rigorous derivation for a two-turning point problem remains to be done. Finally, the small discrepancies in the transmission coefficients between numerical and multi-layer solution for the realistic tropopause profile could be investigated further.

Bibliography

M. Abramowitz and I. Stegun. *Handbook of mathematical functions with formulas, graphs and mathematical tables.* United States National Bureau of Standards, 1964.

U. Achatz, R. Klein, and F. Senf. Gravity waves, scale asymptotics and the pseudo-incompressible equations. *J. Fluid Mech.*, 2010.

C. M. Bender and S. A. Orszag. *Advanced mathematical methods for scientists and engineers*, volume 42. McGraw-Hill Book Company, 1978.

D. J. Benney and A. C. Newell. The propagation of nonlinear wave envelopes. *J. Math. and Phys.*, 46, 1967.

T. Birner. Fine-scale structure of the extratropical tropopause region. *J. Geophys. Res.*, 111, 2006.

T. Birner, A. Dörnbrack, and U. Schumann. How sharp is the tropopause at midlatitudes? *Geophys. Res. Let.*, 2002.

G. L. Brown and B. R. Sutherland. Internal wave tunnelling through non-uniformly stratified shear flow. *Atmosphere-Ocean*, 45, 2007.

G. Bölöni, B. Ribstein, J. Muraschko, C. Sgoff, J. Wei, and U. Achatz. The interaction between atmospheric gravity waves and large scale flows: an efficient description beyond the nonacceleration paradigm. *J. Atmos. Sci.*, 2016.

E. F. Danielsen and R. Bleck. Tropospheric and stratospheric ducting of stationary mountain lee waves. *J. Atmos. Sci.*, 27, 1970.

P. G. Drazin and W. H. Reid. *Hydrodynamic Stability.* Cambridge University Press, 1981.

D. R. Durran. Improving the anelastic approximation. *J. Atmos. Sci.*, 1989.

D. R. Durran. *Numerical methods for wave equations in geophysical fluid dynamics.* Springer-Verlag, 1999.

A. Eliassen and E. Palm. On the transfer of energy in stationary mountain waves. *Geofys. Publ.*, 22:1–23, 1961.

L. C. Evans. *Partial Differential Equations*, volume 19 of *Graduate Studies in Mathematics*. American Mathematical Society, second edition, 2010.

O. Forster. *Analysis 3*. Springer Spektrum, 7. edition, 2012.

O. Forster. *Analysis 2*. Springer Spektrum, 10. edition, 2013.

D. C. Fritts and M. J. Alexander. Gravity wave dynamics and effects in the middle atmosphere. *Rev. Geophys.*, 41(1), 2003.

A. Gettelman, P. Hoor, L. L. Pan, W. J. Randel, M. I. Hegglin, and T. Birner. The extratropical upper troposphere and lower stratosphere. *Rev. of Geophys.*, 49, 2011.

S. Gisinger, A. Dörnbrack, V. Matthias, J. D. Doyle, S. D. Eckermann, B. Ehard, L. Hoffmann, B. Kaifler, C. G. Kruse, and M. Rapp. Atmospheric conditions during the deep propagating gravity wave experiment (deepwave). *Mon. Weather Rev.*, 145(10), 2017.

R. H. J. Grimshaw. The modulation of an internal gravity-wave packet and the resonance with the mean motion. *Stud. Appl. Math.*, 56, 1977.

ISO 2533:1975. Standard atmosphere. Standard, International Organisation for Standardization, Geneva, CH, 1975.

R. Klein. Scale-dependent models for atmospheric flows. *Annu. Rev. Fluid Mech.*, 2010.

R. Klein. On the regime of validity of sound-proof model equations for atmospheric flows. In *ECMWF Workshop on Nonhydrostatic Modelling*, November 2010 2011.

R. Klein, U. Achatz, D. Bresch, O. Knio, and P. K. Smolarkiewicz. Regime of validity of soundproof atmospheric flow models. *J. Atmos. Sci.*, 67, 2010.

L. Lara. A numerical method for solving a system of nonautonomous linear ordinary differential equations. *Appl. Math. Comput.*, 2004.

J. Muraschko, M. D. Fruman, U. Achatz, S. Hickel, and Y. Toledo. On the application of wentzel-kramer-brioullin theory for the simulation of the weakly non-linear dynamics of gravity waves. *Quart. J. R. Met. Soc.*, 141, 2015.

J. T. Nault and B. R. Sutherland. Internal wave transmission in nonuniform flows. *Phys. Fluids*, 19(016601), 2007.

C. Pütz and R. Klein. Evolution of small-amplitude gravity wave packets in non-uniform background. 2018. submitted.

C. Pütz, M. Schlutow, R. Klein, V. Bense, and P. Spichtinger. Transmission and reflection of gravity waves at non-uniform stratification layers. *Theor. Comput. Fluid Dyn.*, 2018. submitted.

F. Rieper, U. Achatz, and R. Klein. Range of validity of an extended wkb theory for atmospheric gravity waves: one-dimensional and two-dimensional case. *J. Fluid Mech.*, 2013a.

F. Rieper, S. Hickel, and U. Achatz. A conservative integration of the pseudo-incompressible equations with implicit turbulence parametrization. *Mon. Weather Rev.*, 2013b.

M. Schlutow, R. Klein, and U. Achatz. Finite-amplitude gravity waves in the atmosphere: travelling wave solutions. *J. Fluid Mech.*, 826, 2017.

J. Stalker. *Complex Analysis.* Birkhäuser, 1998.

E. M. Stein and R. Shakarchi. *Fourier Analysis: An Introduction.* Princeton Lectures in Analysis. Princeton University Press, 2003.

B. R. Sutherland. *Internal Gravity Waves.* Cambridge University Press, 2010.

B. R. Sutherland and K. Yewchuck. Internal wave tunnelling. *J. Fluid Mech.*, 2004.

G. Teschl. *Ordinary Differential Equations and Dynamical Systems*, volume 140 of *Graduate studies in mathematics.* American Mathematical Society, 2012.

L. Thomas, R. Worthington, and A. McDonald. Inertia-gravity waves in the troposphere and lower stratosphere associated with a jet stream exit region. *Ann. Geophys.*, 17, 1999.

J. H. Williamson. Low-storage runge-kutta schemes. *J. Comp. Phys.*, 35, 1980.

List of Figures

Zusammenfassung

In der Arbeit wird ein Modell, welches in der Lage ist, die Evolution von Schwerewellen mit kleiner Amplitude in einer höhenveränderlchen Atmosphäre vorherzusagen, hergeleitet. Im ersten Teil wird die Mehrschichten-Methode, welche auf einer Unterteilung einer ruhigen Atmosphäre in mehrere Schichten mit konstanter Stratifizierung beruht, beschrieben. Für diesen einfachen Fall können explizite Lösungen für die Boussinesq-Gleichungen gefunden werden. Diese Lösungen sind ebene Wellen und werden an den Schnittstellen der jeweiligen Schichten zusammengefügt. Die Konvergenz des Vorgehens wird bewiesen und die Konvergenzordnung diskutiert. Die Mehrschichten-Methode wird benutzt um Transmissionskoeffizienten zu finden. Diese beschreiben, wie viel Wellenenergie über einen Bereich mit ungleichmäßiger Stratifizierung transportiert wird.

Wenn man einen höhenveränderlichen Wind berücksichtigt verändern sich die beschreibenden Gleichungen. Die Frequenz wird Doppler-verschoben und man erhält einen zusätzlichen Term, der die zweite Ableitung des Windes enthält. Dieser sogenannte Krümmungsterm wird mit Hilfe einer Skalenanalyse untersucht. Es wird gezeigt, dass es realistische atmosphärische Konfigurationen geben kann, bei denen Schwerewellen signifikant beeinflusst werden. Die Mehrschichtenmethode wird angepasst um Veränderungen im Hintergrundwind zu berücksichtigen. Die Konvergenz wird dadurch nicht beeinflusst und Transmissionskoeffizienten können berechnet werden.

Der nächste Teil behandelt die Evolution von Wellenpaketen. Eine besondere Schwierigkeit ergibt sich daraus, dass ihre Entwicklung nicht länger durch eine gewöhnliche Differentialgleichung, sondern eine partielle Differentialgleichung beschrieben wird. Durch eine Fouriertransformation der Gleichung sowie eine Koordinatentransformation, um die Anfangsdaten in den Fourierraum zu transferieren, wird die Gleichung in eine Form gebracht, die es möglich macht, eine Variante der Mehrschichtenmethode anzuwenden. Um die Wellenpaketevolution im physikalischen Raum zu erhalten muss diese Lösung mit der inversen Fouriertransformation behandelt werden. Ein großer Vorteil ist, dass man keine Restriktionen für Zeitschritte hat. Damit ist es möglich, das Wellenpaket zu jedem beliebigen Zeitpunkt zu berechnen, vorausgesetzt man hat die Anfangsdaten.

Die Ergebnisse werden in einer umfassenden numerischen Studie validiert.

Zum Schluss wird der Fokus auf eine Skalenanalyse von Wellen, die durch die Tropopause propagieren, gelegt. Es werden drei Bereiche unterschieden: kurze, ähnliche und lange Wellenlängen im Vergleich zur Tropopausendicke. Für kurze Wellen wird eine Skalierung gefunden, die einen WKB-Ansatz zulässt. In führender Ordnung existiert eine Lösung, aber sie kann im Allgemeinen nicht explizit dargestellt werden. Für lange Wellen wird gezeigt, dass die Stratifizierung der Tropopause in führender Ordnung irrelevant ist. Der Fall für ähnliche Wellenlängen ist der härteste für eine analytische Untersuchung, da hier keine Skalentrennung vorliegt. Es wird dargelegt, dass die Lösungen unter einer angemessenen Skalierung durch die Taylor-Goldstein Gleichung beschrieben werden, welche nur für einige Spezialfälle explizit gelöst werden kann.

Abstract

A model is derived that is able to predict the evolution of small-amplitude gravity waves in an atmosphere that changes with height.

In the first part, the multi-layer method is described, which bases on layering a steady atmosphere in several layers where the stratification is assumed to be constant. For this easier case, the Boussinesq equations can be solved explicitly via plane waves and the solutions are matched at the interfaces of the respective layers. We give a proof of the convergence of this procedure and discuss the order of convergence. The multi-layer method is used to find transmission coefficients, which describe the amount of wave energy that is transmitted through a layer of non-uniform stratification.

When including a height-dependent and non-constant background wind, the governing equations change. Most notably, the wave frequency is Doppler-shifted and an additional term occurs in the Taylor-Goldstein equation containing the second derivative of the background wind. This so-called curvature term is the subject of a scale analysis with the result that there can be realistic atmospheric configurations that influences gravity waves non-negligibly. The multi-layer method is adapted to account for changes in the background wind. The convergence is not affected and it still supplies transmission coefficients very fast and efficiently.

The next part deals with the evolution of wave packets. This is particularly challenging as their evolution is no longer described by an ordinary differential equation but a partial differential equation. A Fourier transform is used on the equation as well as a coordinate transformation to translate wave packet initial data to Fourier space. This brings the equation into a shape that permits a variant of the multi-layer method to be used to solve the equation. To obtain the wave packet evolution in physical space, inverse Fourier transform is performed on the solution. A big advantage is that this method has no time step restrictions. Therefore, a fast and efficient computation of the wave packet at any given point in time is possible, given the initial shape.

For both plane waves and wave packets, extensive numerical studies are carried out which emphasise the theoretical findings.

The last part of the work focuses on a scale analysis of waves propagating through the tropopause. The waves are divided into three regimes: short, similar and long wavelength compared to the tropopause depth. For short waves, a scaling is found that allows for a WKB approach. Leading-order solutions exist in this case, but in general, they are not explicitly representable. For the case of long waves, it is shown that the exact stratification profile in the tropopause region is not relevant for the leading order solution but only plays a role in first order corrections. The case of similar wave length is the hardest to deal with analytically, since there is no scale separation in this case. It is shown that, under an appropriate scaling, the solutions are described by the Taylor-Goldstein equation, which can only be solved explicitly in some special cases.

Acknowledgements

To begin with, I want to thank my supervisor Rupert Klein who has been an inspiration to me throughout the last few years. The conversations were always fruitful and motivational and without his guidance, this thesis would not have been possible. I thank Peter Spichtinger for interesting conversations, be it on- or off-topic, and advices. I am also grateful for everything the MS-GWaves research group featured, especially to Ulrich Achatz for the provision of PincFloit and being a capable chairperson, who always encouraged discussions and work across the different sections. Special thanks go to Mark Schlutow, who was a great office mate with whom I could discuss gravity waves, mathematics and so much more. I thank the AG Klein for a warm and comfortable working environment. I thank Darius Wuttke for being a close friend for almost ten years now and supporting me in whatever I go through. I am thankful for our Denmark group, consisting of wonderful people with whom I would go on holiday every year, and also for the latest addition to our group, Tobias Lüder, who became a good friend in no time. Special thanks go to Olaf Parczyk, who went the way of discrete math, but was nonetheless open for discussion. I also want to thank all proofreaders of this work. My deepest gratitude goes to my mother Sabine, who taught me to never give up, no matter how hopeless the situation seems to be. May she rest in peace. I thank my father Eberhard for supporting me through all the years in every possible way and my brother Hendrik for keeping my head away from work when it was needed. I want to thank my godmother Monika for everything she has done for me. And finally, my sincerest gratitude go to my one and only, my love Salome Felmy. Without you, I would not be the person I am now and none of this would have been possible. I am so happy to have met you. Thank you.

Nomenclature

$\mathcal{A}$	Wave action density	
$\vec{c}_g$	Group velocity	
c_p	Specific heat capacity of dry air at constant pressure	$1.0035\,\mathrm{Jkg}^{-1}\mathrm{K}^{-}1$
E	(Wave) Energy	
g	Gravitational acceleration	$9.81\,\mathrm{ms}^{-2}$
H_θ	Potential temperature scale height	
k	Horizontal wavenumber	
m	Vertical wavenumber	
N	Brunt-Väisälä frequency	
$\hat{\omega}$	Relative wave frequency	
ω	(Absolute) wave frequency	
$\mathit{\Pi}$	Exner pressure	
p	Pressure	
ρ	Density	
R	Specific gas constant of dry air	
θ	Potential temperature	
T	Temperature	
u	Horizontal wind	
w	Vertical wind	

Der Lebenslauf ist in der Online-Version aus Gründen des Datenschutzes nicht enthalten.

Eigenständigkeitserklärung

Hiermit versichere ich, dass ich diese Dissertation selbstständig und ohne unerlaubte fremde Hilfe verfasst habe. Ich habe nur die angegebenen Quellen und Hilfen verwendet und die aus besagten Quellen genommenen Stellen als solche kenntlich gemacht. Die Arbeit wurde in nicht in einem früheren Promotionsverfahren eingereicht.

Datum, Unterschrift